universität wien

MASTERARBEIT / MASTER'S THESIS

Titel der Masterarbeit / Title of the Master's Thesis

„Non-equilibrium vortex pinning effects at domains with suppressed critical temperature in cuprate superconductors“

verfasst von / submitted by

Kristijan Luka Mletschnig, BSc

angestrebter akademischer Grad / in partial fulfilment of the requirements for the degree of

Master of Science (MSc)

Wien, 2018 / Vienna, 2018

Studienkennzahl lt. Studienblatt / degree programme code as it appears on the student record sheet:	A 066 876
Studienrichtung lt. Studienblatt / degree programme as it appears on the student record sheet:	Masterstudium Physik
Betreut von / Supervisor:	ao. Univ.-Prof. Dr. Wolfgang Lang

Abstract

In this thesis, investigations on an unconventional critical state in superconducting $YBa_2Cu_3O_{7-\delta}$ thin films nanostructured with a square array of columnar defects are presented. Samples of 210 nm thickness were epitaxially grown on MgO substrates using pulsed-laser deposition and irradiated with 75 keV He^+ ions through Si stencil masks with holes of 180 nm diameter at lattice spacings of 300 nm and 500 nm, respectively. The samples were provided by the group of Prof. Johannes Pedarnig at the Institute of Applied Physics, Johannes Kepler University in Linz.

Different initial equilibrium vortex distributions within the columnar defect array were established by in-field cooling at various initial magnetic fields. The critical current dependency on applied magnetic field was measured upon down-ramping the magnetic field at constant temperature, revealing matching peaks of commensurate arrangement of vortices with the columnar defect array. The position of these peaks reveals an out-of-equilibrium arrangement of vortices, different from the ground state in field-cooled measurements. Remarkably, the distance between peaks still corresponds to the equilibrium matching field. The shifts of critical current peak positions for various initial field-cooled magnetic fields are explained by a terrace-like critical state model. The matching effect and the terraced critical state suppose the presence of two distinct vortex types of different mobility - strongly pinned vortices in the columnar defects and intrinsically pinned interstitial vortices.

The presence of strongly pinned vortices within the columnar defects is investigated by measurements of the angle dependence of the magnetoresistance, upon tilting the applied magnetic field with respect to the sample's c axis. The parallel component of the magnetic field follows the matching condition up to a locking angle of about 80°, exceeding the locking angle corresponding to the columnar defect's aspect ratio of about 40°. This implies strong pinning of vortices due to strong T_c suppression within the columnar defects.

The nature of the columnar defects is investigated by numerical simulations of critical temperature profiles for He^+ ion irradiation of $YBa_2Cu_3O_{7-\delta}$. Single ion trajectories and corresponding collision cascades are computed using common simulation programs for the actual dimensions of the stencil mask holes used in the fabrication of the samples. The critical temperature is computed from defect density profiles, obtained from simulation, using a pair-breaking fit, calibrated to experimental data. For 75 keV He^+ ion irradiation continuous and complete T_c suppression is found within the irradiated area of the columnar defects, with a resolution of about 10 nm lateral straggle at 200 nm depth, whereas simulations of 30 keV He^+ ion irradiation with lateral Gaussian beam distribution show a columnar defect structure up to 80 nm depth, forming a plume of sparse defect density below this depth.

Zusammenfassung

In der vorliegenden Arbeit wird ein unkonventioneller kritischer Zustand in supraleitenden $YBa_2Cu_3O_{7-\delta}$ Dünnschichten mit quadratischer Anordnung nanostrukturierter Defektkanäle untersucht. Proben von 210 nm Stärke wurden mittels gepulster Laser-Ablagerung auf MgO Substraten epitaktisch aufgewachsen und anschließend durch perforierte Si Schablonen mit 75 keV He^+ Ionen in zylindrische Defektkanäle von 180 nm Durchmesser im Abstand von 300 nm und 500 nm bestrahlt. Die Proben wurden von der Gruppe um Prof. Johannes Pedarnig am Institut für angewandte Physik an der Johannes Kepler Universität in Linz bereitgestellt.

Unterschiedliche Gleichgewichtszustände von Flussschlauchverteilungen innerhalb des Defektgitters wurden durch einfrieren verschiedener Ausgangsmagnetfelder erreicht. Die Abhängigkeit des kritischen Stromes bei herunterfahren des angelegten Magnetfelds bei konstanter Temperatur zeigt Maxima im kritischen Strom bei übereinstimmender Anordnung von Flussschlauch- und Defektgitter. Auffällig ist, dass die Abstände der Stromspitzen weiterhin denen des Gleichgewichtszustands entsprechen. Dies kann durch einem Modell mit terrassenförmiger Anordnung von Domänen mit gleicher Anzahl an Flussschläuchen pro Defektkanal erklärt werden. Zur Beschreibung dieses Zustands werden Flussschläuche zweier unterschiedlicher Mobilitäten vorausgesetzt - starke Haftung in Defektkanälen und schwächer haftende Flussschläuche an intrinsischen Defekten.

Um die Haftung von Flussschläuchen an Defektkanälen zu untersuchen, wird die Winkelabhängigkeit der Übereinstimmungsbedingung des Magnetwiderstands bei Verkippen des Magnetfelds bezüglich der c Achse der Probe gemessen. Es zeigt sich, dass die Komponente des angelegten Magnetfelds parallel zur c Achse der Übereinstimmungsbedingung bis zu einem Winkel von etwa 80° folgt, wobei das Aspektverhältnis für starre Flussschläuche in der gegebenen Geometrie einem Sperrwinkel von etwa 40° entspricht. Die gemessenen Positionen der kritischen Stromspitzen liegen demnach deutlich über diesem Wert, was einer erhöhten Haftung der Flussschläuche in den Defektkanälen entspricht.

Die Bestrahlung von Defektkanälen wird mittels numerischer Simulationen von He^+ Ionentrajektorien und dazugehörigen Kollisionskaskaden in $YBa_2Cu_3O_{7-\delta}$ entsprechend der tatsächlichen Probengeometrie veranschaulicht. Aus der ermittelten Defektkonzentration lässt sich mit Hilfe einer experimentell kalibrierten Paarbrechungsfunktion die zugehörige kritische Temperatur berechnen. Bestrahlung mit 75 keV He^+ Ionen zeigt durchgängige T_c Unterdrückung in Defektkanälen mit lateralem Auflösungsvermögen von etwa 10 nm in 200 nm Tiefe. Weiters wurden T_c-Profile für 30 keV He^+ Bestrahlung mit Gaußscher Strahlverteilung von 27 nm Halbwertsbreite berechnet, welche ebenfalls durchgängige Defektkanäle bis etwa 80 nm zeigen, wobei die Defektkonzentration mit steigender Tiefe rasch abfällt und der supraleitende Zustand der Probe darunter nicht vollständig unterdrückt wird.

Acknowledgments

I want to thank my supervisor Prof. Wolfgang Lang for his guidance in research and support during writing this thesis.

I would also like to thank Prof. Johannes Pedarnig and his group from the Institute of Applied Physics, Johannes Kepler University, Linz, for fabricating the samples investigated in this thesis.

Also, I wish to thank my colleagues, Georg Zechner for introducing me to the lab and sharing the peculiarities of the experimental setup, Bernd Aichner for extensive lunch breaks and making me familiar with C programming, as well as Florian Jausner for discussions during our group meetings.

My most sincere gratitude goes to my family for their enduring support and assistance. Most of all, I am grateful to Sara, for encouraging me to go on.
Buhvonej vam!

Contents

1 Introduction to Superconductivity

1.1 Origins of Superconductivity

Investigating the electronic properties of purified Hg in 1911, Heike Kamerlingh Onnes found a sudden unexpected drop in resistivity from linear metallic behavior at about 4.2 K [1], which was in sharp contrast to measurements of residual resistivity on other metals. Kamerlingh Onnes received the Nobel prize for the discovery of superconductivity in 1913.

In principle, an ideal conductor (no defects and thermal vibrations) would show zero-resistivity, since, in a perfectly periodical lattice, electron waves could propagate without being subjected to scattering, as theoretically described by Felix Bloch [2]. However, the drastic decrease in resistivity of superconductors arises due to a thermodynamic phase transition into the genuine superconducting phase.

This phase transition is revealed by the Meissner-Ochsenfeld effect. In 1933 Walther Meißner and Robert Ochsenfeld discovered the *expulsion* of a magnetic field from a superconductor upon its transition into the superconducting state [3]. Hence, a superconductor shows ideal diamagnetism in the Meissner phase. This is in sharp contrast to the behavior of a normal conductor, where eddy currents induced by a change of applied magnetic field dissipate and the magnetic field would not be expelled from the conductor upon transition into its ideal conducting state. In fact, zero-resistivity of superconductors can not be proven experimentally, since only lower bounds can be given. However, persistent currents in superconducting rings induced by low magnetic fields were observed over long time scales and allow for an estimate of resistivity being lower then 10^{-23} Ωcm [4].

It was not until 1986 that Georg Bednorz and Alexander Müller discovered the class of ceramic cuprate superconductors in the La-Ba-Cu-O compound system with a superconducting transition temperature of about 35 K [5], for which they received the Nobel prize in 1987. In the same year, M. K. Wu, P. Chu et al. [6] first synthesized the compound system Y-Ba-Cu-O with a transition temperature of $T_c = 93$ K, which today is one of the most extensively investigated superconducting oxides. The discovery of high-temperature superconductors (HTS) with critical temperatures above the boiling point of liquid nitrogen paved the way for promising technological applications.

1.2 Theories of Superconductivity

1.2.1 London Theory

Ohm's law $\vec{j} = \sigma \vec{E}$ indicates that if the electric field $\vec{E}$ is zero, the mean velocity of normal-state charge carriers $\vec{v}_n$ is zero. This contradicts the experimental findings

on zero-resistivity in superconductors, such that Ohm's law has to be replaced. The Drude model of electric transport can be expanded by introducing a two-fluid model of superconducting and normal conducting current densities $\vec{j} = \vec{j}_s + \vec{j}_n = e(n_s\vec{v}_s + n_n\vec{v}_n)$, to find a phenomenological theory of superconductivity consistent with the Maxwell equations.

The first London equation states that $\vec{E}$ does not cause a constant velocity $\vec{v}_s$ of superconducting carriers, but rather changes the superconducting current density $\vec{j}_s$ with respect to time, by accelerating superconducting charge carriers [7]. Thus, for a constant supercurrent, the electric field is zero, hence the resistivity is zero. However, it has to be noted that the superconducting current density can reach a critical current and does not increase indefinitely.

$$\frac{d\vec{j}_s}{dt} = \frac{1}{\mu_0\lambda_L^2}\vec{E} \tag{1.1}$$

The second London equation covers the expulsion of the magnetic field $\vec{B}$ and explains the Meissner-Ochsenfeld effect. The magnetic field can not be completely expelled from the superconductor's surface, since according to the Maxwell equations a discontinuous change from finite to zero magnetic field would imply an infinitely high current density along the surface. If a magnetic field is applied, a circulating shielding current around the superconductor's surface is induced, such that the magnetic field exponentially decays with respect to depth.

$$\vec{\nabla} \times \vec{j}_s = -\frac{1}{\mu_0\lambda_L^2}\vec{B} \tag{1.2}$$

The characteristic decay constant λ_L is called London penetration depth and depends on the temperature-dependent superconducting charge carrier density $n_s(T)$ with mass m_s and charge q_s. $\lambda_L(T)$ is of the order of several nanometers and diverges for $T \to T_c$ since $n_s \to 0$. μ_0 denotes the permeability of free space.

$$\lambda_L = \sqrt{\frac{m_s}{\mu_0 n_s q_s^2}} \tag{1.3}$$

1.2.2 Ginzburg-Landau Theory

Vitaly Ginzburg and Lev Landau adapted the general theory of phase transitions of second order to phenomenologically describe the macroscopic behavior of superconductivity [8]. A wave function Ψ is introduced, with $|\Psi|^2 = n_s$ as an order parameter, to allow for a series expansion of the free energy around the critical point T_c of the phase transition to second order.

$$f_s = f_n + \alpha|\Psi|^2 + \frac{1}{2}\beta|\Psi|^4 + \frac{1}{2\mu_0}|\vec{B}_a - \vec{B}_i|^2 + \frac{1}{2m_s}\left|\left(\frac{\hbar}{i}\vec{\nabla} - q\vec{A}\right)\Psi\right|^2 \tag{1.4}$$

The condensation energy per superconducting charge carrier $\alpha(T) = \alpha(0)(\frac{T}{T_c} - 1)$ is negative for $T < T_c$, whereas β is constant, which allows for f_s being smaller than the normal-state free energy below a certain temperature. Hence, it becomes energetically favorable to increase the number of superconducting charge carriers n_s in the superconducting state. On the other hand, the series expansion of the

superconducting free energy f_s tends to the normal-state free energy f_n for $T \to T_c$. The additional terms on the right hand side of equation 1.4 are phenomenological contributions. The first term accounts for the energetic contribution of a net magnetic field inside the superconductor, the second motion term allows for a spatially nonuniform superconducting charge carrier density $n_s(\vec{x})$. The macroscopic Ginzburg-Landau theory does not describe the origins of superconductivity and is hence independent of the underlying pairing mechanism. However, the approximation is only valid in the vicinity of T_c.

Minimization of the free energy provides the two Ginzburg-Landau equations, where the Ginzburg-Landau coherence length $\xi_{GL}(T)$ is introduced, which denotes the length scale on which the number of superconducting charge carriers can change. At T_c, the coherence length diverges, hence, superconductivity can not change on small scales and breaks down in the entire sample.

$$\xi_{GL} = \sqrt{\frac{\hbar^2}{2m_s|\alpha|}} \tag{1.5}$$

1.2.3 BCS Theory

A strong indication that superconductivity is not a mere electronic phenomenon is implied by the isotope effect. It was discovered that T_c is inversely proportional to the square root of the atomic mass. Hence, classical superconductivity is related to vibrations of the crystal lattice. It was John Bardeen, Leon Cooper and Bob Schrieffer who in 1957 proposed a microscopic theory of superconductivity, called BCS theory [9], by introducing a weak attractive interaction between electrons, mediated by a retarded distortion of the atomic lattice. They received the Nobel prize in 1972.

Positively charged lattice ions are slightly attracted by a passing electron, creating a cloud of positive charge, which attracts a second electron of opposite $\vec{k}$. Hence, the electron-phonon interaction allows to overcome the electrons' Coulomb repulsion and leads to the formation of electron pairs, called Cooper pairs. In the particle picture, this interaction is explained by the exchange of a virtual phonon, which is created by one electron and absorbed by the other electron. This is in strong contrast to thermally induced phonons by lattice vibration, which indeed corrupt superconductivity.

Cooper pairs are formed by electrons of opposite spin and antiparallel $\vec{k}$, such that for pairs of $(\uparrow, \vec{k})$ and $(\downarrow, -\vec{k})$ the total spin is $S = 0$ and the total $\vec{k} = 0$. Hence, Cooper pairs are subjected to bosonic statistics, allowing them to overcome the Pauli repulsion and collectively occupy a quantum state of lower energy. The amount of energy gained from this condensation into a coherent macroscopic wave function is Δ, which is called the superconducting energy gap. In other words, twice the gap energy 2Δ is needed to break Cooper pairs into single electrons. The stronger the electron-phonon coupling and the higher the electronic density of states at the Fermi level, the larger the binding energy 2Δ. Hence, the superconducting energy gap increases for decreasing temperature.

In the normal state, only electrons close to the Fermi level contribute to the electrical transport. If a voltage is applied, the Fermi-sphere of occupied $\vec{k}$ is shifted from its ground state, with electrons being scattered independently. This gives rise to normal-state resistivity with a mean electronic transport velocity at applied voltage and a fast relaxation of the Fermi-sphere if voltage is removed. However, the center of mass and $\vec{k}$ of all superconducting charge carriers are correlated due to their macroscopic wave function. Hence, all Cooper pairs would have to be scattered simultaneously to suppress the superconducting state, such that no resistivity is observed [10].

The BCS theory provides the shape of the energy gap, its temperature dependence and its relation to T_c, consistent with observations on classical superconductors. Furthermore, the Ginzburg-Landau theory can be derived as an approximation in vicinity of T_c [11]. However, it does not correctly describe the pairing mechanism of high-temperature superconductors. According to BCS theory, cuprate oxide superconductors should be bad superconductors, since they are insulators, if undoped, and have a rather low density of states and low electron-phonon coupling.

1.2.4 Unconventional Pairing Mechanism

Conventional superconductivity is microscopically explained by BCS theory, where Cooper pairing of electrons with isotropic s-wave functions with total angular momentum $L = 0$ and total spin $S = 0$ is mediated by electron-phonon interactions. In unconventional superconductors, the superconducting charge carriers are Cooper pairs as well, since the flux quantum has the same value with $q = 2e$. The total spin of Cooper pairs in YBCO is $S = 0$, as shown by Knight-Shift measurements, where spin-zero paired electrons reduce the paramagnetic contribution for decreasing temperature [12]. However, their total angular momentum is $L = 2\hbar$. This is connected to the pairing symmetry within the Cu $d_{x^2-y^2}$ orbitals, as supported by observations on characteristic d-wave interference in Josephson tunnel junctions [13, 14]. However, the pairing mechanism is still debated, but might be mediated by antiferromagnetic spin fluctuations instead of phonons, due to the high T_c.

The anisotropic symmetry of the order parameter finds its expression in the directional dependence of $\Delta(\vec{k})$ in momentum space. For isotropic s-wave pairing, there is only weak dependency of $\Delta(\vec{k}) \sim \Delta$ in momentum space. Hence, creating a quasi-particle electron of wave vector $\vec{k}$ by breaking a Cooper pair will take the same amount of energy Δ independent of the scattering direction $\vec{k}$, whereas for d-wave pairing the energy gap is strongly anisotropic $\Delta(\vec{k})$ due to its angle-dependent wave function and becomes zero in nodal directions. This translates into the situation that for specific scattering angles the energy needed to overcome the Cooper pairing is small and quasi-particles are created more easily [15].

1.3 Type-II Superconductivity

1.3.1 Shubnikov Phase and Vortices

For actual sample geometries, the local effective magnetic field will exceed the applied magnetic field on the sample's edge due to demagnetization effects. It can thus become energetically favorable to allow for an intermediate phase within the Meissner phase with partial penetration of the magnetic field, if the applied field B locally exceeds B_c. However, the creation of a phase boundary in classical superconductors is unfavorable since it requires energy.

The creation of phase boundaries can be explained within the framework of Ginzburg-Laundau theory. The energy necessary to expel the magnetic field and the condensation energy gained by binding of electrons to Cooper pairs counteract each other in contributing to the free energy. The superconducting charge carrier density $n_s(T)$ is zero within the normal state and can not increase discontinuously. It can change along a characteristic length scale given by the Ginzburg-Landau coherence length ξ_{GL}. Hence, the condition on whether energy is gained or reduced by forming a phase boundary can be associated to the ratio $\kappa = \lambda_L/\xi_{GL}$, known as the Ginzburg-Landau parameter, where the London penetration depth λ_L is the length scale at which the magnetic field can penetrate into the material without destroying superconductivity, and the coherence length ξ_{GL} denotes the length scale on which the number of superconducting charge carriers can change.

Superconductors with $\kappa > 1/\sqrt{2}$ (or $\lambda_L > \xi_{GL}/\sqrt{2}$) are classified as type-II superconductors and tend to increase the surface area between normal and superconducting phase in the so called Shubnikov or mixed state (fig. 1.2). The surface area is maximized by introducing smallest possible shielding currents creating domains of normal state within the superconductor, through which the applied magnetic field can penetrate. These normal-state domains are called flux lines or vortices.

The shielding current generated by one Cooper pair can not increase continuously, since its wave function must obey periodic boundary conditions around the flux tube. Hence, the smallest flux created by superconducting charge carriers confined within a vortex is quantized and called the flux quantum $\Phi_0 = h/2e = 2.07 \times 10^{-15}$ T m^2, with h denoting Planck's constant and e the elementary charge. Within the vortex core n_s is zero, allowing for the penetration of magnetic field. The superconducting charge carrier density increases within a characteristic length scale of ξ_{GL} up to a constant value inside the superconducting phase. The magnetic field is confined by a circular superconducting shielding current extending out to the London penetration depth of the magnetic field (fig. 1.1).

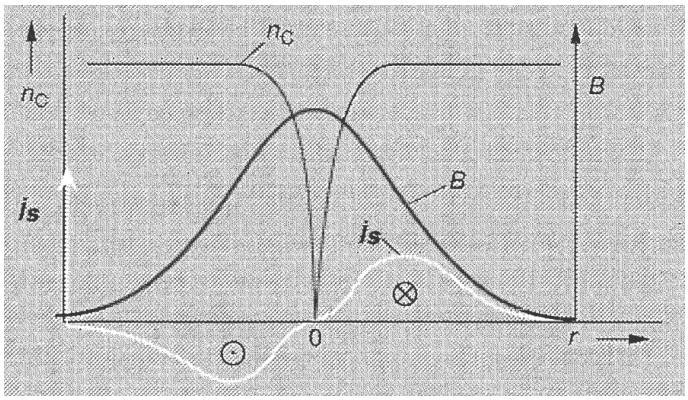

Figure 1.1: Schematic representation of superconducting charge carrier density n_s, magnetic field B and superconducting shielding current density j_s within the cross-section around a flux line. Reprinted from *Supraleitung* by W. Buckel and R. Kleiner with permission of John Wiley and Sons [10].

Upon further increasing the applied magnetic field, vortices are formed at the boundary, which gradually enter the superconductor. The density of vortices increases with the applied magnetic field, such that the fraction of magnetic field penetrating the sample is a multiple of the flux quantum.

$$B = n\Phi_0 \tag{1.6}$$

On the one hand, vortices repel each other since it is energetically favorable to maximize the surface of phase boundaries. On the other hand, they are confined to the superconductor, which can be understood as some sort of magnetic pressure. Hence, vortices in isotropic superconductors tend to arrange in a densely packed hexagonal structure, known as Abrikosov lattice [16]. However, this is only an approximation, since vortices are not stiff. The shielding current is mobile, such that vortices can bend, vibrate, entangle and pass each other resulting in a vortex liquid state. For HTS only a short range order of the hexagonal vortex lattice occurs.

1.3.2 Critical Temperature

The superconducting state breaks down if the amount of energy corresponding to Δ is added to the system. Hence, the contributions of temperature T, applied magnetic field B and supercurrent j_s to the free energy are interdependent. The critical temperature T_c is the temperature at which the superconducting transition is completely suppressed for a given magnetic field or applied current. For classical superconductors, T_c depends on the characteristic phonon frequency of the material, the electron-phonon coupling constant and the normal-state density of states at the Fermi level.

1.3.3 Critical Field

In the Meissner state the magnetic field is expelled from the superconductor by shielding currents along its surface. The energy needed to perform this work is released by the condensation of electrons to Cooper pairs. The magnetic field for which this energy exceeds the energy gained from condensation is the critical field B_c. Its

temperature dependence is governed by the empirical formula given in equation 1.7. At the critical field, the Meissner state breaks down and superconductivity in classical superconductors is suppressed.

$$B_c(T) = B_c(0)\left(1 - \left(\frac{T}{T_c}\right)^2\right) \tag{1.7}$$

In type-II superconductors, the Meissner state breaks down at a critical field B_{c1} (fig. 1.2). The critical field B_{c2} of the Shubnikov phase is reached for vortex distance being of the order of the coherence length ξ_{GL}, such that the normal-state cores of vortices begin to overlap. Hence, the size of a vortex is governed by the temperature dependence of the Ginzburg-Landau coherence length ξ_{GL}.

$$\xi_{GL}(T) = \xi_{GL}(0)\left(1 - \frac{T}{T_c}\right)^{-\frac{1}{2}} \tag{1.8}$$

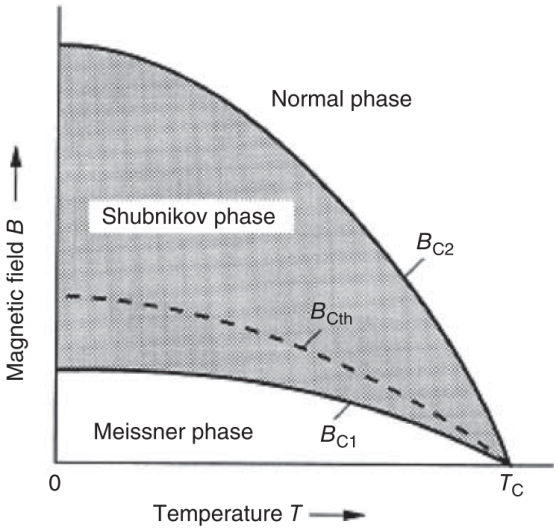

Figure 1.2: Schematic representation of the phase diagram for type-II superconductors with associated critical fields and temperature. Reprinted from *Superconductivity* by R. Kleiner and W. Buckel with permission of John Wiley and Sons [17].

1.3.4 Critical Current

The critical current density j_c is defined as the current density at which a given voltage threshold arising from a resistive state is reached. The critical current in the Meissner and Shubnikov phase need to be discriminated since resistivity mechanisms are of different origin.

Depairing Current

According to Ampere's law, a current induces a curl magnetic field around its direction of propagation. Thus, if the self field of a supercurrent in a surface layer of characteristic length λ_L exceeds B_c, the superconducting state breaks down (Silsbee effect [18]). The associated critical current j_c of the Meissner phase is called depairing current.

Critical Current of Vortex Motion

The critical current for superconductors in the Shubnikov phase is governed by vortex motion. At the critical current j_c the Lorentz force overcomes the vortex pinning potential and vortices are set in motion. The motion of vortices induces an electric field $\vec{E} = \vec{B} \times \vec{v}$ resembling a resistive state. In a simplified picture, Cooper pairs are hit by moving vortices and disassemble within them. The transport of unbound electrons causes dissipation within the normal state of the vortex core. Hence, in type-II superconductors a voltage drop can be measured before the depairing current is reached. The critical current can be increased with increasing pinning potential of vortices.

The total current density inside a superconductor consists of an induced shielding current $\vec{j}_{s,\mathrm{ind}}$ along the superconductor's surface in addition to the applied transport supercurrent $\vec{j}_{s,\mathrm{tr}}$ and a possible normal-state current $\vec{j}_n$.

$$\vec{j} = \vec{j}_{s,\mathrm{tr}} + \vec{j}_{s,\mathrm{ind}} + \vec{j}_n \tag{1.9}$$

In a simplified picture, the induced shielding current $\vec{j}_{s,\mathrm{ind}}$ is a circular surface current, whereas the applied transport current $\vec{j}_{s,\mathrm{tr}}$ is one-directional and homogeneous along the sample. Hence, the critical current j_c will be reached within the edge of the sample, where currents overlap in parallel direction.

1.3.5 Vortex Dynamics

There are several forces acting on a vortex within a superconductor, depending on macroscopic and microscopic properties such as applied magnetic field, transport current, temperature, structural properties and defects.

The most prominent force acting on a single flux line is the Lorentz force $\vec{F}_L$ at applied transport current density $\vec{j}_{s,\mathrm{tr}}$, which accelerates vortices perpendicular to the current direction.

$$\vec{F}_L = \vec{j}_{s,\mathrm{tr}} \times \hat{\Phi}_0 \tag{1.10}$$

The motion of a vortex within the superconductor experiences friction $\vec{F}_F = \eta\dot{\vec{r}}$, described by the Bardeen-Stephen friction viscosity η originating from normal-state charge carriers inside the vortex core. In equilibrium, these two forces lead to a mean vortex velocity $\vec{v}$, generating an electric field $\vec{E} = \vec{B} \times \vec{v}$ perpendicular to the direction of vortex motion. Hence, there is a parallel component to the electric transport current giving rise to flux-flow resistivity and energy dissipation [19].

There is a perpendicular component of the electric field if $\vec{v} \not\perp \vec{j}_{s,\mathrm{tr}}$, which gives rise to the vortex Hall effect. In a simplified picture, electrons of disassembled Cooper pairs are passing the normal-state core of a vortex and experience a deviation along their direction of motion due to the Lorentz force. The Cooper pairs are thus displaced perpendicular to the current direction after recombination of electrons. Vortices contribute to this voltage the same way, such that a Hall angle can be defined, though of different origin than in normal state.

The influence of the Magnus force $\vec{F}_M$ on vortex dynamics is still under debate. It is a classical effect of hydrodynamics, in which a rotating object is accelerated perpendicular to a laminar flow. In this case, the shielding current is the rotating object in the laminar flow of the transport current. Forces arising from random thermal fluctuations $\vec{F}_{th}$ become substantial around T_c, especially in HTS with their small coherence volume $\xi_{ab}\xi_c$. Furthermore, vortices are not stiff and elastic forces occur, such that vortices are bent, entangled and vibrate.

The motion of vortices is inhibited by the vortex-vortex interaction $\vec{F}_{v-v}$, which is repulsive if the vortices are of same polarity, and by defects acting as pinning centers with a force $\vec{F}_{v-p}$ of restoring character, which is discussed in section 1.3.7. The overall arrangement of an ensemble of vortices is hence determined by the interplay of vortex-vortex interactions with pinning centers at given temperature and applied magnetic field. Undisturbed idealized vortices in a homogeneous isotropic superconductor tend to arrange in a densely packed hexagonal structure, known as the Abrikosov lattice [16] due to their mutual repulsive interaction. A stable arrangement of vortices in arrays is also called vortex solid. Upon increasing temperature or thermal fluctuations, vortices vibrate and bend around their equilibrium positions, which resembles a melting process into a vortex liquid phase [19]. If the vortex structure is strongly deformed, e.g. by a given defect distribution, but stable with respect to time, the arrangement is called to be in a vortex glass state [20], which is the case in cuprate superconductors due to a short-range ordering of vortices [21].

1.3.6 Flux-Flow Magnetoresistance

Within the Bardeen-Stephen model [22] the flux-flow resistivity at acting Lorentz force is explained by dissipation of energy within the normal cores of vortices. In a comprehensive picture, Cooper pairs are hit by rapidly moving vortices and dissociated into single electrons adding normal-state resistivity while passing the normal-state domains of vortices. The probability of hitting a vortex is proportional to the ratio of vortex area per overall area $\frac{a}{A} = \frac{B}{B_{c2}}$, which corresponds to the ratio of applied magnetic field B to the Shubnikov critical field B_{c2}. Therefore, the flux-flow resistance ρ_F due to the motion of vortices is proportional to the normal-state resistivity times the fraction of $\frac{B}{B_{c2}}$.

$$\rho_F = \rho_N \frac{B}{B_{c2}} \tag{1.11}$$

In a finite sample vortices are formed on one side of the sample, transported through the superconductor and dissociate into the shielding current on the opposite side.

1.3.7 Flux Pinning

Pinning Mechanism

Vortices are pinned in regions of suppressed T_c since the shielding current of a vortex can be reduced due to the lower superconducting charge carrier density n_s. The gain in condensation energy increases with the fraction of pinned vortex cores [23]. Once a vortex is pinned, additional energy needs to be spent to create a shielding current

within the superconducting phase. The pinning of vortices can be overcome if the Lorentz force is sufficiently strong, which is the case if the transport current exceeds the critical current.

According to Bean and Livingston [24] on the one hand, a vortex inside a superconductor in vicinity of a non-superconducting area is attracted towards the phase boundary surface due to the image force of the anti-vortex it induces. On the other hand, the externally applied magnetic field repels the vortex from this surface. Hence, this surface barrier depends on the applied magnetic field. For low fields, the vortex is attracted to the surface at a distance of λ_L. The surface barrier decreases for increasing external field.

This consideration can be now applied in the opposite direction. A vortex in vicinity of a defect is attracted to the defect and gets trapped. However, prior to reaching the potential well a repulsive potential of shielding currents needs to be overcome [25]. Once a vortex is trapped, it can be seen as a contribution of a quasi-external field within the Bean-Livingston model, such that additional vortices need to overcome the surface barrier.

Intrinsic In-Plane Pinning

A most prominent example consistent with the aforementioned considerations is the trapping of vortices within the intermediate insulating layers of CuO_2 planes in the layered structure of cuprate superconductors. For magnetic fields applied parallel to the planar structure, the critical current is strongly enhanced [26] (fig. 1.3). This indicates that vortices are intrinsically pinned within the non-superconducting layers and repelled from the superconducting CuO_2 planes. A shielding current would have to be turned on for vortices to pass the surrounding superconducting layers, reducing the condensation energy of the system [27]. Tachiki et al. [28] proposed a modulation of the superconducting charge carrier density along the c-axis and found strong vortex pinning consistent with experimental data.

Intrinsic defect pinning

Any defect locally suppressing the critical transition temperature T_c acts as a pinning center for vortices. Since the pinning force increases with increased pinned fraction of a vortex, single point defects such as vacancies and interstitials are weak pinning centers [23]. The pinning potential increases for linear and planar defects such as dislocations and twin planes of twinning boundaries.

The overall enhancement of critical current in thin films of YBCO is reported to arise due to intrinsic pinning at low magnetic fields by both edge and screw dislocations along the growth direction [29], where the dislocation density of natural linear defects depends on growth parameters. Indications for enhanced pinning potential by twin planes are presented in figure 1.3, which shows a broad maximum in critical current for magnetic field applied parallel to the c axis [26]. In YBCO, twinning boundaries are formed by a change in orientation of CuO chains in the orthorhombic structure by a flip of 90°. Measurements on angle-dependent critical current density of YBCO thin films show a varying width of the enhancement with magnetic field applied perpendicular to the film plane, with maximum to minimum

critical current ranging from 38° [30] to 30° [26] and even below 10° [31]. Thus, the broadening might be dependent on synthesis parameters.

Numeric calculations assuming in-plane and planar pinning centers perpendicular to the film plane show sharp peaks for both in-plane and perpendicular orientation of an applied magnetic field in the critical current [32]. Tachiki et al. suppose the peak broadening might be connected to a distribution of tilt angles for the twin planes. Enhanced vortex pinning is also reported for edge dislocations in grain boundaries [33]. However, the density of grain boundaries in current thin film synthesis techniques is negligible.

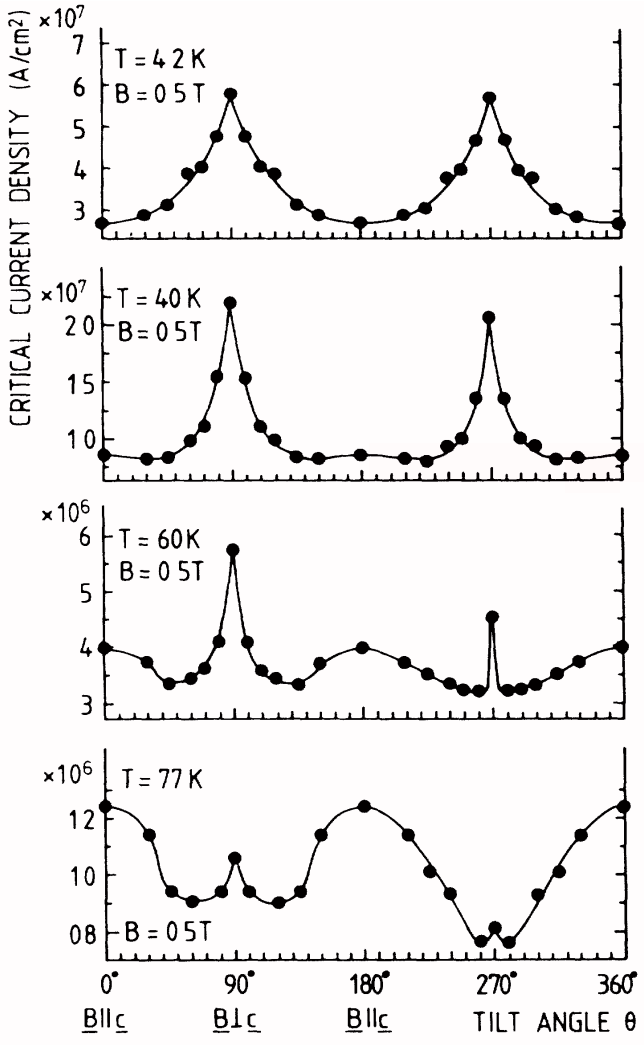

Figure 1.3: Angle dependence of the critical current density of YBCO thin films of about 250 nm thickness epitaxially grown by laser deposition at an applied magnetic field of $B = 0.5$ T for various temperatures. The angle θ is given between the direction of applied magnetic field $\vec{B}$ and the film normal. At low temperatures sharp maxima in the critical current occur for magnetic field applied parallel to CuO_2 planes. At higher temperatures broad peaks of increased j_c for pinning parallel to the c-axis becomes apparent, since the in-plane pinning and its corresponding increase in j_c is reduced. These features are assigned to pinning at twin and grain boundaries. Reprinted figure with permission from B. Roas *et al.*, Rev. Mod. Phys., 66.4, 1125 (1994). Copyright (1994) by the American Physical Society [26].

Kinked vortex structure

Another way to explain the broad peak in critical current for applied magnetic field perpendicular the film plane is the formation of a kinked vortex structure [26]. A peculiarity of layered cuprate superconductors with anisotropic coherence lengths is that shielding currents are formed within the superconducting CuO_2 planes. There is no need for shielding currents in the intermediate insulating layers. The in-plane shielding currents are weakly coupled magnetically for magnetic fields applied perpendicular to the superconducting layers. Tilting the applied magnetic field from the axis of normal incidence, the individual shielding currents are displaced within the planes and so called kinked or pancake vortices are formed [27] (fig. 1.4).

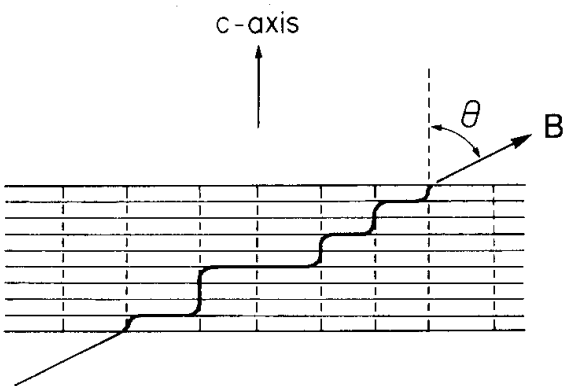

Figure 1.4: A kinked vortex structure (bold solid line) is formed by preferentially penetrating planes of suppressed superconductivity (horizontal solid lines) and twin planes (vertical dashed lines). Reprinted from M. Tachiki and S. Takahashi, Solid State Commun. 72.11, 1083. Copyright (1989), with permission from Elsevier [32].

Individual pancake shielding currents are further pinned by defects, where continuous defect structures provide more effective pinning. Thus, for aligned defects such as dislocations and twin planes vortices are locked up to a locking angle of about 1° and flux lines are still parallel to the defect alignment although the magnetic field is tilted. Upon further tilting the applied magnetic field, kinked vortex structures are formed. For twin planes in YBCO single crystals the pancake structure dissociates and the shielding currents decouple at a trapping angle of 2° to 10° [31].

Extrinsic Pinning

Technical applications of type-II superconductors are generally operated in the Shubnikov state above B_{c1}. Since the Lorentz force on a stationary vortex depends on superconducting current density, extrinsic defects suppressing T_c are introduced in so called hard superconductors to increase the critical current. Within these defects superconductivity is suppressed and no additional shielding current is needed for the formation of vortices. The total pinning force depends on the type and distribution of defects, which determines their ability to suppress superconductivity and the spreading of distortions within the vortex lattice [23].

Several types of defects are reported to increase the critical current, such as holes, blind holes, magnetic dots, non-magnetic nanodots, ion irradiation of stripes

or columnar defects [34–39]. For high current applications the critical current enhancement is sought to be independent of the orientation of an applied magnetic field. However, Civale et al. [38] found that pinning on heavy ion-irradiated stripes is stronger than pinning at arbitrarily distributed point defects at high fields and temperatures, although strongly angle dependent.

The pinning strength increases for increasing fraction of overlap between a vortex and the pinning defect. Hence, linear defects with lateral dimensions exceeding the coherence length ξ_{GL} act as strong pinning centers for aligned vortices at low magnetic field [19]. Ion irradiation allows for a controlled and continuous altering of pinning properties depending on ion species and applied irradiation dose, such as point defects, defect cascades or columnar defect tracks for increasing ion mass and irradiation energy [27]. The induction of correlated point defects by ion irradiation into columnar defects (CD) gives rise to strong increase in critical current, with the peaks in critical current coinciding with the angle of irradiation [39]. However, the number of pinning sites should not exceed the amount of vortices to be pinned, since the effective cross-section for the supercurrent decreases with increasing irradiated area. Numeric calculations indicate a maximum pinning potential of cylindrical insulating inclusions for radii being of the order of several $\xi_{GL}(0)$ even for single vortices [40]. Furthermore it was shown that the interaction between flux lines and non-superconducting columnar defects approaches the Bean-Livingston formalism for increasing defect radius [41].

According to Mkrtchyan and Schmidt [42], the number of vortices a cylindrical pinning center can accommodate is proportional to the radius r of the columnar defect and inversely proportional to the temperature-dependent coherence length $\xi(T)$ (eq. 1.12).

$$n \approx \frac{r}{2\xi(T)} \tag{1.12}$$

Doria et al. [43] found deviations of the Mkrtchyan limit for high vortex density at fields near B_{c2} considering the presence of vortices surrounding the columnar defects, which force further vortices to be trapped, hence, exceeding the limit given by Mkrtchyan.

1.4 Matching Effect and Irreversibility

1.4.1 Matching Condition

Introducing periodic pinning arrays, vortices are pinned to the defects within minima of their inter-vortex repulsive potential. Since the repulsive contribution is lowered, the vortices are stronger pinned and the Lorentz force for depinning needs to be increased. Hence, for a commensurate arrangement of the vortex lattice within the periodic pinning array, a peak in the critical current is observed. In case of a square array of defect channels with lattice spacing d, maxima occur for a distribution of n flux quanta per unit cell surface area of a pinning site. The number of vortices is given by the applied magnetic field, such that a matching condition can be derived, where the first matching field B_m occurs for a distribution of one flux quantum per pinning site. Fractional commensurability of vortices within a sublattice might occur, allowing for rational matching conditions [44].

$$nB_m = n\frac{\Phi_0}{d^2} \tag{1.13}$$

Matching effects in critical current are reported for several external defect mechanisms such as precipitates in alloys, spatial modulation in alloy concentration, periodic thickness modulation, hole patterns in films and multilayers or magnetic dots [45–50]. On YBCO, matching effects of a square lattice of holes created by e-beam lithography and dry etching were first reported by Castellanos et al. [51]. Vortex arrangements were imaged by Lorentz microscopy, where an electron beam is deflected by the magnetic field within vortices [52].

The maxima in critical current for higher order matching decrease due to the reduced net pinning potential of defects accommodating multiple vortices. In actual arrangements, intrinsic pinning sites contribute to vortex pinning. Hence, peaks in critical current become more pronounced for extrinsic defect spacing comparable to intrinsic defect distance and become sharper for closer spacing of extrinsic pinning sites [53]. However, shielding currents start to overlap for close vortex arrangement reducing the critical current [54].

Since intrinsic pinning centers are statistically distributed, the forces acting on vortices are anisotropic and the critical current shows no matching peak. However, Dam et al. [29] report a matching field of $B^* = 0.7 \cdot n_{\mathrm{disl}} \cdot \Phi_0$ of the order of 10 mT for intrinsic dislocation pinning in YBCO with as grown short range order in a mean distance of about 300 nm to 500 nm. This corresponds to a flux of about $0.7{\cdot}\Phi_0$ per dislocation, which indicates a self-organized short range order of dislocations. The lack of strict periodicity allows for a dominating role of inter-vortex repulsion, counteracting consistent matching of one flux line per dislocation.

Investigations on artificial quasi-periodic pinning arrays of Penrose lattices show enhanced critical current for a wide range of applied magnetic fields by providing a variety of matching conditions at small increments of the magnetic field [55]. Furthermore, the pinning of interstitial vortices within the potential landscape of pinned vortices allows for a stronger caging compared to periodic pinning arrays, thus broadening the peaks in critical current [56].

1.4.2 Signatures of Vortex Matching

In this section, general signatures of matching effects are discussed on previously published results of sample A used in this thesis. In sample A, columnar defects of (180 ± 5) nm in diameter with a lattice spacing of $d = (302 \pm 2)$ nm are irradiated into a YBCO thin film using 75 keV He^+ ion irradiation. The sample is presented in more detail in chapter 6. The lattice spacing corresponds to a matching field of $B_m = 22.6$ mT, which is experimentally observed in field-cooled measurements (fig. 1.6). The critical temperature of $T_c = 90$ K prior to irradiation reduced to about $T_c = 46$ K after irradiation.

The measurement of critical current is temperature dependent [57]. On the one hand, the pinning potential of intrinsic defects increases for decreasing temperature, such that matching is suppressed and peak sharpness is reduced. The increase of pinning in an unpatterned reference sample for reduced temperature is shown in figure 1.5. On the other hand, at increasing temperature, the pinning strength of columnar defects is reduced since the difference in T_c suppression between irradiated and unirradiated areas decreases. Hence, measurements on matching effects are best resolved slightly below T_c and the reduced temperature $t = T/T_c$ should be declared.

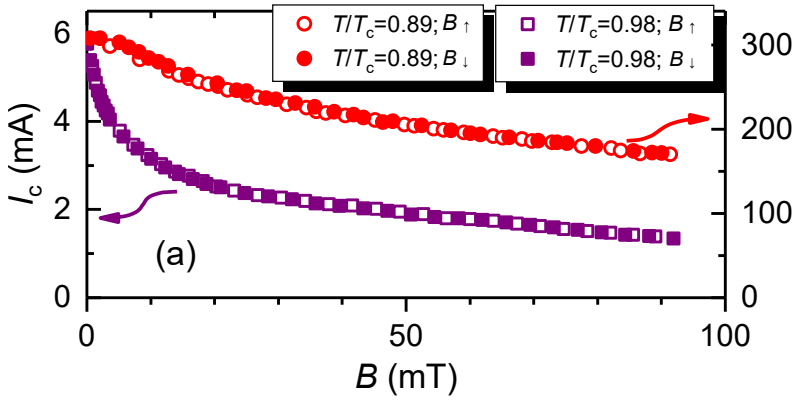

Figure 1.5: Critical current of unirradiated reference to sample A for cooling in zero magnetic field and ramping the magnetic field up (open symbols) and down (full symbols) for different temperatures. At lower temperatures the Meissner phase appears at low magnetic fields and the peak shape becomes inconsistent with the generalized critical state model of equation 1.15. Reprinted figure with permission from G. Zechner *et al.*, Phys. Rev. App., 8.1 (2017). Copyright (2017) by the American Physical Society [58].

The measurement on matching effects in critical current is further dependent on the distribution of magnetic field within the material. Thus, two distinct procedures of measuring the critical current need to be discussed:

Field-Cooled (FC) Procedure

Field-cooled measurements are recorded by applying a magnetic field B_a prior to cooling the sample in-field into the superconducting state to ensure equilibrium vortex distribution throughout the sample. After recording the critical current I_c, the sample is heated above the superconducting transition temperature T_c and the

applied magnetic field B_a is altered to the next value. A new equilibrium distribution of vortices at altered magnetic field is cooled in-field. This procedure is repeated for each data point of $I_c(B_a)$.

Zero-Field-Cooled (ZFC) Procedure

Cooling the sample below T_c in zero magnetic field and measuring the critical current $I_c(B_a)$ upon ramping the applied magnetic field B_a at constant temperature for each data point, the virgin curve of the critical current hysteresis is obtained. The procedure of measuring the critical current $I_c(B_a)$ upon ramping the magnetic field within the superconducting state is referred to as the zero-field-cooled (ZFC) ramped measurement cycle.

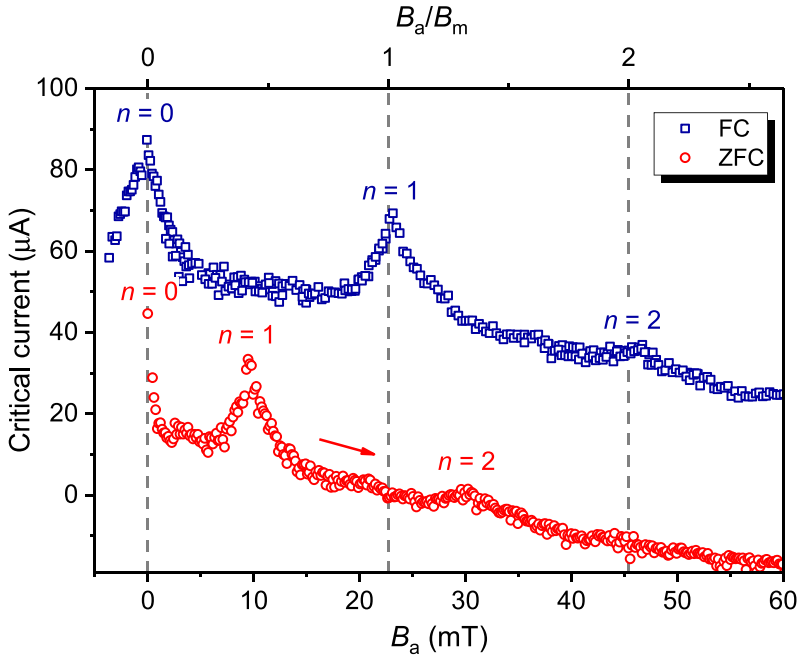

Figure 1.6: Comparison of the critical current measured after FC from above T_c to 38 K ($T/T_c = 0.78$) for every datum (blue squares) and the respective data after ZFC and ramping the applied magnetic field up (red circles). The curve is displaced by -40 μA for better visibility.[1] Reproduced from Superconductor Science and Technology [59] with permission ©IOP Publishing.

In general, the critical current decreases for increasing magnetic field due to unbalanced repulsive vortex interactions, such that a lower Lorentz force is needed for depinning [44]. Minima occur for most incommensurate arrangements of vortices due to highly mobile interstitial vortices. Such interstitial vortices need to overcome an energy barrier before reaching the columnar defect, which increases with the number of already accommodated vortices within the columnar defect. Hence, these interstitial vortices are merely quasi-pinned within interstitial sites of the potential landscape evoked by pinned vortices [60].

The maxima in resistivity of FC measurements presented in figure 1.6 coincide with maxima calculated from the matching condition given by equation 1.13, since

[1] This caption is reproduced from [59].

the in-field cooling of an applied magnetic field in equilibrium realizes a uniform arrangement of vortices, which is rearranged for each FC applied magnetic field. According to equation 1.12, the saturation of vortex accommodation of columnar defects with a diameter of 180 nm at a reduced temperature of $t = 0.83$, with $\xi_{GL}(0) = 1.4$ nm is about 5 to 6 vortices per columnar defect. However, significant peaks for multiples of the matching field are only observed up to an arrangement of two vortices per pinning site. This discrepancy occurs since the lattice spacing of the columnar defects is not considered in this calculation and interstitial vortices are channeled through the columnar defects. Furthermore, features of enhanced critical current occur at rational multiples of $n = 1/2$ and $3/2$.

The critical current measurement for ZFC ramped magnetic field shows a mismatch of measured and calculated equilibrium matching fields. This is consistent with the realization of a critical state within the edge of the sample upon ramping up a magnetic field which penetrates into the superconductor from the outside. Hence, matching peaks B_n appear at lower magnetic fields, i. e. prior to the matching conditions nB_m. Both demagnetization effects and irreversibility contribute to the formation of the critical state, as discussed in section 8.

Demagnetization

Demagnetization effects are geometry-dependent deviations of effective B_{eff} to applied magnetic fields B_a on a sample's edge [10]. The local increase of density of magnetic field lines occurs due to an increased curvature of the magnetic field as it is pushed out of the sample by shielding currents. The demagnetization is the larger the flatter the geometry.

$$B_{\mathit{eff}} = \frac{B_a}{1 - N_m} \tag{1.14}$$

The demagnetization factor N_m is zero for a magnetic field applied parallel to an infinitely long slab, which leads to equality in applied and effective magnetic field. For superconducting thin films in a perpendicular magnetic field Doria et al. [61] found that $1 - N_m \ll 1$ for infinitely thin film thickness $w/t_z \gg 1$, with the spatially averaged magnetic field $\bar{B}$ in the film coinciding with the perpendicular applied magnetic field B_a. The geometry of the samples considered in this thesis is close to this limit ($w/t_z = 286$), such that the local effective magnetic field at the sample's edge strongly exceeds the applied magnetic field $B_{\mathit{eff}} \gg B_a$.

1.4.3 Generalized Critical State Model

The penetration of vortices into a superconductor in Shubnikov state upon increasing the applied magnetic field B and their non-equilibrium distribution is called a critical state. The initial (virgin) magnetization in the Meissner phase is the same for both hard and soft superconductors, since the induction of shielding currents is not highly affected by defects. However, the magnetization hysteresis is different for hard and soft superconductors. In soft superconductors, both the Meissner and Shubnikov state are reversible. In hard superconductors, pinned vortices can not be easily shifted. Their distribution is delayed with respect to soft superconductors. Hence the magnetization is irreversible and hysteresis occurs.

A generalized critical state model for hard superconductors was derived by Xu et al. [62], unifying previous empirical models with limited validity depending on the actual system. It describes the magnetization and the dependence of an applied magnetic field B on the local macroscopic critical current density j_c at a given temperature.

$$j_c(B,T) = \frac{j_c(T)}{\left(1+\frac{B}{B_0}\right)^{\beta}} \tag{1.15}$$

It includes two parameters β and B_0. The dimensionless constant β is associated to the pinning properties of the microstructure within the material. It decreases for increasing pinning strength. The meaning of B_0 is still unclear, however, it might be connected to the thermodynamical critical field.

1.4.4 Matching in Critical Current and Magnetoresistance

The maxima in critical current $I_c(B_n)$ coincide with minima $R(B_n)$ in FC magnetoresistance measurements [56], as shown in figure 1.7.

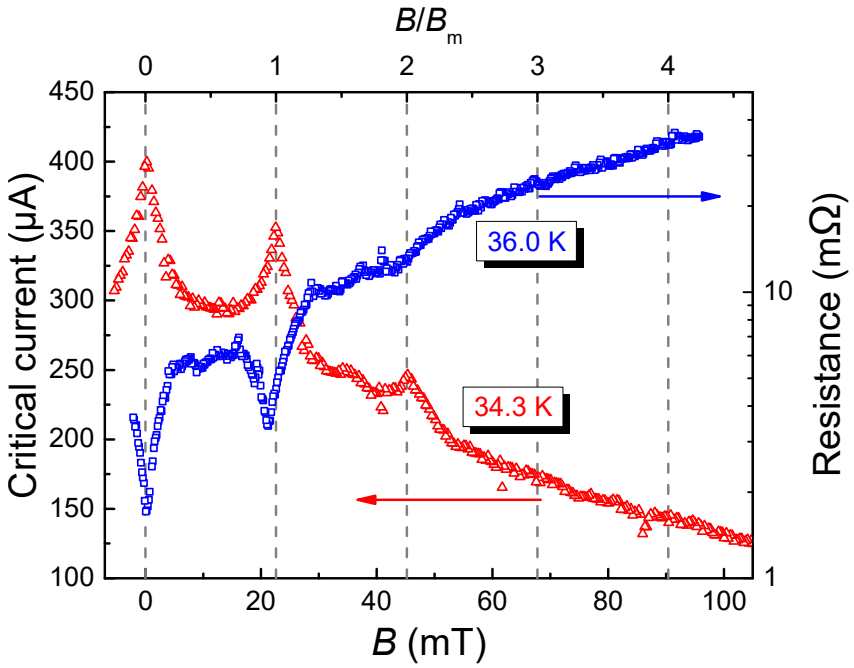

Figure 1.7: Field-Cooled (FC) experiments of sample A with magnetic fields applied in the normal state at 100 K and cooled in-field below the transition temperature of $T_c = 46$ K. The extrema of $I_c(B_n)$ and $R(B_n)$ coincide and occur at the matching condition of equation 1.13. Reprinted figure with permission from G. Zechner *et al.*, Phys. Rev. App., 8.1 (2017). Copyright (2017) by the American Physical Society [58].

Hence, the same mechanism is probed with different methods. However, both measurements in fact probe different conditions. On the one hand, the critical current I_c is obtained once enough mobile interstitial vortices contribute to the resistivity such that the threshold voltage V_t is reached. Hence, the current I_c at constant voltage V_t is measured (fig. 1.8). It probes the static situation of vortices

pinned to the CDs. However, Blamire [44] points out that a measurement of critical current determined by a voltage criterion within a matching peak in fact measures the current at which a low density of vortices is accelerated high enough to reach the voltage criterion.

On the other hand, the magnetoresistance $R(B)$ is obtained by measuring the voltage at constant bias current of $I = 200$ μA within the plastic flow regime and thus probes the dynamic situation of mobile vortices [63]. However, the only parameter in measurement of the critical current at standardized voltage threshold is the temperature, whereas the resolution of peaks in the magnetoresistance measurement moreover depends on the chosen bias current.

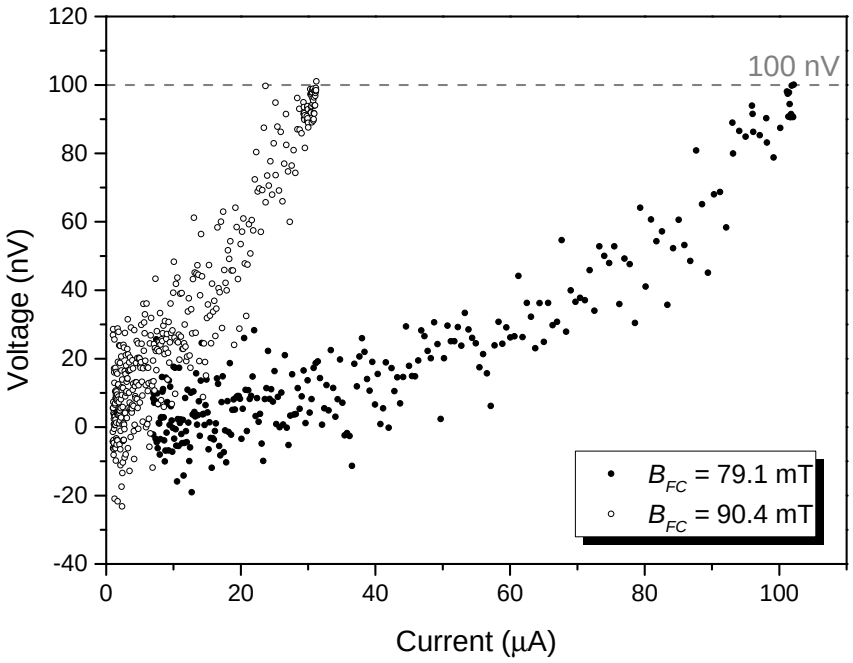

Figure 1.8: Current/Voltage characteristics for I_c measurements of sample A with field-cooling applied fields B_{FC} of 79.1 mT and 90.4 mT, respectively. For increased magnetic field the threshold condition of 100 nV is met at lower applied current. Resistance measurements would correspond to a vertical intersection of I/V-curves at $I = 200$ μA, which is not shown here.

2 The cuprate HTS $YBa_2Cu_3O_{7-\delta}$

2.1 Crystal Structure

The high-temperature superconductor $YBa_2Cu_3O_{7-\delta}$ (YBCO) is a cuprate superconductor of perovscitic structure, where $0 < \delta < 1$ denotes the oxygen deficiency of the material. The oxygen content has crucial influence on the material's crystallographic structure and electronic properties. For $\delta = 1$, the material is fully reduced to a $YBa_2Cu_3O_6$ insulator of tetragonal symmetry, whereas for $\delta = 0$, the material is fully oxidized to a $YBa_2Cu_3O_7$ quasi-metal with orthorhombic structure.

The common characteristic of cuprate superconductors is an anisotropic crystal structure containing CuO_2 layers (fig. 2.1). For YBCO, there are two CuO_2 layers per unit cell, equally spaced by the rare earth element Yttrium. This covalently bound plane shall be denoted by $Cu(2)O_2$ and its oxygen atoms by O(2) for a bond in axis a and O(3) in axis b, respectively.

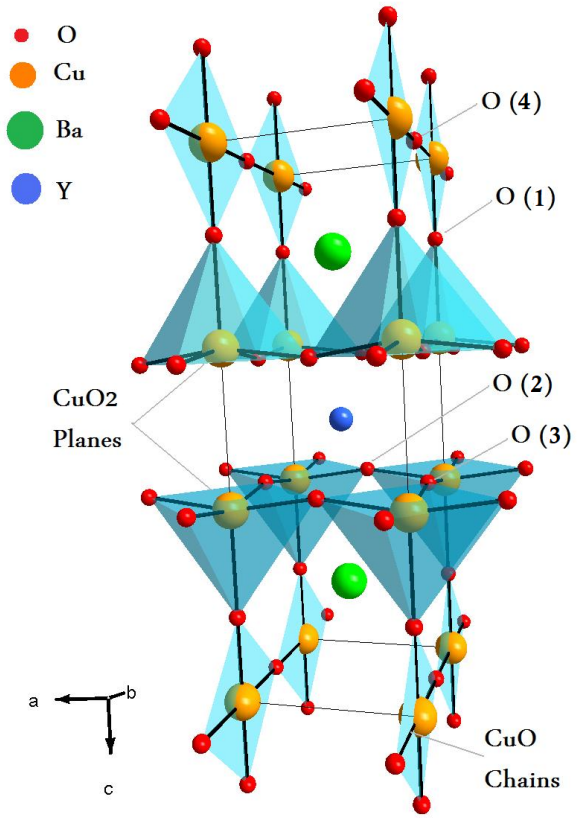

Figure 2.1: Elementary cell of orthorhombic $YBa_2Cu_3O_7$ illustrating $Cu(2)O_2$ planes and the oxygen deficient $Cu(1)O_{1-\delta}$ basal plane. O(1) indicates the site of the apical oxygen, whereas O(2) and O(3) correspond to equivalent oxygen sites in the $Cu(2)O_2$ planes. O(4) is the oxygen site in the b axis of the Cu(1)O chain. Position O(5) is unoccupied and thus not depicted, but represents the oxygen site in a axis of the $Cu(1)O_{1-\delta}$ plane. Figure adapted from [64] in public domain.

A BaO layer separates the $Cu(2)O_2$ layers from the Cu(1)O basal plane in the $YBa_2Cu_3O_7$ structure. The oxygen atoms of the Cu(1)O plane are denoted by O(5) for bonds in axis a and O(4) for bonds in axis b, respectively. The oxygen site O(1) of the BaO layer is called *apical oxygen* and forms a tetrahedron with the oxygen positions O(2) and O(3).

Changing the oxygen content δ directly affects the crystallographic structure of the $Cu(1)O_{1-\delta}$ layers. For fully reduced $YBa_2Cu_3O_6$, the positions O(4) and O(5) are unoccupied and thus crystallographically equivalent. Increasing the oxygen content, oxygen atoms tend to arrange in short CuO chains at positions O(4), such that axes a and b are not equivalent anymore. The transition from tetragonal to orthorhombic structure at $\delta \sim 0.6$ is confirmed by investigations of the oxygen content dependence on lattice parameters (fig. 2.2). In fully oxygenated $YBa_2Cu_3O_7$ the Cu(1)O chains are completely occupied [65]. Furthermore, the lattice parameter in crystallographic c axis is diminished with increasing oxygen content, indicating hole doping of the $Cu(2)O_2$ planes by Cu(1)O chains.

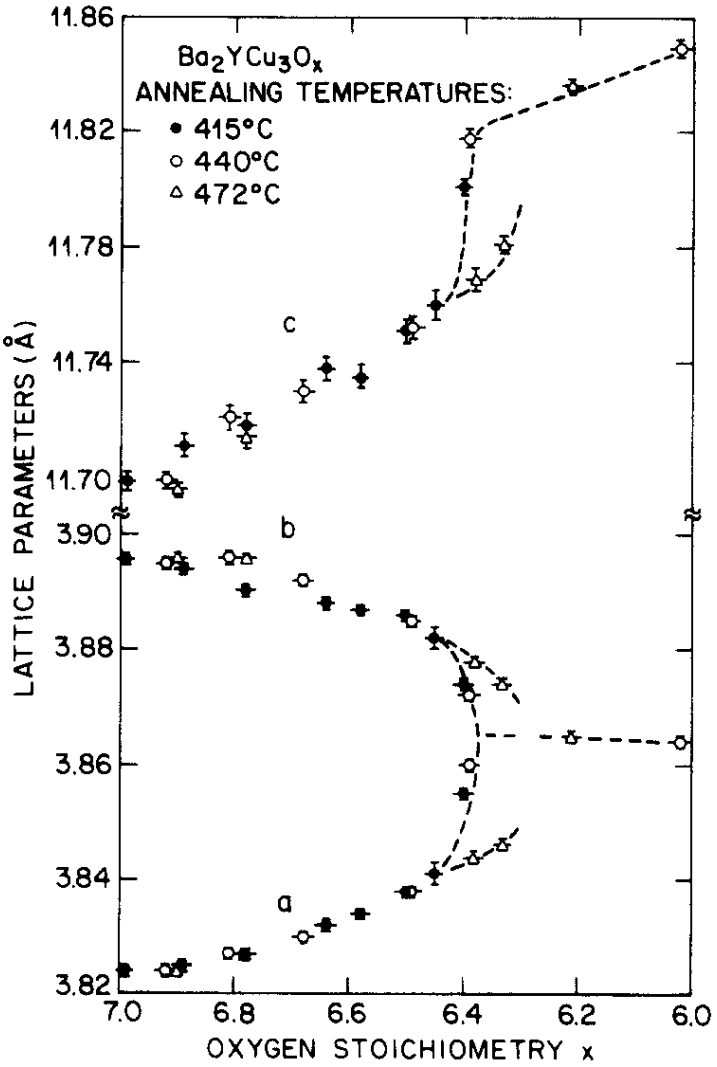

Figure 2.2: Lattice parameter dependence of $YBa_2Cu_3O_{7-\delta}$ on oxygen content δ for different annealing temperatures. Reprinted from R. J. Cava *et al.*, Physica C: Superconductivity 156.4, 523. Copyright (1988), with permission from Elsevier [66].

2.2 Electronic Properties upon Oxygen Depletion

In addition to changing the material's crystallographic structure, the variation of oxygen content in $YBa_2Cu_3O_{7-\delta}$ also strongly affects its electronic transport properties in the normal and superconducting state. An insulating state is found for low oxygen content due to antiferromagnetic ordering of magnetic moments in the $Cu(2)O_2$ layers. Upon increasing oxygen content, the $Cu(1)O_{1-\delta}$ chains dope the $Cu(2)O_2$ planes by hole injection. The doping allows for the formation of the superconducting state, as shown in figure 2.3, and gives rise to the 60 K and 90 K plateaus of the superconducting transition temperature by short range ordering of oxygen in $Cu(1)O_{1-\delta}$ chains.

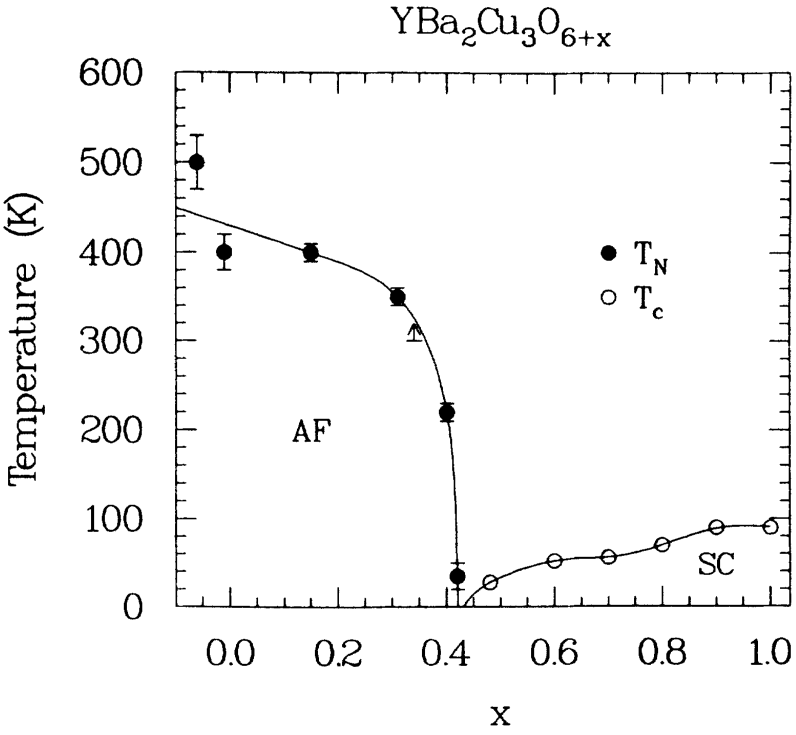

Figure 2.3: Influence of oxygen content x on critical superconducting transition temperature T_c in $YBa_2Cu_3O_{6+x}$ illustrating the underdoped antiferromagnetic regime and electronic transition into the superconducting state. Reprinted figure with permission from J. M. Tranquada *et al.*, Phys. Rev. B., 38.4, 2477 (1988). Copyright (1988) by the American Physical Society [67].

Uimin and Rossat-Mignod [65] numerically analyzed the free energy for various configurations of oxygen within the basal plane. The Cu(1) atoms of the basal plane were found to be bound to a Cu^+ charged state by the apical oxygen atoms in fully reduced $YBa_2Cu_3O_6$. Increasing the oxygen content, initially, the basal oxygen atoms were found to be randomly distributed at O(4) and O(5) sites.

Upon further oxygen increase, first, Cu^{2+} - O^{2-} - Cu^{2+} monomers are formed by covalent bonding of $Cu^+ d_{x^2-y^2}$ orbitals with adjacent O2p orbitals. Adding oxygen atoms, $Cu(1)O_{1-\delta}$ chain fragments are formed with oxygen atoms additional to the monomers being in O^- monovalent charge state [68]. It is now energetically favorable for electrons of the $Cu(2)O_2$ layer to be bound to the $Cu(1)O_{1-\delta}$ chains. This localization of $Cu(2)O_2$ layer electrons in the $Cu(1)O_{1-\delta}$ chains can be equivalently

explained in the hole picture as doping by hole injection from the $Cu(1)O_{1-\delta}$ chain hole reservoir.

Strong reduction of the superconducting transition temperature T_c for underdoped $YBa_2Cu_3O_{7-\delta}$ is reported after quenching of annealed samples in liquid nitrogen [69]. This is assigned to the freezing of a high-temperature equilibrium distribution of oxygen atoms on O(4) and O(5) sites. Thus, the charge carrier concentration also depends on the arrangement of oxygen atoms within the $Cu(1)O_{1-\delta}$ chains for given doping. However, T_c reduction by quenching is not significant for optimally doped $YBa_2Cu_3O_{7-\delta}$, probably due to the stable oxygen content within the doping plateau.

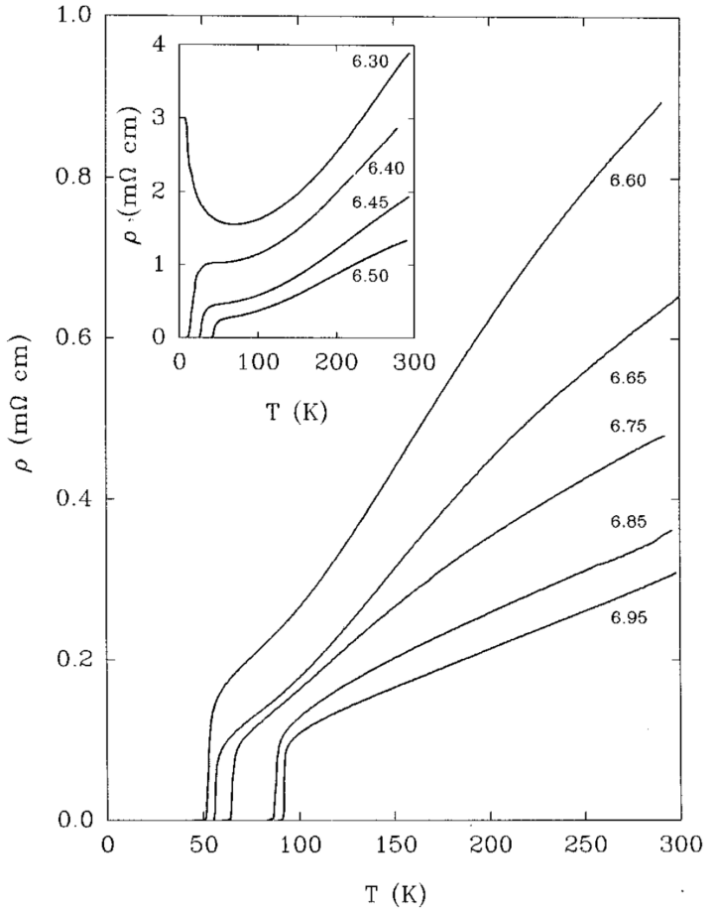

Figure 2.4: Temperature dependence of resistivity for varying oxygen content in $YBa_2Cu_3O_x$. Reprinted figure with permission from B. Wuyts *et al.*, Phys. Rev. B., 53.14, 9418 (1996). Copyright (1996) by the American Physical Society [70].

In general, T_c decreases and the normal-state resistivity ρ increases upon oxygen depletion of $YBa_2Cu_3O_{7-\delta}$ (fig. 2.4). An overview on characteristic properties of temperature and oxygen content dependence on resistivity is given below.

1. Strongly underdoped charge carrier concentration ($\delta > 0.66$):
   - The antiferromagnetic ordering leads to an insulating state.
   - There is no transition into the superconducting state at any temperature.

2. Slightly underdoped charge carrier concentration:

   - Increasing the charge carrier concentration above the antiferromagnetic threshold allows for a superconducting transition with $T_c(\delta)$ (fig. 2.3).
   - The normal-state resistivity shows metallic onset and nonlinear behavior below a temperature T^* related to the pseudogap phase. There are semiconducting features above T_c, as shown for $x = 6.40$ in figure 2.4.

3. Optimally doped charge carrier concentration:

   - The normal-state resistivity is linear and thus metallic. Superconducting fluctuations in the onset of the superconducting transition evoke paraconductivity and therefore the resistivity falls below a linear metallic behavior [71].
   - Superconducting transition widths ΔT_c are small. T_c changes only marginally for slight variations in oxygen content due to the $T_c(\delta)$ plateau.

2.3 Defect Creation by Ion Irradiation

There are two main reasons of high technological importance for research on irradiation of HTS. First, defects in HTS increase the pinning potential of vortices, hence higher critical currents can be applied. Second, superconducting electronics requires precise knowledge on modification of electronic transport properties, such as the microscopic manipulation of vortex motion.

Several parameters influence the defect creation by ion irradiation, such as ion species, ion kinetic energy, angle of incidence as well as composition, structure and dimensions of the target. For given ion species and target material, the ion's kinetic energy determines its penetration range. The atomic number defines the ion's mass and charge distribution, which in turn determines the creation of characteristic defect types. Particles of low mass, such as electrons, protons or light ions, produce point defects and finite defect clusters [72], whereas massive particles produce primary knock-on atoms of high energy. The primary knock-on atoms create collision cascades within the target, resulting in extended defects. Hence, irradiation with heavy ions of high energy is used to create columnar defect tracks to enhance vortex pinning [38].

To locally modify vortex pinning potentials, the superconducting transition temperature T_c needs to be suppressed in confined areas. However, other material properties are aimed to stay unaltered, which is best accomplished by introducing point defects in the $Cu(2)O_2$ plane. Point defects are created if the energy transfer of the incident ion to target atoms is higher than the atoms' displacement energy, without significantly exceeding this value, which implies the use of light-ion irradiation.

Strong T_c suppression is achieved by introducing about one defect per YBCO unit cell [73], corresponding to about 1/13 defects per atom. On the one hand, increasing the ion's kinetic energy extends its penetration range. This is particularly important to avoid ion implantation and to ensure spatially homogeneous defect

density. On the other hand, the energy transfer decreases for higher kinetic energy. Thus, irradiation fluence needs to be increased to create a given defect density. To reach feasible fluences, the irradiation needs to be performed on thin films.

Along these lines, Dineva-Stavreva [74] investigated the optimization of irradiation parameters using computer simulations. It was found that low energy proton irradiation results in only slight lateral straggling (fig. 2.5a). However, due to its low mass, high fluences are required to create practical defect densities. Irradiation with He^+ ions of 75 keV kinetic energy was found to allow for a resolution of about 10 nm lateral straggle in 100 nm depth with defect densities at feasible ion fluences, creating clusters of mostly oxygen vacancies along the ion path (fig. 2.5b).

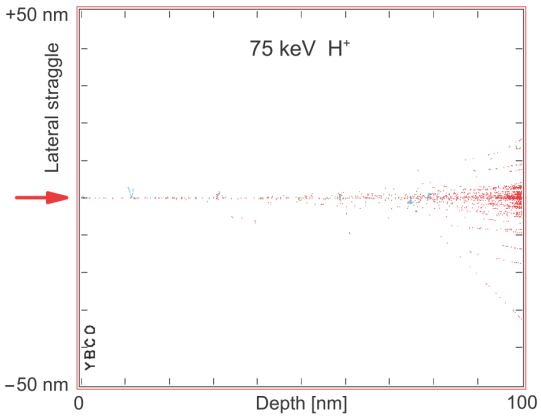

a) Irradiation with 75 keV H^+ yields 0.5 defects/ion with T = 99.7% at 100 nm depth.

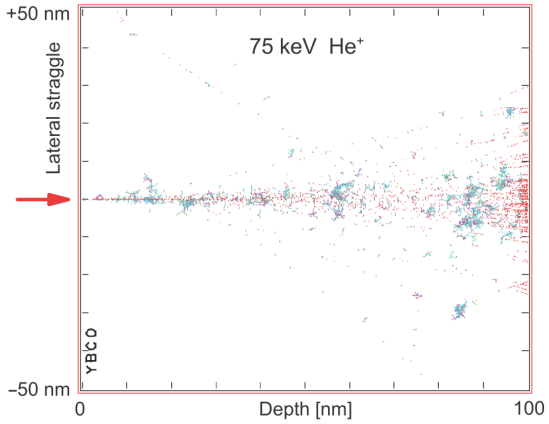

b) Irradiation with 75 keV He^+ yields 9.7 defects/ion with T = 99% at 100 nm depth.

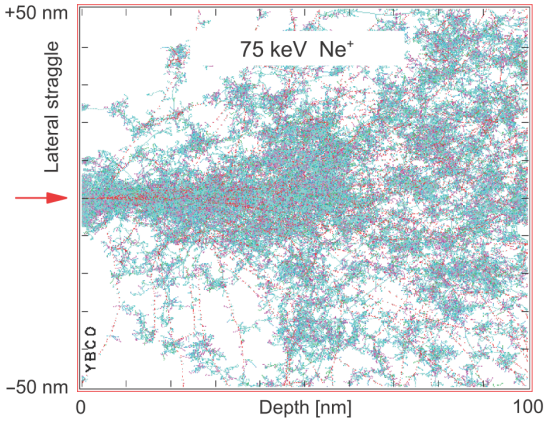

c) Irradiation with 75 keV Ne^+ yields 476 defects/ion with T = 37% at 100 nm depth.

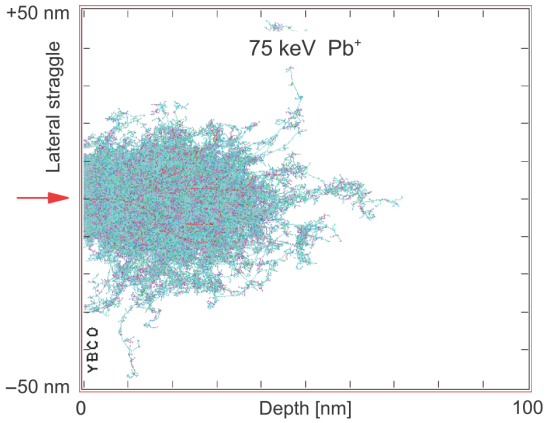

d) 75 keV Pb^+ irradiation creates a large amount of defects and full implantation.

Figure 2.5: Computer simulations of $YBa_2Cu_3O_{7-\delta}$ irradiation with 100 ions of different species at 75 keV. The figures show the 2D projection onto the incident plane of a 3D vacancy distribution created by ions (red dots) and vacancies created in collision cascades (O (*blue*), Cu (*magenta*), Y (*green*), Ba (*purple*)), respectively. The direction of the incident ion beam is indicated by a red arrow. The transmittance T of ions is given in the subcaptions. Reprinted by permission from Springer Customer Service Centre GmbH: Springer Nature, *Nanoscience and Engineering in Superconductivity* by V. Moshchalkov, R. Woerdenweber and W. Lang [75], copyright (2010).

Ne^+ and Pb^+ irradiation was shown to create many collision cascades producing a high amount of displacements. Moreover, Y and Ba atoms are displaced more frequently due to the ions' higher masses. For 75 keV Ne^+ irradiation the defect clumps are widely spread (fig. 2.5c), thus it is not suited for high-resolution patterning of YBCO. 75 keV Pb^+ ions are fully implanted and the material along the ion trajectory becomes amorphous (fig. 2.5d), creating large defect tracks.

To conclude, Dineva-Stavreva [74] found that He^+ ions at energies ranging from 60 to 100 keV are most suitable for creating a homogeneous distribution of point defects in thin films of $YBa_2Cu_3O_{7-\delta}$ with low lateral straggling at feasible ion fluences.

X-ray diffraction analysis of $YBa_2Cu_3O_{7-\delta}$ thin films irradiated with 75 keV He^+ ions at various doses shows reduced intensity of the $(00l)$ peak up to a fluence of 5×10^{15} cm^{-2} [76], which is attributed to increasing oxygen disorder and defect density. The crystal structure is reported to be unchanged upon irradiation [77] up to a a fluence of 10^{16} cm^{-2}, at which the sample becomes amorphous [76].

2.4 Electronic Properties after Ion Irradiation

In this section, electronic properties of $YBa_2Cu_3O_{7-\delta}$ thin films after 75keV He^+ irradiation with cumulative doses up to a fluence of 10^{16} cm^{-2} are discussed. Most of the investigations presented in this section were performed by Enzenhofer [78].

The normal-state resistivity was found to increase exponentially with the applied dose (fig. 2.6), which is in agreement with investigations performed by Marwick et al. [79]. The exponential increase in resistivity for 100 K and 300 K intersects at a fluence of 3×10^{15} cm^{-2}. This indicates a transition from metallic to semiconducting behavior, since for the 300 K data, resistivity is reduced by thermally activated charge carriers above this fluence, whereas phonon scattering is responsible for the increase in resistivity below this fluence for the 100 K data, respectively.

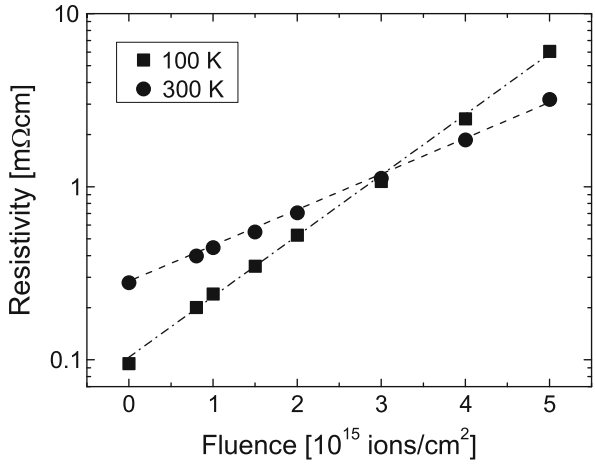

Figure 2.6: Resistivity dependence on fluence for 100 K and 300 K. Reprinted by permission from Springer Customer Service Centre GmbH: Springer Nature, *Nanoscience and Engineering in Superconductivity* by V. Moshchalkov, R. Woerdenweber and W. Lang [75], copyright (2010).

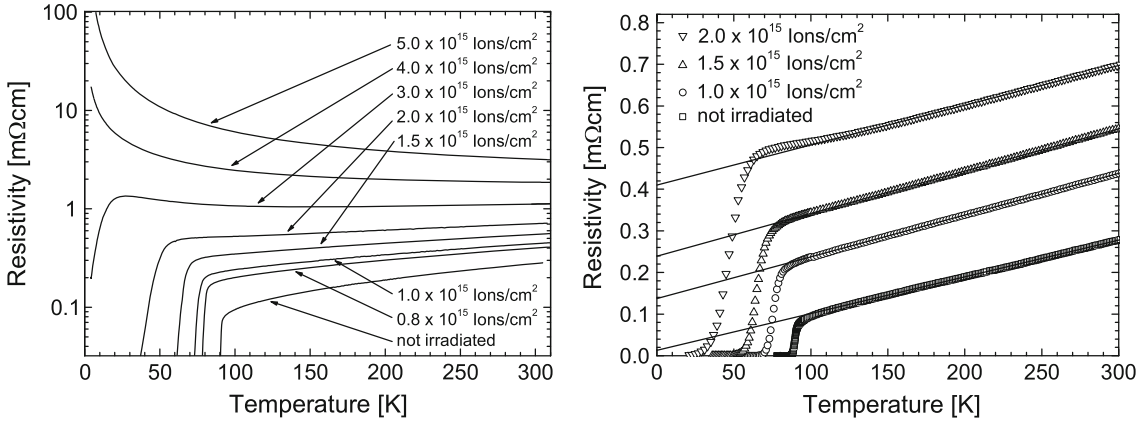

a) Resistivity dependence on temperature for various irradiation fluences.

b) Linear fit on $\rho(T)$ shows the same slope for moderate fluences.

Figure 2.7: Temperature dependence of resistivity for 75 keV He^+ irradiation of $YBa_2Cu_3O_{7-\delta}$ for several doses. Sharp superconducting transitions and constant slope of normal-state resistivity are observed for fluences below 3×10^{15} cm^{-2}, which also marks the transition from metallic to semiconducting behavior. Note the semilogarithmic scale in figure 2.7a. Reprinted by permission from Springer Customer Service Centre GmbH: Springer Nature, *Nanoscience and Engineering in Superconductivity* by V. Moshchalkov, R. Woerdenweber and W. Lang [75], copyright (2010).

The superconducting transition temperature T_c progressively decreases upon irradiation, with the transition width ΔT_c remaining sharp (fig. 2.7a). The slope in the normal-state resistivity is linear, and most notably, constant, up to a fluence of 2×10^{15} cm^{-2} (fig. 2.7b). These findings can be qualitatively interpreted in the Drude model [80] of a free charge carrier gas, where the temperature dependence of the resistivity $\rho(T)$, is described by equation 2.1, with charge carrier density n, mass m, mobility μ, characteristic scattering time τ and elementary charge e.

$$\rho(T) = \frac{1}{ne\mu(T)} + \rho_0 = \frac{m}{ne^2\tau(T)} + \rho_0 \tag{2.1}$$

In a classical metal, the charge carrier density $n(T) = n$ is temperature independent. The resistivity is linear in T for moderate temperatures due to phonon scattering of charge carriers. For low temperatures the resistivity of metals, first, decreases proportional to T^5 and ultimately heads to a finite residual resistivity ρ_0 due to defect scattering of charge carriers. However, the latter case is not observed here, since the material either becomes superconducting or semiconducting in this temperature range.

Following these explanations, a constant slope up to a fluence of 2×10^{15} cm^{-2}, as presented in figure 2.7b, implies that charge carrier concentration is not altered upon moderate irradiation [81]. This is in contrast to the temperature dependence on resistivity upon oxygen depletion, where the slope of the normal-state resistivity increases or even becomes nonlinear (fig. 2.4). Furthermore, the normal-state extrapolation of residual resistivity ρ_0 at zero temperature increases with irradiation fluence. This indicates increasing defect density, which in turn reduces the charac-

teristic scattering time τ, implying decreasing charge carrier mobility μ.

These findings are supported by measurements of the Hall angle $\tan\theta_H = \mu B$. The Hall angle follows Anderson's law [82] in the normal state, which predicts a quadratic temperature dependence due to hole-hole scattering, with α being proportional to the charge carrier density n.

$$\cot\theta_H = \alpha T^2 + C \tag{2.2}$$

Figure 2.8a shows that the Hall angle indeed follows the quadratic scaling. Again, the slope α, and thus the charge carrier density, is unchanged upon moderate irradiation, and only slightly changed upon irradiation with a fluence of 3×10^{15} cm^{-2}. Both, the increase in offset C (fig. 2.8a), as well as the linear decrease in charge carrier mobility with increasing fluence (fig. 2.8b) can be associated to an increase in defect scattering [83].

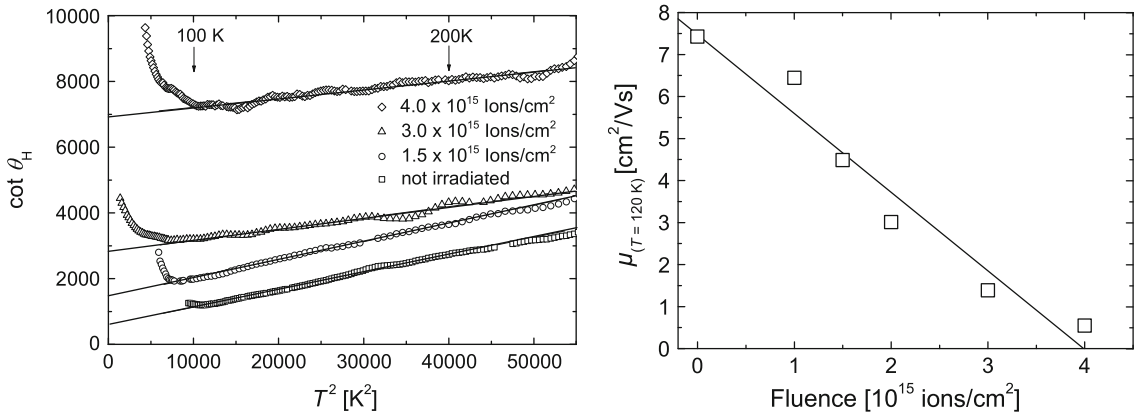

a) Quadratic temperature dependence of $\cot\theta_H$ for various fluences.

b) Linear dependence of the mobility μ on irradiation fluence at 120 K.

Figure 2.8: Hall angle dependence θ_H on the temperature and cumulative fluence. Full lines represent fits to the Anderson model (a) and linear fit (b), respectively. Reprinted by permission from Springer Customer Service Centre GmbH: Springer Nature, *Nanoscience and Engineering in Superconductivity* by V. Moshchalkov, R. Woerdenweber and W. Lang [75], copyright (2010).

In conclusion, the narrow transition width ΔT_c, the constant slope in $\rho(T)$, the steady increase in residual resistivity ρ_0 as well as mobility measurements on the Hall angle imply that the charge carrier density is unaltered and defect density is increased upon 75 keV He^+ irradiation with moderate fluences [76]. These finding are consistent with the conclusion of Valles et al. [84] and White et al. [85], stating that the suppression of superconducting transition temperature is caused by a reduction in charge carrier mobility due to increased defect scattering.

To distinguish between the influence of chain and plane oxygen displacements on the electronic properties, Tolpygo et al. [86] investigated defect creation for several energies of electron irradiation. They compared the reduction of T_c created by electron irradiation to data of T_c reduction for Zn substitutions, which act as in-plane defects in the Cu sublattice and found consistency in T_c suppression [87].

They interpret their results as having found a threshold value of electron irradiation of about 58 keV at which in-plane oxygen atoms would be displaced, considering a maximum energy transfer calculation for elastic electron-atom collisions. A fit of the Mott-Rutherford displacement cross section suggests an in-plane oxygen displacement energy of 8.4 eV [73].

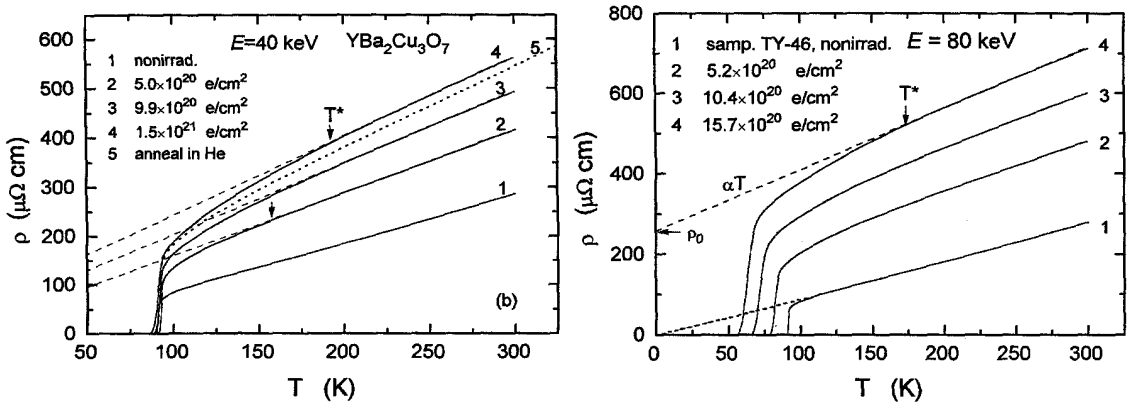

a) $\rho(T)$ for 40 keV e^- irradiation **b)** $\rho(T)$ for 80 keV e^- irradiation

Figure 2.9: Resistivity dependence on temperature for optimally doped $YBa_2Cu_3O_{7-\delta}$ after irradiation with electron irradiation energies below (40 keV) and above (80 keV) the threshold energy for CuO_2 in-plane oxygen displacements at different fluences. Dashed lines indicate linear fits up to a pseudogap temperature T^*. Reprinted from S. K. Tolpygo *et al.*, Physica C: Superconductivity 269.3-4, 207. Copyright (1996), with permission from Elsevier [86].

The measurements presented in figure 2.9a on electron irradiation energies below the threshold energy for CuO_2 in-plane oxygen displacements are consistent with He^+ irradiation data, regarding increasing normal-state resistivity, strong enhancement of residual resistivity ρ_0 and only slight variations in T-linear resistivity slope. Tolpygo et al. interpret these results as being caused by chain oxygen disorder induced by irradiation defects. However, the onset of a pseudogap for temperatures below T^* is inconsistent with the constant slope found for 75 keV He^+ irradiation presented in figure 2.7b. This implies that the cross section for electron-atom collisions favors chain oxygen displacements, which might slightly reduce charge carrier density compared to 75 keV He^+ irradiation.

However, the superconducting transition temperature T_c is obviously stable upon electron irradiation below the in-plane oxygen displacement energy threshold. This implies that the charge carrier density can not be strongly decreased. Tolpygo et al. explain this result by concluding that the increasing resistivity predominantly arises due to disrupted CuO chain conductivity [86].

This reasoning is supported by measurements showing that the crystal structure at complete T_c suppression upon irradiation is still orthorhombic [88]. If T_c was suppressed by reduced charge carrier density due to oxygen disorder in the CuO basal plane, a transition to tetragonal structural is expected to occur. Further support is given by Wang et al. [89], who found no significant difference in T_c for optimally doped $GdBa_2Cu_3O_{7-\delta}$ synthesized in tetragonal and orthorhombic structure. Hence,

oxygen disordering in the $CuO_{1-\delta}$ plane does not destroy high-temperature superconductivity [89].

For electron irradiation energies above the CuO_2 in-plane oxygen displacement threshold, a systematic reduction in T_c is observed (fig. 2.9b). If the findings on threshold energy are correct, mainly in-plane oxygen defects would cause T_c suppression and interstitial oxygen atoms from $CuO_{1-\delta}$ displacements would give an insignificant contribution. However, these findings are in agreement with previous reports on T_c being sensitive on both O and Cu displacements [88].

Tolpygo et al. [87] found that T_c suppression is a universal function of the impurity scattering rate τ_{imp}^{-1}, obtained from resistivity and Hall measurements. Furthermore, T_c suppression was found to be consistent with pair-breaking theory (eq. 4.3), assuming the defects which evoke the impurity scattering rate τ_{imp}^{-1} in resistivity measurements act as potential scatterers. However, this implies that the pair-breaking scattering rate $\Gamma = \tau_{\text{pb}}^{-1} \sim 0.3 \cdot \tau_{\text{imp}}^{-1}$ is only a third of the impurity scattering rate.

This is consistent with the superconducting energy gap $\Delta(\vec{k})$ being anisotropic, as $\Delta(\vec{k})$ is reduced in specific directions only, whereas impurity scattering contributes to resistivity in any scattering direction. Thus, these results are consistent with anisotropic pairing mechanism of superconductivity in $YBa_2Cu_3O_{7-\delta}$ [73].

3 Introduction to SRIM

In this introductory chapter basic concepts of the TRIM program are presented. An overview on the theoretical background of monolayer-collision-steps calculation for light ions at low energy is given [90].

The Transport of Ions in Matter (TRIM) [91] is part of a computer program called SRIM (The Stopping and Range of Ions in Matter), which computes the energy loss and final spatial distribution of ions, the production of phonons and plasmons, as well as collision cascades and the sputtering of target atoms in solid, liquid or gaseous phase. It uses approximations to quantum mechanical screened interaction potentials and a statistical Monte Carlo algorithm to compute nuclear and electronic stopping cross-sections in amorphous targets, with a maximum of eight layers, each of which can be a compound. Crystal channeling, thermal effects, diffusion and recrystallization are not considered.

Ions can lose energy by nuclear and electronic stopping in collisions with target atoms and their electronic charge distribution. The first basic approximation used in the program is the separation of both contributions, which leads to loss of correlation between nuclear and electronic scattering. This can usually be neglected, except for thin targets.

The second approximation reduces the calculation of scattering with target nuclei to a binary collision between two atoms with screened potentials. The energy loss of the incident ion to the target atom as well as the scattering angle are determined. Inelastic energy loss depends on the binding of the electrons to the target atom, i. e. its orbital structure, and the accessible energy levels for the electrons in the band structure itself.

The concept of the *free-flight-path* approximation enables to save computing time, particularly for ions with high energies, by skipping calculations of collisions with negligible impact on energy loss and deflection angle. The *Monolayer Collision Steps* calculation used in this thesis does not make use of the *free-flight-path* approximation, thus forcing TRIM to account for collisions in every monolayer.

3.1 Elastic Nuclear Energy Loss

The scattering of two atoms is described in the center of mass coordinate system with zero net momentum. In this system, the final scatter angle Θ can be calculated according to equation 3.1. It depends on the impact parameter p, the initial kinetic energy $E_c = \frac{1}{2} m_c v_0^2$ in the center of mass system and the interatomic potential $V(r)$, with r being the distance between incident and target atom. The reduced mass of the collision partners is denoted by m_c and v_0 is the initial velocity of the incident

atom in the laboratory system.

$$\Theta(E_c, p) = \pi - 2 \int_{r_{\min}}^{\infty} \frac{p}{r^2 \left[1 - \frac{V(r)}{E_c} - \frac{p^2}{r^2}\right]^{\frac{1}{2}}} dr \tag{3.1}$$

The scatter angle of the incident atom ϑ and the recoil angle of the target atom ϕ in the laboratory system can be obtained by equations 3.2 and 3.3, if the scatter angle Θ in the center of mass system is known.

$$\phi = \frac{1}{2}(\pi - \Theta) \tag{3.2}$$

$$\vartheta = \arctan\left(\frac{m_2 \sin\Theta}{(m_1 + m_2)\cos\Theta}\right) \tag{3.3}$$

The amount of energy T transferred from incident atom with mass m_1 to the recoiling atom with mass m_2 depends on the scatter angle Θ.

$$T(E_c, p) = 4E_c \frac{m_c}{m_2} \sin^2\frac{\Theta}{2} \tag{3.4}$$

The nuclear stopping cross-section $S_n(E_c)$ is the mean energy transfer per collision and obtained by integrating equation 3.4 over all impact parameters.

$$S_n(E_c) = \int_0^{\infty} T d\sigma = \int_0^{\infty} T(E_c, p) 2\pi p dp \tag{3.5}$$

The ion's kinetic energy loss per unit path length is the nuclear stopping cross-section $S_n(E_c)$ times the target density.

3.2 The Interatomic Potential $V(r)$

To determine the scattering angle in equation 3.1, the *interatomic potential* $V(r)$, with its origin at the center of mass, must be determined. The total interatomic potential consists of contributions from the Coulomb interaction between the nuclei, electronic interaction of both charge densities, interactions of the nuclei with the charge density of the opposite atom, the increase in kinetic energy by Pauli repulsion due to the Fermi statistics for electrons, and an increase in exchange energy due to electronic spin repulsion.

To calculate the interatomic potential $V(r)$, TRIM assumes that both charge distributions remain undisturbed during the collision, such that the aforementioned contributions solely depend on the atomic charge distributions $\rho(r)$ of both atoms, respectively. In TRIM, the charge distribution is either calculated using a local density approximation, or by extended Hartree-Fock-Slater solid-state charge distributions, depending on the target element. Both account for the orbital electronic structure, exchange and correlation effects. To ensure a central field potential $V(r)$, the spherical symmetry of the charge distribution $\rho(r)$ is obtained by taking a radial

mean value.

An analytical function to calculate an approximation to the elaborate interatomic potential $V(r)$ can be obtained by introducing the *interatomic screening function* $\Phi_I(r)$ (eq. 3.6). It is defined as the deviation of a sole Coulomb interaction between two nuclei with atomic numbers Z_1, Z_2 and elementary charge e, with respect to the actual interatomic potential.

$$V(r) = \frac{Z_1 Z_2 e^2}{r} \Phi_I(r) \tag{3.6}$$

To avoid large databases of interatomic potentials for all possible combinations of atomic collisions, the interatomic screening function $\Phi_I(r)$ is calculated from sophisticated interatomic potential simulations for 522 random pairs of collision partners. The obtained screening function data is fitted with an exponential series to obtain the *universal screening function* $\Phi_U(R)$, where the reduced radial coordinate $R = r/a_U$ is normalized by a fitted *universal screening length* a_U. The universal screening function $\Phi_U(R)$ is used to compute all interatomic potentials analytically and is in good agreement with experimental data.

3.3 The Magic Formula of Scattering

Biersack and Haggmark [92] proposed the so called *Magic Formula of Scattering* (eq. 3.7, which allows for an analytical calculation of the scattering angle (eq. 3.1), using the initial velocity and impact parameter.

$$\cos\frac{\Theta}{2} = \frac{B + R_c + \Delta}{R_0 + R_c} \tag{3.7}$$

The impact parameter B, the distance of closest approach R_0, the sum of the radii of closest approach R_c and the correction term Δ are given in reduced units of the universal screening length a_U. R_0 and R_c depend on the actual interatomic potential $V(R)$. The correction term Δ must be fitted to the screened universal interatomic potential for accurately describing low energy ions in the screened Coulomb potential regime.

3.4 Inelastic Electronic Energy Loss

The description of an ion's kinetic energy loss to the electrons in a solid is rather complex, due to the mutual interaction between the local target charge density and the ion charge density.

The interaction strength $I(v, \rho)$ between the ion and a free electron gas with density ρ is strongly velocity v dependent. I decreases with increasing electron density ρ, since the Fermi velocity of the conduction electrons increases $\propto \rho^{1/3}$, leading to adiabatic scattering. For low velocity ions, there is little excitation of target core electrons and most of the inelastic energy is absorbed by outer shell electrons, since the velocity of core electrons is too high to allow for absorption.

However, since the electronic stopping power in a free electron gas is given by the interaction strength I times the local electron density ρ, the Lindhard stopping

formalism shows increasing stopping cross-section S_e for increasing electron density ρ, with a flattening due to the decreasing interaction strength.

TRIM uses a local density approximation with the Lindhard stopping formalism for the interaction strength $I(v, \rho)$ for hydrogen ions with effective charge Z^* and solid-state Hartree-Fock charge density distributions to compute the electronic stopping cross-section S_e.

$$S_e = \int I(v, \rho) \Big(Z_1^*(v) \Big)^2 \rho dx^3 \tag{3.8}$$

The hydrogen ion is assumed to be fully ionized, such that the charge of a proton is +1 for all velocities throughout all computational steps, since the electron of the H1s orbital would be delocalized over several lattice sites.

The effective charge for He^+ ions is found by fitting experimental data on stopping powers with respect to proton stopping powers. The formalism for heavy ions and relativistic velocities is not discussed here, but explanations and further literature can be found in the book of Ziegler et al. [90].

3.5 The Calculation of Target Damage

An incident atom with atomic number Z_1 and energy E collides with a resting target with atomic number Z_2, such that E_1 and E_2 are the energies of the atoms after collision, respectively. The following cases need to be considered:

- Creation of a **displacement**: If the energy E_2 of the target atom is higher than the element's displacement energy $E_2 > E_d$, it is knocked out of its lattice site and a displacement is created. Additionally, it will lose the amount of binding energy E_b to the lattice as phonons. It will now be considered as an incident atom in the collision cascade, unless its remaining energy is smaller than a final cutoff energy E_f. Now the following possibilities occur:
  - Creation of a **vacancy**: If the energy of the incident atom $E_1 > E_d$ is greater then the displacement energy as well, it is not stuck at the lattice site. Thus a vacancy is created in the subset of displacements. E_b is subtracted from the incident atom and released as phonons, as it passes the lattice site.
  - Creation of a **replacement**: If $Z_1 = Z_2$ and $E_1 < E_d$, the incident atom is captured by the lattice site, since it can not overcome the displacement potential. Thus, the replacement is a subset of displacements. The energy E_1 is released as phonons. In the case of $Z_1 \neq Z_2$ the atom is considered an **interstitial**.
- Consider $E_2 < E_d$, such that the target atom can not leave its lattice site. There are two possibilities for the incident atom:
  - If $E_1 < E_d$, the incident atom becomes an **interstitial**, such that E_1 and E_2 are released as phonons.
  - If $E_1 > E_d$, the incident atom continues the collision cascade. E_2 is released as phonons.

The collision of an ion with a primary target atom causes a recoil cascade, if the transferred energy is higher than the displacement energy E_d. The recoil energy decreases due to the creation of displacements: vacancies, interstitials and replacements with atoms of same kind. Replacements with unlike elements are considered interstitials. The replacements of same elements in consecutive cascades is not accounted for.

The selection of target atoms is randomly distributed with respect to their relative abundance in the compound layer. The impact parameter is not affected by cross-section calculations, since range and energy transfer are governed solely by the interaction potential.

The Kinchin-Pease Model is an analytic approximation for computing target damage. It is not used in the *Monolayer Collision Steps* calculation due to its poor spatial defect resolution, since it projects the full damage to the location of the primary recoil. Phase and compound corrections, as well as ion straggling are not discussed here, since it is not required for the determination of the defect distribution.

4 SRIM Simulation and Data Processing

In this chapter, the simulation setup and the subsequent processing of acquired data is presented. The calculated displacement coordinates are read in and redistributed according to uniform irradiation through stencil mask holes and irradiation by a defocused He^+ microscope. 3D T_c profiles of the nanostructured samples are obtained by calculating T_c from damage profiles.

4.1 TRIM Simulation Setup

The *TRIM* setup window offers several setting options leading to differing outcomes (fig 4.1). In this simulation, first, the *DAMAGE type* calculation is set to *Monolayer Collision Steps* to force a calculation of ion-atom interaction and atom-atom collision cascade in each target layer, thus disabling the *free-flight-path* approximation. Next, He is selected as the incident ion species and its energy defined as 75 keV and 30 keV in the first and second run, respectively. The angle of incidence is set to 0° to calculate damage cascades at normal incidence.

A YBCO target layer with density (6.3 g cm^{-3} [93]) and width (2100 Å) needs to be initialized. The target layer is constructed by adding its compound elements with their respective stoichiometric abundance. In prior simulations, the difference in displacement energy E_d for chain and plane oxygen was not considered. However, to account for this difference, two separate oxygen compound elements need to be defined. Hence, the elements are selected and the compound abundance for Y (1/13), Ba (2/13), Cu (3/13), plane and apical O (6/13) as well as chain O (1/13) is entered into the field *Atom Stoich or %*.

The default displacement energy E_d of each compound needs to be changed to obtain accurate collision cascade calculations. The displacement energy for chain oxygen atoms was calculated by Cui et al. [94] using molecular dynamics simulations. Observing changes in the oxygen partial radial pair distribution function upon varying ion energies, the chain oxygen displacement energy $E_d^{\text{O-c}}$ from O(4) to O(5) site was found to be 1.5 eV. Furthermore, oxygen displacements of other lattice sites were shown to have displacement energies below 9 eV. In this simulation $E_d^{\text{O-c}} = 1$ eV was used, which does not significantly alter the collision cascades.

For Cu, a displacement energy E_d^{Cu} of 15 eV was experimentally determined by Legris et al. [88]. The linear decrease of T_c with respect to fluence Φ is determined for several electron irradiation energies from 0.1 MeV to 2.4 MeV. The decrease rate $\Delta T_c/\Delta\Phi$ as a function of electron energy is fitted using calculated displacement cross-sections, with E_d^{Cu} as fitting variable. Similarly, Tolpygo et al. [73] report the displacement energy for plane oxygen atoms being $E_d^{\text{O-p}} = 8.4$ eV determined by fitting the decrease rate $\Delta T_c/\Delta\Phi$ as a function of electron energy from 20 keV to 120 keV using the Mott-Rutherford displacement cross section. Displacement ener-

gies for Y and Ba are set to 35 eV.

The number of ions considered in the SRIM simulation has to be adapted to the fluence Φ from irradiation experiments in [81]. The effective surface irradiated with He^+ ions is the area of holes in the silicon mask. Thus, the number of ions per mask hole of diameter $d = (180 \pm 5)$ nm for a given fluence can be calculated according to equation 4.1. Results are presented in table 4.1.

$$N_{\text{Ions}} = \Phi \cdot \frac{d^2}{4}\pi \tag{4.1}$$

$\Phi\left[10^{15}\frac{\text{Ions}}{\text{cm}^2}\right]$	N_{Ions}
0.8	203,575
1.0	254,469
1.5	381,704
2	508,938
3	763,407
(3.4)	(868,906)

Table 4.1: Fluences of experimentally applied irradiation with 75 keV He^+ ions and corresponding number of ions per mask hole. The value in brackets is a conversion from published fluences of 120 keV He^+ irradiation to corresponding fluences for 75 keV He^+ irradiation at $T_c = 0$, explained in chapter 4.4.3.

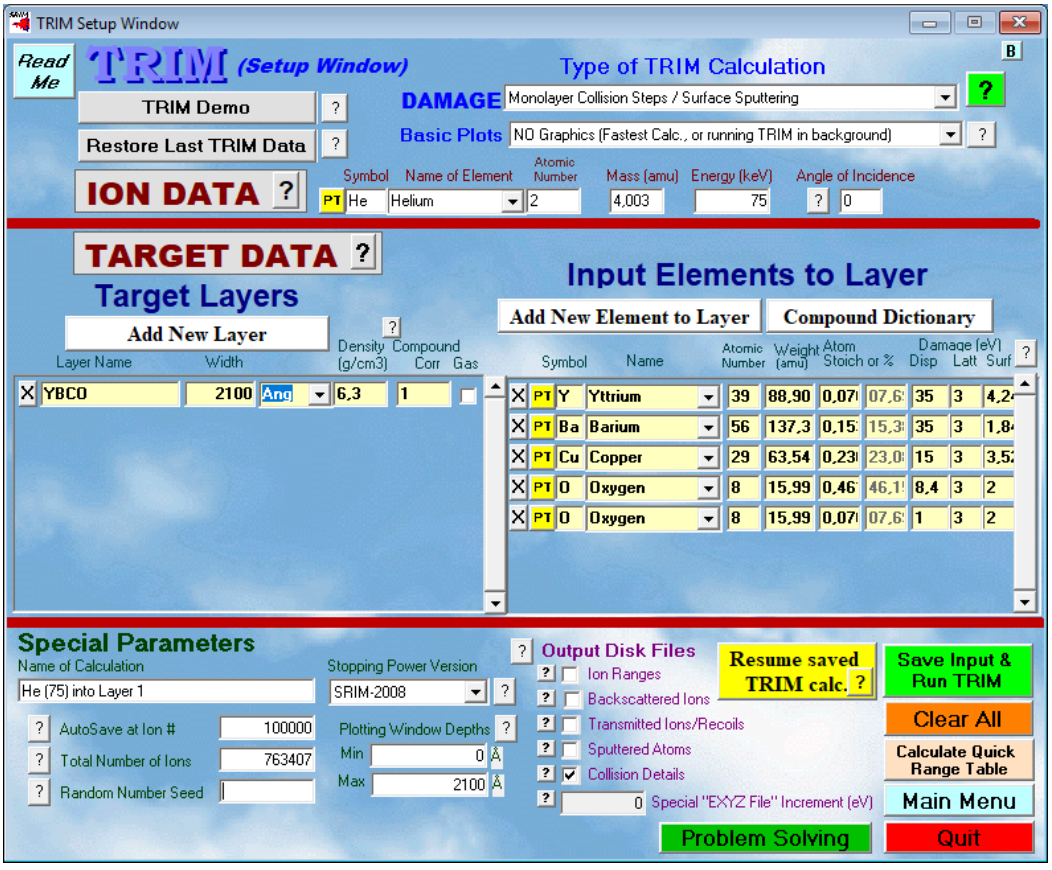

Figure 4.1: TRIM setup for simulation of 75 keV He^+ irradiation in $YBa_2Cu_3O_7$.

For 30 keV He^+ irradiation 50639 ions are considered, corresponding to a fluence of about 3×10^{15} cm^{-2} with Gaussian beam distribution with full width at half maximum (FWHM) of 27 nm.

The default random number seed of 716381 is used, which ensures equal outcomes for same input setup. This is particularly important for the correlation of ion trajectories of different calculation runs, e. g. in calculating the positions of transmitted ions using the `TRANSMIT.txt` output at several target layer depths.

4.2 TRIM Output Files

4.2.1 `TRANSMIT.txt`

A straightforward way to obtain the transmission of ions for a 3D visualization of fluence is to calculate the `TRANSMIT.txt` file for several target layer widths. An output example is given in figure 4.2. Each incident ion is numbered consecutively, whereas only transmitted ion are listed in this file. Backscattered or implanted ions are not considered. The last location of transmitted ions inside the target is listed with cosine values of the corresponding final trajectory. The y and z coordinates of each target width considered are needed to obtain a 2D mapping of the number of transmitted ions per cell area.

```
============================== SRIM-2013.00 ==============================
==========================================================================
=================  TRANSMIT.txt : File of Transmitted Ions  ==============
=  This file tabulates the kinetics of ions or atoms leaving the target.     =
=  Column #1: S= Sputtered Atom, B= Backscattered Ion, T= Transmitted Ion.   =
=  Col.#2: Ion Number, Col.#3: Z of atom leaving, Col.#4: Atom energy (eV).  =
=  Col.#5-7: Last location:  X= Depth into target, Y,Z= Transverse axes.     =
=  Col.#8-10: Cosines of final trajectory.                                   =
= *** This data file is in the same format as TRIM.DAT (see manual for uses).=
====== TRIM Calc.= He(75 keV) ==> YBCO( 2000 A) ==============================
 Ion  Atom   Energy        Depth       Lateral-Position        Atom Direction
 Numb Numb    (eV)          X(A)        Y(A)       Z(A)      Cos(X)  Cos(Y) Cos(Z)
T    1  2 .3308906E+05   2000405E-03  .2287E+03  .2583E+03   .7098216 -.5263877 -.4680484
T    2  2 .3269143E+05   2001565E-03  .3581E+03  .2705E+03   .6815792  .2877550  .6727904
T    3  2 .2641104E+05   2000221E-03 -.6226E+03  .9608E+03   .9704999 -.2374914  .0415662
T    4  2 .3511640E+05   2001503E-03  .2344E+03 -.1316E+03   .9361580  .2939434 -.1928871
T    5  2 .3264794E+05   2000551E-03  .4641E+03  .1490E+03   .9853067  .1704627  .0106375
```

Figure 4.2: Example output of the `TRANSMIT.txt` file for 75 keV He^+ irradiation in $YBa_2Cu_3O_7$ of 200 nm width.

4.2.2 `COLLISION.txt`

To obtain full collision cascade data, the *Collision Details* button and the *Storage of Recoils* is enabled, providing the `COLLISION.txt` file. The input settings of the TRIM setup are listed in the file header.

In case an ion collides with a target atom such that at least one displacement is caused, a new collision cascade is started (fig. 4.3). If the energy of the primary recoil atom is high enough additional recoil cascades might occur. Each displacement caused either by the primary recoil atom or any other atom in the recoil cascade is numbered consecutively and listed until the kinetic energy of each recoil atom is

below the smallest displacement energy. The atomic number, kinetic energy after collision and the initial coordinates of each collision partner are given. At this site, either a vacancy or a replacement is created. It is important to note that the lateral position of ions and displacements is not constricted to the lateral window size of the simulation, but followed indefinitely [90]. However, recoil atoms leaving the target are not further considered. The displacements created in the collision cascade are summarized below the last recoil atom considered.

```
  Ion    Energy    Depth     Lateral Distance (A)   Se    Atom  Recoil    Target Target Target Target
  Numb   (keV)      (A)       Y Axis    Z Axis    (eV/A)  Hit  Energy(eV) DISP.  VAC.   REPLAC INTER
-------------------------------------------------------------------------------------------------------
³00001³70,97E+00³16431,E-02³-1612,E-03³-1312,E-04³0023,27³ Ba ³14380,E-02³ <== Start of New Cascade  ³
=======================================================================
  Recoil Atom Energy(eV)   X (A)      Y (A)      Z (A)   Vac Repl Ion Numb 00001=
Û 00001   56  14380,E-02 1643,E-01 -1612,E-03 -1312,E-04  1   00 Û<ÄPrime RecoilÛ
Û 00002   29  73746,E-03 1654,E-01 -4039,E-03  3729,E-03  1   00 Û
Û 00003   08  93957,E-04 1687,E-01 -7338,E-03  3967,E-03  1   00 Û
Û 00004   08  30010,E-03 1671,E-01 -5600,E-03  3580,E-03  1   00 Û
Û 00005   08  15656,E-03 1689,E-01 -6241,E-03  5093,E-03  1   00 Û
Û 00006   29  45091,E-03 1644,E-01 -2817,E-03  1921,E-03  1   00 Û
Û 00007   08  50940,E-04 1690,E-01  5508,E-03 -1863,E-03  1   00 Û
Û 00008   08  96894,E-04 1651,E-01  1787,E-03  1059,E-03  1   00 Û
Û 00009   08  11083,E-03 1645,E-01 -4659,E-04  1545,E-03  1   00 Û
Û 00010   08  34315,E-04 1667,E-01  2734,E-03  1538,E-03  1   00 Û
=================================================================
³                              Summary of Above Cascade ==> ³14380,E-02³000010³000010³000000³000010³
```

Figure 4.3: Example output of the `COLLISION.txt` file for 75 keV He^+ irradiation in $YBa_2Cu_3O_7$ of 210 nm width. Recoils are numbered consecutively within each collision cascade. The atomic number, kinetic energy after collision and the initial coordinates are listed for each recoil.

Each ion could knock out several primary recoil atoms along its path through the target. Thus, several collision cascades presented in figure 4.3 could be listed for a given ion. However, for the ion considered, the displacement statistics of all occurring collision cascades are listed below its last collision cascade (fig. 4.4). Furthermore, the displacement statistics include the statistics for all ions considered up to this point.

```
=========================================================================================================
- For Ion 0000001:              For All Ions to date :                                                  º
- Displacements     = 000105,0  Average Displacements/Ion     = 0000105,000                             º
- Replacements      = 000004,0  Average Replacements/Ion      = 0000004,000                             º
- Vacancies         = 000101,0  Average Vacancies/Ion         = 0000101,000                             º
- Interstitials     = 000105,0  Average Interstitials/Ion     = 0000105,000                             º
- Sputtered Atoms   = 000000,0  Average Sputter Atoms/Ion     = 0000000,000                             º
- Transmitted Atoms = 000001,0  Average Transmitted Atoms/Ion = 0000001,000                             º
=========================================================================================================
```

Figure 4.4: Example output of the displacement statistics of a given ion and for all ions to date from `COLLISION.txt` file.

4.3 Programs for Data Processing

In this section the programs used to calculate the fluence, defect density, dpa, and T_c for He^+ irradiation with 75 keV and 30 keV in $YBa_2Cu_3O_7$ of 210 nm thickness are presented. The main purpose is to explain how certain values are calculated from SRIM output and to give an overview to allow for easier reuse of the programs within the research group. The programs discussed below can be found in the group share and are partly published in section C of the appendix.

The SRIM simulation calculates defect coordinates with respect to the incident beam coordinate center, as shown in figure 5.1. To obtain fluences and defect densities corresponding to the experimental irradiation conditions, the coordinates of the ion trajectory and its corresponding collision cascades need to be shifted. For 75 keV irradiation a uniform distribution across the mask hole is assumed, whereas the irradiation with 30 keV is assumed to be performed with a defocused ion beam of a He^+ microscope with radial Gaussian distribution of fluence. The approximation of Gaussian beam distribution for defocused He^+ microscope beams was found to be consistent with fluence dependence of growth behavior of nanopores in SiN membranes by Emmrich et al. [95].

4.3.1 `fluence.c`

The program `fluence.c` requires input of simulated `TRANSMIT.txt` files. Since a `TRANSMIT.txt` file can only be calculated for a given width, several runs of different width need to be calculated using SRIM. The filename should be changed to `TRANSMIT_`*`width`*`_A.txt`, where *`width`* is to be inserted in Å. Since SRIM tends to cut the last row in the output file, one needs to make sure that the file has a proper `End Of File (EOF)` condition.

Before execution, the calculated width values need to be inserted into the `depth[]` array. Since the program is not written for shell input, the array length and loop conditions need to be changed according to the number of files used.

`filecopy`

After reading in each `TRANSMIT_`*`width`*`_A.txt` file, a copy of the file is made (function `filecopy`), where commas and the sign ^{3} are substituted by points and spaces, respectively. The latter is a problem of font-type, however, the SRIM manual expects the use of `Newline` font. This conversion is necessary, since the data file with altered symbols is used for further calculation.

The replaced file is searched for the string `(Z)`, which is the last line before the actual data (fig. 4.2). Next, one line is read in and stored in the `input[]` array.

`randnum`

The y and z coordinates are independently and randomly displaced in a uniform distribution inside an area of $d = (180 \pm 5)$ nm in diameter by calling the function `randnum`. An accept/reject algorithm is used to randomly distribute the coordinates. First, the sign of the shift is determined by drawing a random number

between 0 and 1000 independently for each coordinate. If the number is below 500, the shift changes sign. Next, the absolute value of the shift y_+ and z_+ is determined by drawing an integer random number between 0 and 900. If the radius $r = \sqrt{y_+^2 + z_+^2} < 900$ the absolute values and signs of the shift for both coordinates are accepted. Else, the procedure is repeated until the shifts obey this constraint.

The SRIM calculation of `TRANSMIT.txt` files for different widths uses the same random number seed. Hence, the ion coordinates stated in the files of different width are correlated. The random seed in this program is reset as well. However, since some ions are implanted, the correlation is lost. An updated program should improve the correlation by additionally calling random numbers for implanted ions, such that the subsequent random number calls match the ion number again.

The essential part of this program is the mapping of ion coordinates to 2 nm × 2 nm areas and counting the number of ions within this cell for several slices in target depth. The unit cell size of the irradiation pattern for sample A is about 302 nm, such that an array of dimension `ioncount[:][151][151]` is created. It has to be noted that, in principle, the coordinate shift should be distributed uniformly using real numbers. However, the ion coordinates are assigned to areas of smaller resolution, such that the use of integer random numbers is feasible.

`foldback`

It might occur that either the ion trajectory or their shifted coordinates are located outside the unit cell size of mask hole. In this case, the neighboring unit cell is irradiated. However, this irradiation needs to be mapped back into the primary unit cell, since irradiation is performed in a periodic array and the ion trajectory might origin from irradiation of the neighboring unit cell. The mapping back is performed using the `foldback` function.

After obtaining the number of ions per 4 nm^2 area for a target width, this number is normalized to units of 10^{15} cm^{-2} and stored in a separate file with the appropriate format for visualization using `gnuplot pm3d` style.

4.3.2 3D_defect_distribution.c

This main program reads out the defect coordinates from the `COLLISION.txt` file, shifts them randomly according to a uniform distribution and counts the number of defects per 8 nm^3 as well as the atom's atomic number.

First, the program is initialized with some requests to the user. The number of ions `n` which should be considered from the `COLLISION.txt` file must be given. It must not be greater than the actual number simulated, but can be smaller than that. Next, the user is asked whether commas should be replaced by points. Since the `COLLISION.txt` file is of size of about 10-20 GB for several 100.000 ions with about 100 displacements per ion at the setup considered, this should only be done once. Next, an estimate on how many lines of data per ion there are in the file. This is necessary to alter the defined variable `LENGTH` in case it is smaller than the

estimated number of lines, since it defines the number of maximum array entries which are possibly read in for each ion's collision cascades.

readcol

The function `readcol` reads in all displacement coordinates and their respective atomic number from recoil cascades caused by one ion. The function reads in subsequent lines of the file and first searches for the line before the beginning of a recoil cascade for ion `k` (fig. 4.3).

```
snprintf(find_ion,8, " %05d=", k);
```

Once this line is found, the function searches for the entries within the recoil cascade.

```
snprintf(find_cascades,8, "Û %05d", l);
```

The line of data is stored to the array `koord[:][8]`, where entries `koord[:][3-5]` correspond to the x, y and z coordinates, respectively. The loop ends if the string `"For All Ions to date"` is found.

Once all coordinates of defects for one ion are read in, the main program calls the `randnum` function to shift this ions coordinate and thus, the coordinates of all its defects from collision cascades. Coordinates outside the unit cell of the mask hole are mapped back calling the `foldback` function. The number of defects within cubes of (2 nm)$\cdot[i, i+1)$ length is stored in the `defects[o][p][q][ind]` array, with `ind` $\in [1, 5]$ denoting classification for Y, Ba, Cu, O and total defects, respectively. This array with the 3D defect distribution data is stored in the `defectmatrix_x_y_z_fxyz.txt` file.

It has to be noted that this program should be improved by reducing the number of global variables. Furthermore, the process of reading-in should be possible without the use of the input array of predefined `LENGTH`, by subsequently reading in and storing data with the same random shift.

4.3.3 dpa_mean.c

This program reads in defect matrices obtained by `3D_defect_distribution.c` for several simulated fluences (i.e. number of ions, see table 4.1) and computes the mean number of defects per atom (dpa) inside the defect channel from start to end value (depth).

$$\mathrm{dpa} = \frac{N_{\text{sum of defects in arrays}}}{8\ \mathrm{nm}^3 \cdot N_{\text{array entries}}} \cdot \left(\frac{13_{\text{atoms per u.c.}}}{172.8093\ \text{Å}^3} \right)^{-1} \tag{4.2}$$

The mean dpa is calculated for several start and end values. The computed dpa's are linearly proportional to the fluence (fig. 4.5). This is to be expected, since each ion creates a mean number of defects. The mean dpa values substitute the fluences as x values in the experimentally determined $T_{c\text{-onset}}$ figure 4.9.

4.3.4 dpa_distribution.c

This program reads in the `defectmatrix_x_y_z_fxyz.txt` files for the total number of displacements and for each atom species. The mean number of defects per atom within a cylinder of 180 nm diameter is calculated for every 2 nm target depth. The resulting dpa distribution with respect to depth is presented in figure 5.6.

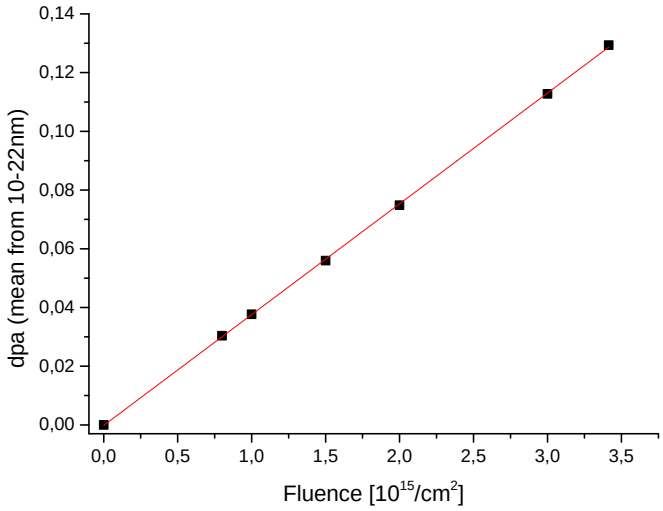

Figure 4.5: dpa and fluence are linearly dependent. This is to be expected since each ion creates a mean number of defects.

4.3.5 `dpa_histogram.c`

This program reads in the file `defectmatrix_x_y_z_fxyz.txt` containing the total 3D defect distribution and checks each cell of 8 nm^3 for its number of defects. Their abundance is stored in an array, which is then normalized to values of dpa. This process is repeated with the addition of taking the average number of defects within six nearest neighboring cells iteratively up to five times. Hence, small clusters of high defect density are smeared out in the histogram (fig. 5.7).

4.3.6 `Tc_matrix.c`

This program reads in the file `defectmatrix_x_y_z_fxyz.txt` containing the total 3D defect distribution, calculates the dpa for each cell of 8 nm^3 and determines its corresponding $T_{c\text{-onset}}$ value according to equation 4.5 using parameters given in table 4.3.

4.3.7 `-HIM.c`

The simulation of 30 keV He^+ irradiation accounts for a sample geometry recently irradiated with a defocused ion beam of an He^+ ion microscope (HIM) within our research group. For 30 keV He^+ irradiation, the programs are named with the extension `-HIM.c`. The programs are essentially the same, apart from a quadratic unit cell of 200 nm width and a Gaussian distribution for the ion-beam fluence and hence, all respective collision cascades. The Gaussian beam profile is an approximation to the actual defocused beam profile.

The Gaussian distribution of random numbers is obtained by an accept/reject algorithm in the altered `randnum` function. The random distribution of the shifted incident coordinates y_+ and z_+ is accepted, if a randomly drawn number r of uniform distribution obeys

$$r < e^{-\frac{-(y_+^2+z_+^2)}{2\sigma^2}}$$

This constraint will be accepted with probability of Gaussian distribution. With $\sigma = \mathrm{FWHM}/2.4$, the FWHM must be given to determine the beam profile. The overall number of ions is 50639, corresponding to fluence of 3×10^{15} cm^{-2} if the FWHM is about 27 nm. The mean dpa distribution with respect to depth is determined as the mean dpa value within a cylinder of 27 nm diameter. Since the $T_{c\text{-onset}}(\mathrm{dpa})$ is calibrated using experimental data it is applied to the simulation of 30 keV He^+ irradiation as well.

4.4 Mapping dpa to $T_{c\text{-onset}}$

The goal of the computational part of this thesis is to obtain a 3D T_c profile for the samples irradiated by 75 keV He^+ ions through a stencil mask of $d = (180 \pm 5)$ nm used in the experimental part of this thesis, by calculating the T_c corresponding to the dpa obtained by simulation.

4.4.1 Pair-Breaking Function of T_c Reduction

Lesueur et al. [96] and Tolpygo et al. [73] reported that the reduction in T_c with respect to defect density is qualitatively consistent with pair-breaking theory. Hence, a fit of the pair-breaking theory function for experimentally obtained discrete T_c values at given fluence can provide a function for continuously mapping defect density obtained by simulation to T_c. The aforementioned publications propose to use the pair-breaking function (eq. 4.3) theoretically derived by Abrikosov and Gorkov [97] as a fitting function for normalized $T_{c\text{-onset}}/T_0$, where $T_0 = 90$ K is the critical temperature of the non irradiated superconducting film.

$$\ln\left(\frac{T_{c\text{-onset}}}{T_0}\right) = \Psi\left(\frac{1}{2}\right) - \Psi\left(\frac{1}{2} + 0.14\frac{T_0}{T_{c\text{-onset}}}\frac{\Gamma}{\Gamma_c}\right) \tag{4.3}$$

The pair-breaking rate Γ is proportional to the inverse pair-breaking scattering time τ_{pb}^{-1}, which itself is proportional to the defect density. Since this nonlinear, implicit function is tricky to fit, first, the digamma function $\Psi(\zeta)$ is approximated by the asymptotic formula (eq. 4.4) given in [98].

$$\Psi(\zeta) \approx \ln(\zeta) - \frac{1}{2\zeta} - \frac{1}{12\zeta^2} + \mathcal{O}(\zeta^{-4}) \tag{4.4}$$

According to equation 4.3 $\zeta = \frac{1}{2} + 0.14\frac{x}{y}$. For

$$\lim_{y\to 1} \Psi(\zeta) = \text{const},$$

thus the implicit y-dependence of the right hand side can be neglected. However, for

$$\lim_{y\to 0} \Psi(\zeta) = \lim_{\zeta\to\infty} \ln(\zeta)$$

the function diverges, such that we introduce an error for small y using this approximation.

The function can be linearized in y by approximating $\ln(y) \approx y - 1$ for $y \in [0, 2]$. However, an exponentially increasing error for $y \to 0$ is introduced. This is acceptable, since an error up to $0.2 \cdot T_0$ has low impact on the T_c profile plot.

The errors arising by approximations and the mitigation of the implicit dependence can be compensated for by introducing additional fit parameters: d as a constant offset, k as an amplitude of Ψ and g as the pair-breaking parameter Γ/Γ_c per dpa. Using $\Psi\left(\frac{1}{2}\right) \approx -1.9635$ [98] and $z(\text{dpa}) = 0.5 + 0.14 \cdot g \cdot \text{dpa}$ the fitting function is:

$$\frac{T_{c\text{-onset}}}{T_0}(\text{dpa}) \approx -1.9635 + d - k \cdot \left[ln(z) - \frac{1}{2(z)} - \frac{1}{12(z)^2}\right] \tag{4.5}$$

This approximated fitting-function is in good agreement with the digitized fitting function of Lesueur et al. [96] and shows only minor deviations for $T_c \to 0$ (fig. 4.6).

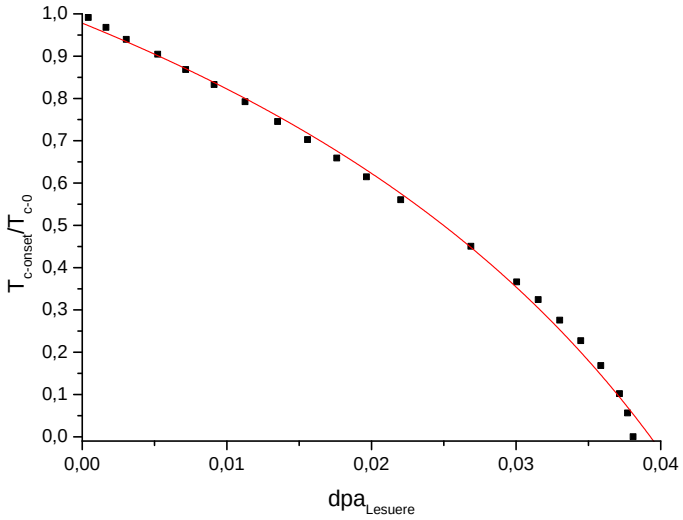

Figure 4.6: The approximated fitting function (eq. 4.5) is tested on digitized data of the unapproximated fitting function published by Lesueur et al. [96].

4.4.2 Determining $T_{c\text{-onset}}$ from Resistivity Data

The pair-breaking fitting function (eq. 4.5) will be used to fit simulated dpa data to corresponding experimental T_c values, such that continuous T_c values can be calculated from 3D damage profiles to obtain 3D T_c profiles. Thus, the $T_{c\text{-onset}}$ of experimental in-plane $\rho(T)$ data for several fluences given by Lang et al. [81] (fig. 4.7) needs to be determined.

$T_{c\text{-onset}}$ is defined as the intersection of normal-state resistivity with the tangent on the inflection point of the cumulative Gaussian distribution function of the superconducting transition. It is thus an indicator for the temperature at which the material is on the edge of the superconducting state. However, since the $\rho(T)$ is obtained by digitizing semi-logarithmic data (fig. 4.7), the fitting of the cumulative Gaussian distribution function is not feasible. Therefore the tangent to the distribution is approximated by a linear fit at the center of the superconducting transition. Thus, $T_{c\text{-onset}}$ is the intercept of both linear functions $\rho = k \cdot T + d$.

$$T_{c\text{-onset}} = \frac{d_2 - d_1}{k_1 - k_2} \tag{4.6}$$

However, at a fluence of 3×10^{15} cm^{-2} a semiconducting feature in resistance is measured. Thus a straightforward application of the general definition is not possible. An approximation of the intrinsic semiconductor carrier density n_i for $T \gg 0$ is given in equation 4.7.

$$n_i \propto T^{\frac{3}{2}} \cdot e^{-\frac{E_g}{2k_B T}} \approx T^{\frac{3}{2}} \tag{4.7}$$

The fitting function (eq. 4.8) thus superposes the normal and semiconducting state resistance, with $\rho \propto \sigma^{-1} \propto n_i^{-1}$.

$$\rho_{xx}(3 \times 10^{15}\ \text{cm}^{-2}) = (A \cdot |T - T'|^{-1.5} + y_0) + (R \cdot T + d) \tag{4.8}$$

The non-physical parameter T' shifts the x axis offset, allowing for compensation of the simplifications made in the assumption of $T \gg 0$ and neglecting the semiconducting energy gap $E_g \sim 0.23$ eV [99].

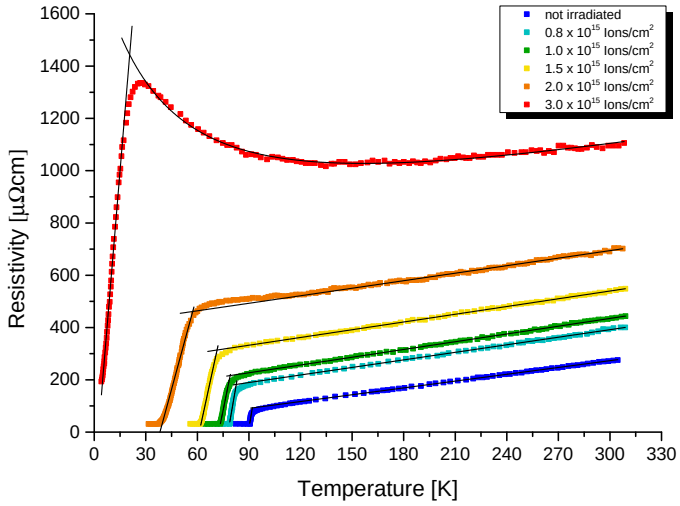

Figure 4.7: Data digitized manually from experimental $\rho(T)$ data in semi-logarithmic scale (fig. 2.7a) for several irradiation fluences. $T_{c\text{-onset}}$ is evaluated as the intersection of the linear fits, apart from the fluence 3×10^{15} cm^{-2} due to its semiconducting features.

The intersection points are calculated according to equation 4.6 and given in table 4.2, apart from the fluence 3×10^{15} cm^{-2}, which was calculated using *WolframAlpha* [100] (fig. B.1). Uncertainties are not given, since error propagation from the fitting functions' standard deviations in this case is only a measure of how well the data was digitized and is estimated to be below 0.5 K.

Table 4.2: Calculated $T_{c\text{-onset}}$ for several fluences.

$10^{15}\,\frac{\text{Ions}}{\text{cm}^2}$	$T_{c\text{-onset}}$
0	92.0
0.8	82.6
1.0	79.1
1.5	71.4
2	57.3
3	20.6

4.4.3 Calibration of $T_{c\text{-onset}}$

The fluence for which T_c becomes zero needs to be determined to further compensate the uncertainty in fitting T_c(dpa) for high defect densities. Therefore, T_c dependence on 190 keV He^+ irradiation fluence at 150 K published by Nédellec et al. [101] is digitized. This data includes the data point $T_c = 0$ at a fluence of $1.9 \times 10^{15}\text{cm}^{-2}$. Unfortunately, it is not stated whether this is the minimal fluence for complete T_c suppression. The data is fitted using equation 4.5 as depicted in figure 4.8a to determine the fluences for 190 keV He^+ irradiation at 150 K corresponding to the same T_c values for irradiation with 75 keV at 300 K given in table 4.2. Hence, the fluences can be correlated via their common $T_{c\text{-onset}}$ presented in figure 4.8b and are found to be of linear dependence. This is reasonable, since each incident ion creates a mean number of defects at given kinetic energy and irradiation temperature.

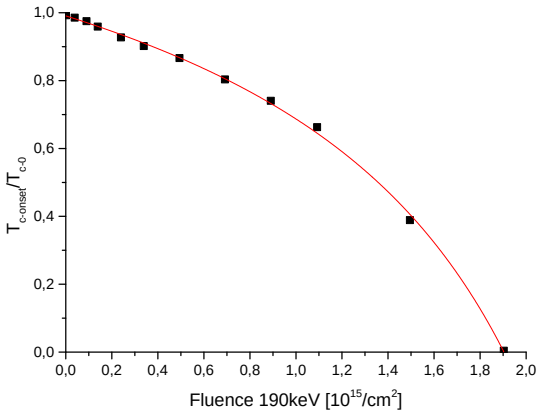

a) $T_c(\Phi)$ for 190 keV He^+ irradiation at 150 K fitted using equation 4.5.

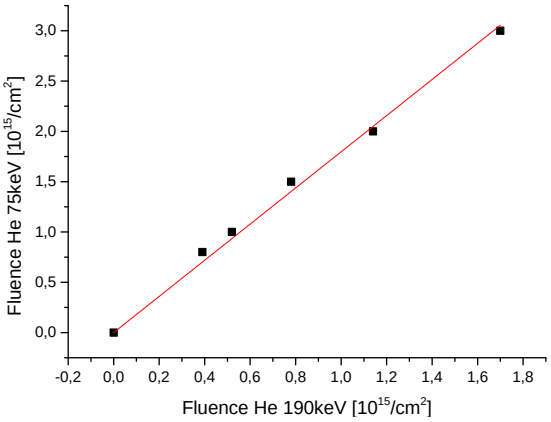

b) Correlation of fluences for 150 K 190 keV and 300K 75 keV He^+ irradiation.

Figure 4.8: Temperature dependence on fluence for 190 keV He^+ irradiation at 150 K from Nédellec et al. [101]. Linear correlation of 190 keV He^+ irradiation at 150 K and 75 keV He^+ irradiation at 300 K fluences at same $T_{c\text{-onset}}$ is found.

The extrapolation of the linear fit for a fluence of 1.9×10^{15} cm^{-2} for 190 keV He^+ irradiation at 150 K corresponds to a fluence of about 3.4×10^{15} cm^{-2} for 75 keV He^+ irradiation at 300 K. This fluence corresponds to about 868,906 ions per mask hole, as stated in table 4.1.

The in-plane resistivity data published by Lang et al. [81] (fig. 4.7) was measured on homogeneously irradiated bridges of 80 nm thickness. However, the fluence and defect density are not distributed homogeneously with respect to target depth, since ions are scattered due to collisions or get stuck as interstitials. Thus, the volume considered in calculating the mean dpa is crucial to the calibration and a reasonable criterion defining the mean dpa corresponding to the experimentally determined $T_{c\text{-onset}}$ needs to be found.

First, the mean dpa can only be determined inside the cylindrical dimensions of the mask hole, since the bridges were irradiated homogeneously. Second, for low current densities, the resistivity is determined by continuous regions of highest T_c. Following the SRIM simulation, the defect density for 75 keV He^+ irradiation is

lowest in the topmost layer of the thin film, since collision cascades could not yet accumulate defects, even though the fluence is highest.

However, surface layers could be of different composition or structure and thus underdoped [102]. Hence, in this calibration the mean dpa is defined as the mean number of defects per atom in a cylindrical slice of mask hole diameter from 10 nm to 22 nm depth, which corresponds to a thickness of about 10 unit cells. This calibration is presented in figure 4.9 together with some alternative definitions of mean dpa.

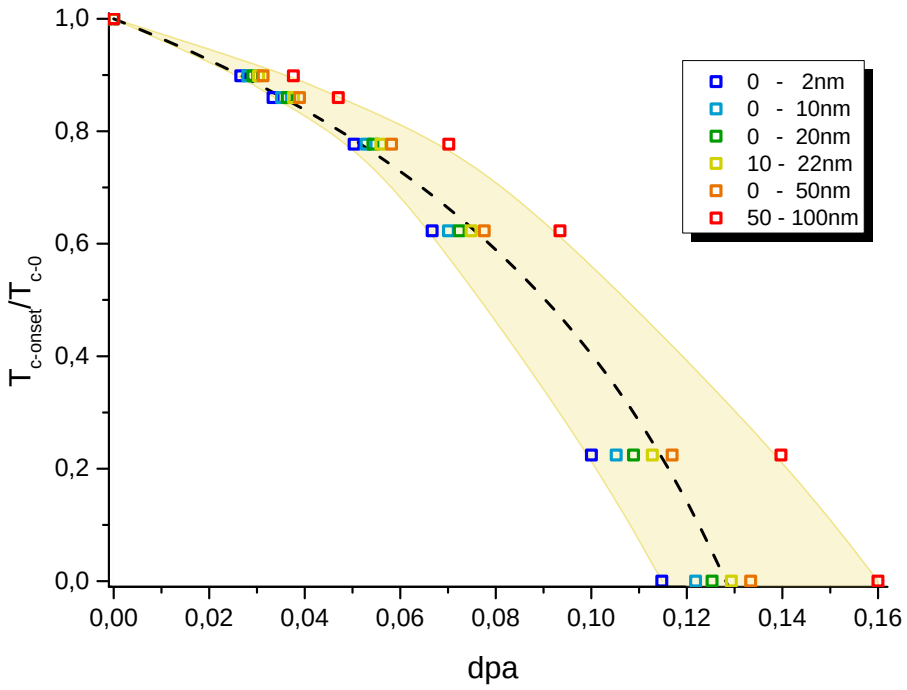

Figure 4.9: Experimentally determined $T_{c\text{-onset}}$ values are fitted to simulated dpa defined as the mean dpa in a cylindrical slice of mask hole diameter and depth as stated in the figure legend. The dashed curve is the fit of equation 4.5 to mean dpa from 10 nm to 22 nm depth. The yellow region is a qualitative confidence interval for the T_c calibration.

The dashed fit in figure 4.9 yields the fit parameters given in table 4.3 for $T_0 = 91.95604$ and a linear constraint of going through the point (0,1). The obtained fit parameters calibrated by experimental data are inserted into equation 4.5 and used to calculate the transition temperature for simulated 3D T_c profiles from 3D damage profiles.

Table 4.3: Fit parameters obtained by fitting equation 4.5 to data in figure 4.9 (dashed curve) and used for calculation of T_c profiles.

d	3.55452
k	- 0.29165
g	- 15.51013

5 Fluence, Damage and T_c Profiles

5.1 Simulation of Ion Irradiation

Figures 5.1 and 5.2 represent a lateral view on the as simulated incidence of 100 He^+ ions into $YBa_2Cu_3O_{7-\delta}$ of 210 nm thickness with energy of 75 keV and 30 keV.

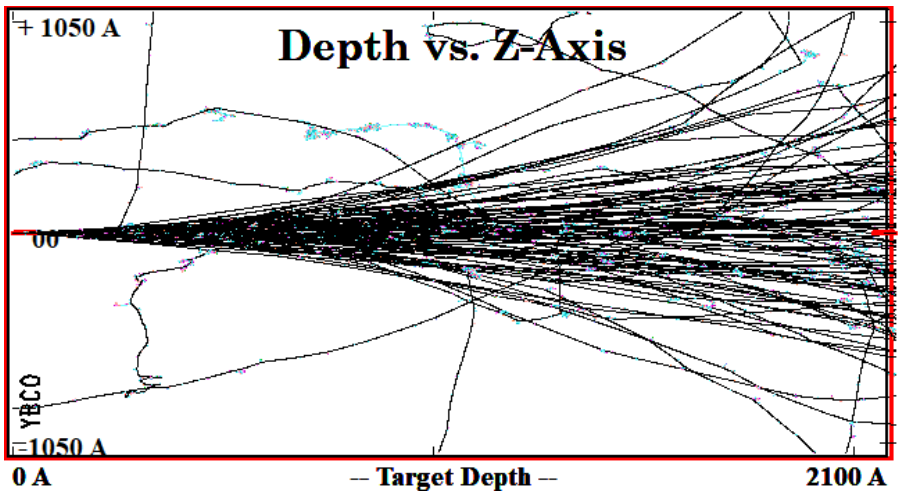

Figure 5.1: Lateral view on 100 simulated ion trajectories of 75 keV He^+ irradiation creating about 94 vacancies per ion at a transmittance of T= 91%.

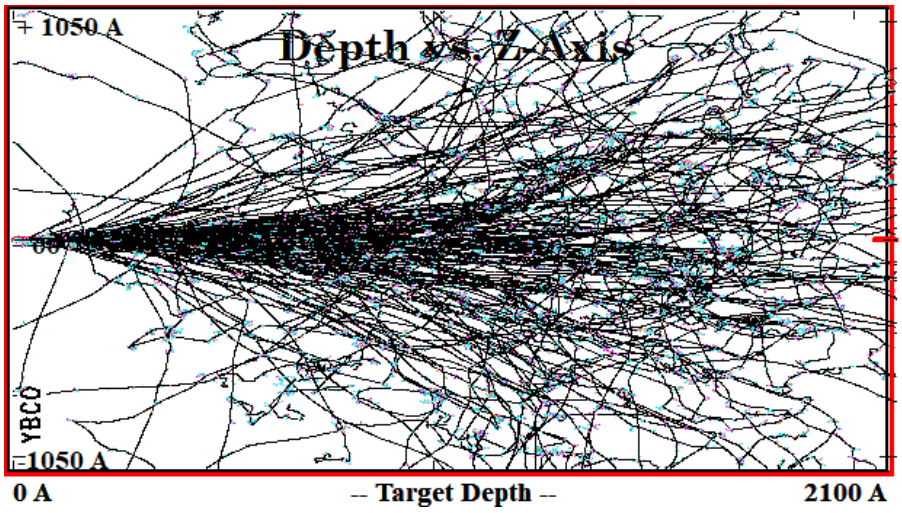

Figure 5.2: Lateral view on 100 simulated ion trajectories of 30 keV He^+ irradiation creating about 208 vacancies per ion at a transmittance of T= 20%.

The figures qualitatively confirm that incident ions of lower energy experience much more interaction with the target ions due to the increasing nuclear stopping cross-section. Furthermore, the mean number of created vacancies per ion is roughly twice as high for 30 keV irradiation at 80% ion implantation.

5.2 Fluence Profiles

The trajectories of the incident ions from figures 5.1 and 5.2 are distributed to a uniform distribution within the area of the mask hole of 180 nm in diameter for 75 keV irradiation (fig. 5.3a), whereas the ions of the 30 keV irradiation are distributed according to a Gaussian distribution of FWHM = 27 nm (fig. 5.3b).

The resulting fluence profiles are consistent with the calculated transmittance. There is straggling of about 30 nm in radius for 75 keV irradiation at 200 nm depth with accompanied smearing of the ion fluence. However, the irradiation of a columnar defect is clearly achievable.

For 30 keV irradiation the fluence is already strongly decreased at about 100 nm depth due to much higher amount of ion implantation. Furthermore, the Gaussian beam profile spreads out much faster than for 75 keV irradiation due to the increased nuclear stopping cross-section.

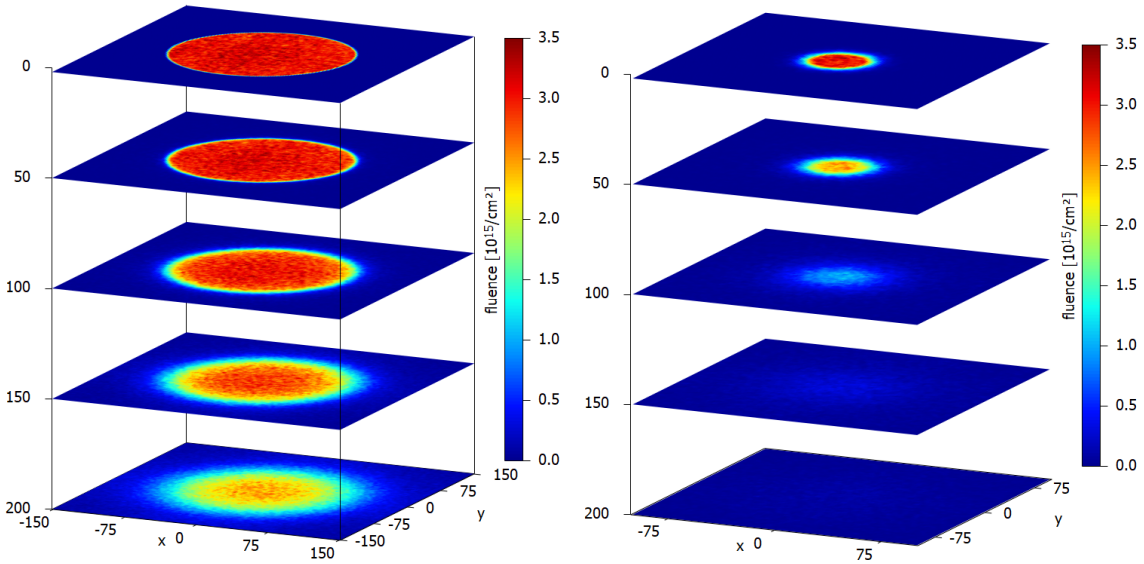

a) Fluence profile for 75 keV uniform distribution.

b) Fluence profile for 30 keV Gaussian distribution with FWHM = 27 nm.

Figure 5.3: Fluence profiles for 3×10^{15} cm^{-2} He$^+$ irradiation at different energies and distributions.

5.3 Damage Profiles and dpa

The number of defects per atom is calculated as the average dpa within cubes of 8 nm^3. Here, the term defect denotes Frenkel pairs, or more precisely vacancies, since there might be less interstitials than vacancies in case recoiling atoms leave the target. It should be noted that SRIM does not account for interstitials. However, Lang et al. found in simulations that atoms are mostly displaced within distances at the order of the size of a unit cell [76]. Furthermore, it should be brought to mind that thermal annealing effects are not taken into account in the SRIM simulation. Thus, the actual defect density is most probably lower.

As implied by the fluence profiles and transmittance, irradiation with 75 keV He^+ ions creates consistent columnar defects with shape of the stencil mask profile (fig. 5.4a). The straggling in dpa at 200 nm is slightly decreased with respect to the fluence plot, since the fluence of straggled ion trajectories beyond the initially irradiated area of 180 nm in diameter is about a third of the incident irradiation fluence. However, recoil cascades give rise to defect clusters and reduce the sharpness of defect density with respect to the columnar defect.

Irradiation with 30 keV He^+ ions creates an inhomogeneous defect distribution with respect to depth and shows high straggling of recoil cascades below 80 nm depth (fig. 5.4b). Both irradiations yield homogeneous radial defect distributions, which is expected, since the simulation is performed assuming amorphous target material and uses statistical algorithms for cascade calculation.

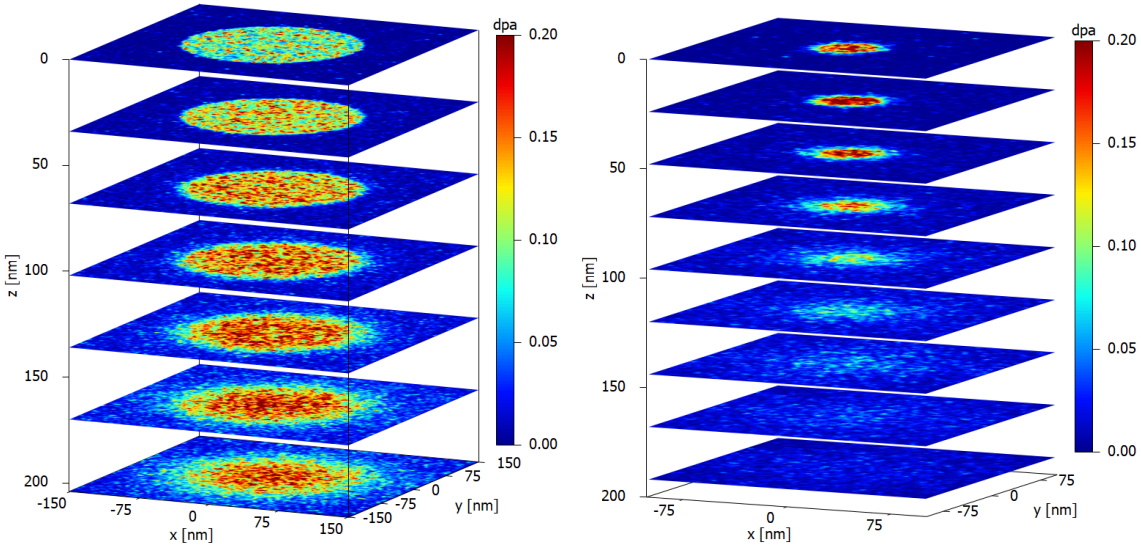

a) dpa profile for 75 keV uniform distribution.

b) dpa profile for 30 keV Gaussian distribution with FWHM = 27 nm.

Figure 5.4: dpa profiles for 3×10^{15} cm^{-2} He^+ irradiation at different energies and distributions.

Cross-section profiles of defects per atom are presented in figure 5.5. For 75 keV irradiation the shape of the columnar defect is very sharp up to a depth of 100 nm, whereas the density of defect clusters outside the columnar defect increases with

depth. However, the straggling of dpa is about 10 nm at 200 nm depth. Surprisingly, the defect density of the topmost layers is lowest throughout the area of irradiation.

For 30 keV irradiation the dpa cross-sectional profile is columnar up to 80 nm depth where it abruptly merges in a large plume of lower defect density. The Gaussian beam shape can not be deduced from the lateral cross-sectional view, however, it is clearly visible when comparing the profiles of figure 5.4. Below 170 nm depth no significant defect density is created.

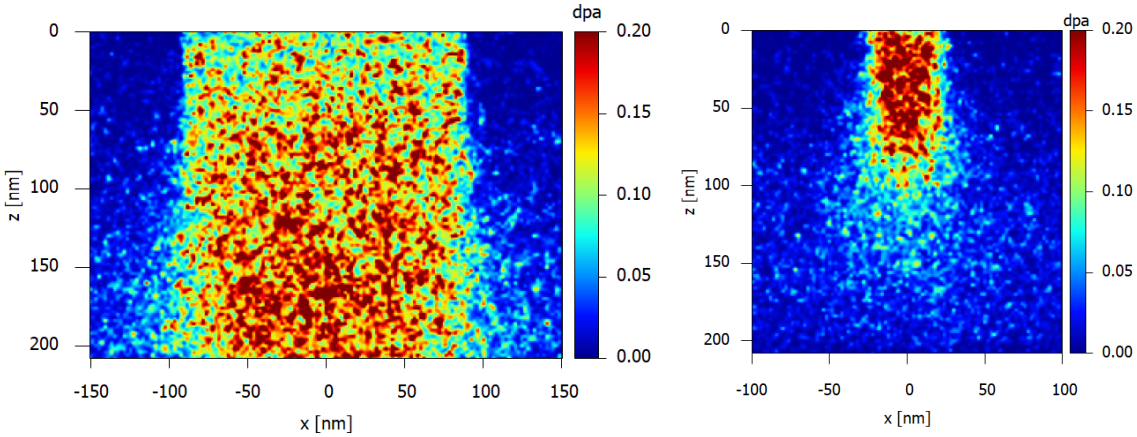

a) dpa cross-section for 75 keV uniform distribution.

b) dpa cross-section for 30 keV Gaussian distribution, FWHM = 27 nm.

Figure 5.5: dpa cross-section for 3×10^{15} cm^{-2} He^+ irradiation at different energies and distributions.

The increase of defect density with depth for 75 keV irradiation is supported by figure 5.6. However, irradiation with 30 keV He^+ ions shows a rapid increase in defect creation, which drastically decreases beyond 80 nm depth.

There are several mechanisms contributing to the distribution of dpa with respect to depth. On the one hand, dpa increases due to accumulation of recoil cascades. Assuming that a collision cascade created by a primary recoil atom creates a plume of mean defect distribution around its primary recoil site, a constant defect density should occur once these distributions start to overlap with respect to depth, provided the fluence has not substantially decreased. Hence, uniformly distributed primary recoils should first give rise to a monotonic increase in dpa, transitioning into a constant dpa distribution with respect to depth only after passing a preceding layer of target material. This mechanism is consistent with the data presented in figure 5.6 for 75 keV irradiation (solid lines).

On the other hand, the dpa increases with depth due to increasing nuclear stopping cross-section of ions losing energy due to target ionization (electronic stopping). This implies a steady increase in dpa with respect to depth up to a point of inflection at which dpa is reduced dramatically due to decreasing fluence. This explanation is consistent with data presented in figure 5.6 for 30 keV irradiation (dashed lines). The kinetic energy of 30 keV ions is dissipated sooner than for irradiation with 75 keV ions due to their higher nuclear stopping cross-section. Hence, the ion fluence for 30 keV irradiation decreases with depth.

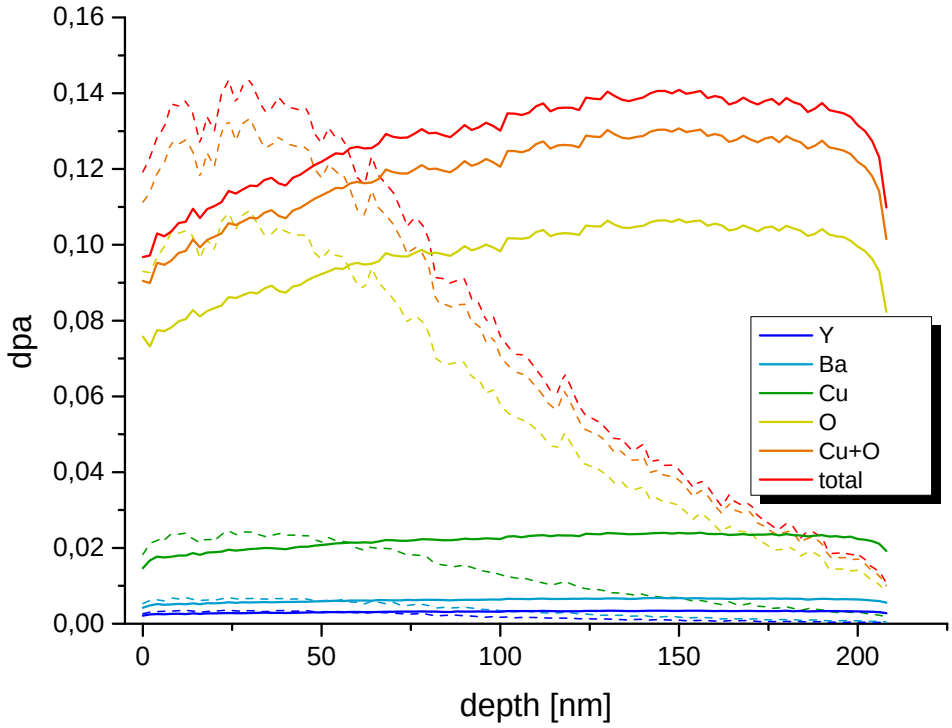

Figure 5.6: Distribution of dpa with respect to depth for 75 keV (solid lines) and 30 keV (dashed lines) of individual elements. Here, dpa is a mean dpa within defect columns of 180 nm and 27 nm diameter, respectively.

The dpa distribution for each element is presented in figure 5.6. First, the individual distributions are directly proportional to each other, which was to be expected due to the statistical approach of the simulation. Second, about 90% of vacancies produced are located at Cu and O sites. This seems to be a high share since their displacement energies are rather low. However, one has to keep in mind that their stochastic abundance in the material is already about 85%. Hence, the presumption of $E_d^{\text{O-c}}$ being 1 eV instead of 1.5 eV is of insignificant influence.

For further insight in defect formation, the atomic number and energy distributions of the primary recoil atoms could be investigated to understand whether oxygen vacancies are created by recoil cascades of the heavier elements Y and Ba, or by ion collisions directly.

Unfortunately, vacancies in chain and plane oxygen sites can not be distinguished in the `COLLISION.txt` file, although separate displacement energies are set for two oxygen entries in the layer setup. Nonetheless, the simulation is consistent with the findings of Lang et al. [76] that light-ion irradiation at low energies primarily creates Cu and O defects, as intended for T_c suppression.

The abrupt decline in dpa at the bottom of the sample should not be an artifact of programming, since the number of defects within [208, 210) nm is summed. Hence, this could be an indication that a significant amount of recoils occurs in the opposite direction of the incident ion beam. However, the actual sample is grown on a substrate, which would reduce this effect.

The histogram in figure 5.7 presents the relative abundance of dpa corresponding to the mean dpa of 8 nm^3 cells within the unit cell of the irradiation geometry of sample A. More than half of the 8 nm^3 cells within the unit cell contain little or no defects at all. Averages between the six nearest neighboring cells are taken to investigate the correlation of defect density. The small amounts of very high defect density are averaged out, hence, there are no clumps of high defect density, but rather individual clusters of high defect density within an area of average density. This again is a strong indication for clusters of point defects created at the end of collision cascades.

Furthermore, in taking the average five times, a peak around 0.13 dpa is formed, which corresponds to the mean dpa within the columnar defect channel. This peak emerges as an intersection in the cumulative distributions when taking averages. The cumulative distribution shows that about 10% of the 8 nm^3 cells contain a mean defect density which completely suppresses T_c (fig. 4.9). The histogram could be further improved by reducing the cell size to increase resolution.

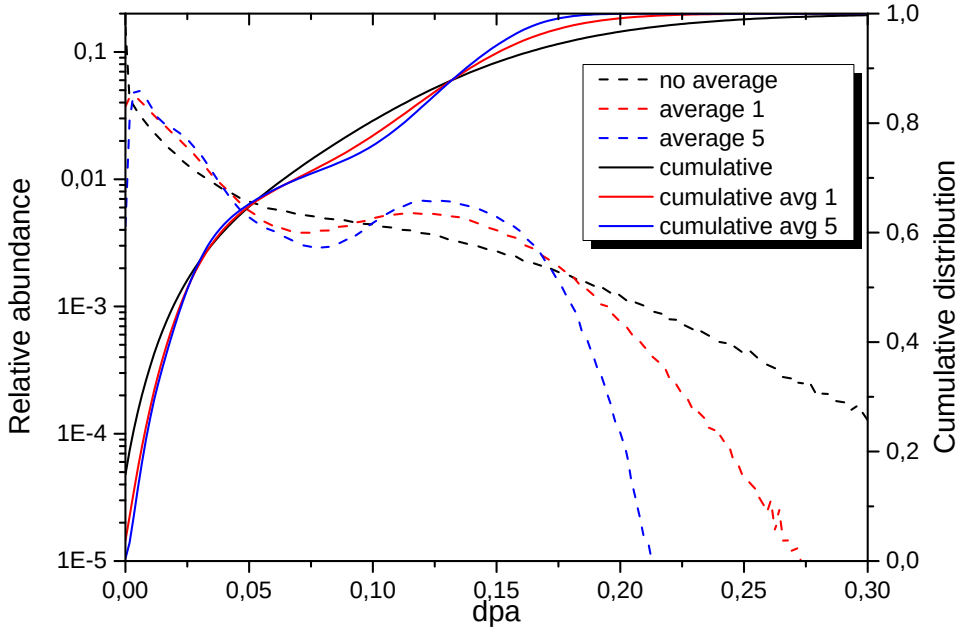

Figure 5.7: A histogram of relative abundance of mean dpa in cells of 8 nm^3 within the unit cell of the irradiation geometry of sample A for 75 keV irradiation is given in dashed lines. Solid lines represent the corresponding cumulative distribution. The average dpa within the six nearest neighboring cells is taken once and five times.

5.4 T_c Profiles

$T_{c\text{-onset}}$ is calculated from simulated dpa using eq. 4.5. The overestimation of simulated dpa does not directly affect the calculation since it is calibrated using experimental $T_{c\text{-onset}}$ data. Figures 5.8 and 5.9 essentially show the same features as observed for dpa profiles, though now it can be concluded that T_c is continuously suppressed within the columnar defect. However, the suppression is not distributed homogeneously, since the average suppression increases with depth.

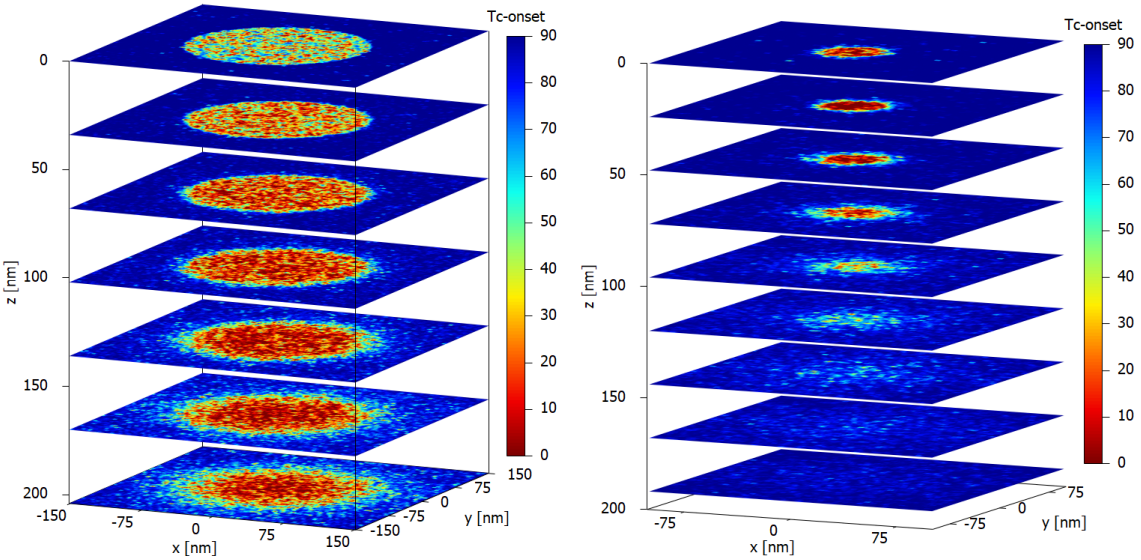

a) $T_{c\text{-onset}}$ profile for 75 keV uniform distribution.

b) $T_{c\text{-onset}}$ profile for 30 keV Gaussian distribution with FWHM = 27 nm.

Figure 5.8: $T_{c\text{-onset}}$ profile for 3×10^{15} cm^{-2} He^{+} irradiation at different energies and distributions.

For 30 keV irradiation, the target material is still superconducting below 150 nm depth since the irradiation does not create the required amount of defects for significant T_c suppression.

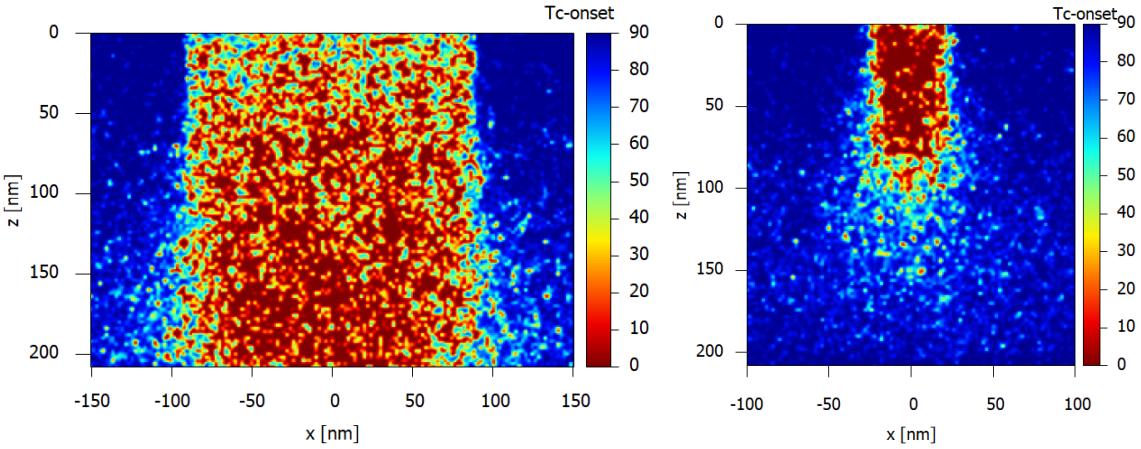

a) $T_{c\text{-onset}}$ profile cross-section for 75 keV uniform distribution.

b) $T_{c\text{-onset}}$ profile cross-section for 30 keV Gaussian distribution with FWHM = 27 nm.

Figure 5.9: $T_{c\text{-onset}}$ profile cross-sections for 3×10^{15} cm^{-2} He^{+} irradiation at different energies and distributions.

It can be concluded that masked He^{+} irradiation of 75 keV creates consistent columnar defect channels of strong T_c suppression at 10 nm resolution at 200 nm thickness. Columnar defects of T_c suppression can also be created using 30 keV irradiation. However, the sample thickness should not exceed 80 nm if consistency is required.

6 Sample Fabrication

6.1 Thin Film Synthesis and Processing

The samples examined in this thesis were produced at the Institute of Applied Physics, Johannes Kepler University Linz, in the group of Prof. J. Pedarnig. The fabrication of the samples was carried out by M.-A. Bodea and M. Dosmailov, who documented the processing in their theses [103, 104].

YBCO thin films are grown on two substrates, each of which is patterned to two areas on which four-point measurements can be performed. One area of each sample is patterned with a quadratic columnar defect array (CDA) with mask hole diameters of (180 ± 5) nm by ion irradiation. The unirradiated area of each sample serves as a reference. For sample A, the columnar defects (CDs) are arranged with a lattice spacing of (302 ± 2) nm, whereas for sample B the lattice spacing is about 500 nm.

6.1.1 Substrate

MgO single crystals of size 10 mm × 10 mm and 1 mm thickness were used as substrates in YBCO pulsed-laser deposition (PLD) for both samples. To control the sample's lattice orientation, the lattice parameters of the substrate and the sample's desired crystallographic orientation should match as precise as possible. Here, YBCO is grown epitaxially with its c axis being perpendicular to the (100) plane of the MgO single crystal. In general, substrates should be chemically compatible with the deposited material to suppress diffusion from the substrate. Furthermore, the thermal expansion coefficients of target and substrate should not differ much, to reduce stresses in the deposited material [105].

6.1.2 Pulsed-Laser Deposition

The setup of PLD consists of an evacuated deposition chamber with the bulk target being placed opposite to the substrate. The rigid polycrystalline target material is produced by mixing and grinding high purity Y_2O_3, $BaCO_3$ and CuO powders, extracting CO_2 and H_2O by calcination, compression to pellets in a hydraulic press at 1 GPa and successive sintering to increase mechanical strength and form grain boundaries.

An optical system focuses a 248 nm KrF-excimer-laser beam and scans it across the target surface. The target material is ablated by short laser pulses of about 20 ns at a repetition rate of 10 Hz and a laser fluence of 3.2 J cm^{-2}. The plasma plume of vaporized target material is repelled from the target surface by electrostatic interactions and condenses on the substrate in epitaxial growth, forming multilayers with smooth surface including droplets, particulates and outgrowths. The sample stage is heated to enhance diffusion of atoms in the sample to their respective lattice sites; the vacuum chamber is cooled.

The main advantage of the pulsed ablation is the suppression of energy dissipation into the bulk target for optimized parameters such as target-substrate distance, laser fluence, pulse rate, substrate temperature as well as type and pressure of the background gas [103, 106, 107]. Thus, the actual stoichiometric composition of the ablated target volume is transferred into the plasma and the residual target material's stoichiometry is preserved.

The as grown YBCO film has a thickness of about 210 nm and is annealed in 800 mbar oxygen atmosphere at elevated temperatures to annihilate surface defects and compensate oxygen deficiency. After annealing, the sample is slowly cooled in an oxygen atmosphere of 0.7 mbar to obtain optimum oxygen doping of $YBa_2Cu_3O_{7-\delta}$. After oxygen treatment, circular Ag contact pads of 1 mm diameter and 100 nm thickness are sputtered onto the films of sample A and B, whereas an additional Au layer is sputtered on top of the Ag contact pads for sample A.

6.2 Sample Design by Photolithography

Each thin film sample is structured to two equivalent areas of standard six probe measurement architecture by photolithography (fig. 6.1). For each sample, one of these areas is processed by masked ion-beam irradiation, whereas the other serves as unirradiated reference sample.

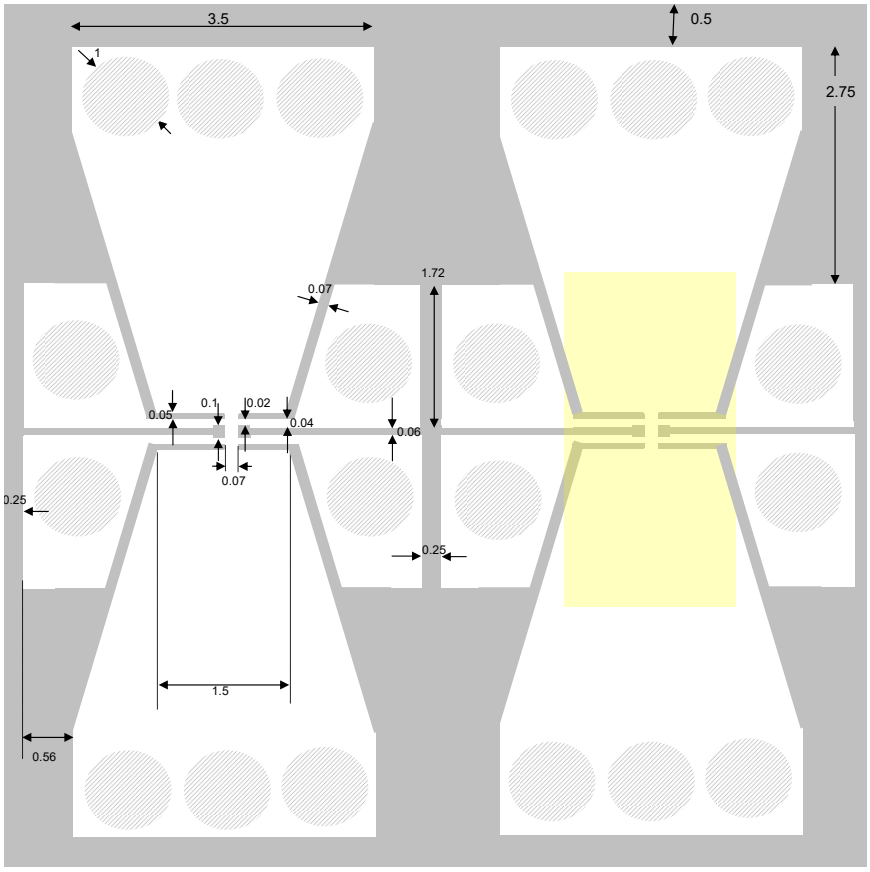

Figure 6.1: Schematic representation of the sample architecture used as a mask for photolithography. Distances are given in mm. [108]

The superconductor's in-plane electrical resistivity is probed on a small bridge of size 60 μm $\times$ 100 μm. Three contact pads at the top and bottom of each area are connected to the source current. On each side, two contact pads with a distance of 100 μm enable the measurement of longitudinal and transverse voltage drop, respectively.

The YBCO thin film is spin coated with a photoresist of 1.5 μm thickness. The architecture mask is placed on top of the photoresist layer and processed by UV-photolithography. The solvent of the photoresist is removed by heating and the YBCO film below the irradiated area is dissolved by wet chemical etching.

After patterning the sample architecture, the photoresist is removed in an area of 2 mm in diameter around the sample bridge by UV-photolithography. The remaining photoresist protects the current tracks and contact pads from irradiation and serves as a platform for the silicon stencil mask used for ion irradiation. The photoresist is removed with acetone after ion irradiation [107, 108].

The superconducting transition temperature of the reference area of sample A is $T_c \sim 90$ K at transition width $\Delta T_c \sim 1$ K with critical current density $j_c \sim 3$ MA cm^{-2} at 77 K. The critical temperature of reference sample B is $T_c \sim 89$ K with a critical current density of $j_c \sim 4$ MA cm^{-2} at 78 K.

6.3 Masked Ion Beam Structuring

In Masked Ion Beam Structuring (MIBS) a patterned stencil mask is placed at some distance of a thin film and processed by ion irradiation with ion beams of large cross section and low beam divergence [76]. The mask protects the YBCO thin film solely in unperforated areas, such that the pre-defined pattern is directly projected onto the material (fig. 6.2).

The effect of ion irradiation on the irradiated material strongly depends on the ion's atomic number, its energy and irradiation fluence, as discussed in chapter 2.4. However, for thin films of HTS and proper irradiation parameters, MIBS allows to directly modify the material's electric properties by introducing point defects without ablation of the material, in contrast to ion milling [81].

The main advantage of this technique is the contactless single-step processing and its potential scalability in parallelization, whereas common patterning techniques such as photolithography include photoresist coating and chemical etching. In MIBS processing, underetching or surface degradation are prevented, allowing for epitaxial growth of additional layers. The technique's resolution essentially depends on the irradiation parameters and dimensions of the stencil mask. Low ion-beam divergence and reduced straggling of ions and collision cascades is favorable [76].

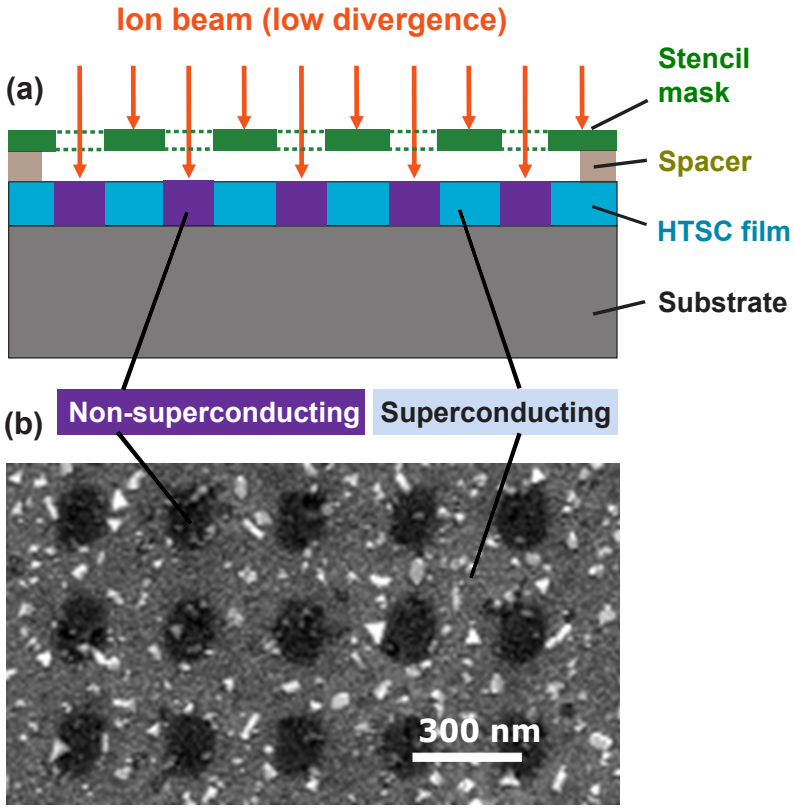

Figure 6.2: A schematic representation of the MIBS processing is shown in figure (a). The Si stencil mask blocks the ion irradiation at unperforated areas, such that the superconducting material is locally protected from direct irradiation. The patterned areas of the stencil mask are directly projected onto the sample. Figure (b) shows a scanning electron microscopy (SEM) recording of the film surface after irradiation with 75 keV He^+ ions at a fluence of 3×10^{15} cm^{-2}. The contrast in the SEM recording arises due to a variation of the escape rate of secondary electrons for modifications in local electronic properties. The bright flakes could be diamond remnants of chemical-mechanical polishing used in the scanned sample [107]. Reprinted figure with permission from G. Zechner *et al.*, Phys. Rev. App., 8.1 (2017). Copyright (2017) by the American Physical Society [58].

Each sample examined in this thesis consists of two identical areas per substrate, which are structured to enable four-point measurements on identical bridges of size 60 μm $\times$ 100 μm. For each sample, one of these areas is irradiated with 75 keV He^+ ions at a fluence of 3×10^{15} cm^{-2} through a commercial Si stencil mask of 2 μm thickness, produced by *IMS Nanofabrication*. Both Si stencil masks are patterned with a square array of columnar perforations with diameter of (180 ± 5) nm. However, the spacing of these holes differs. Sample A is patterned using a stencil mask of (302 ± 2) nm lattice spacing, whereas sample B is patterned with a lattice spacing of 500 nm.

The masks are manually placed on top of a photoresist ring with a distance of 1.5 μm to the YBCO film. The alignment of the masks with respect to the sample bridges is accomplished by marker holes perforated into the mask and monitored through an optical microscope (fig. A.1). The alignment uncertainty is estimated to be 0.3° for sample A and $(1.0 \pm 0.5)°$ for sample B. The masks are fixed to the

substrate with silver paste. In mounting the mask to sample B, silver paste crept between the YBCO film and the mask. However, the bridge was not affected and the silver paste was removed by ultrasonication in ethanol.

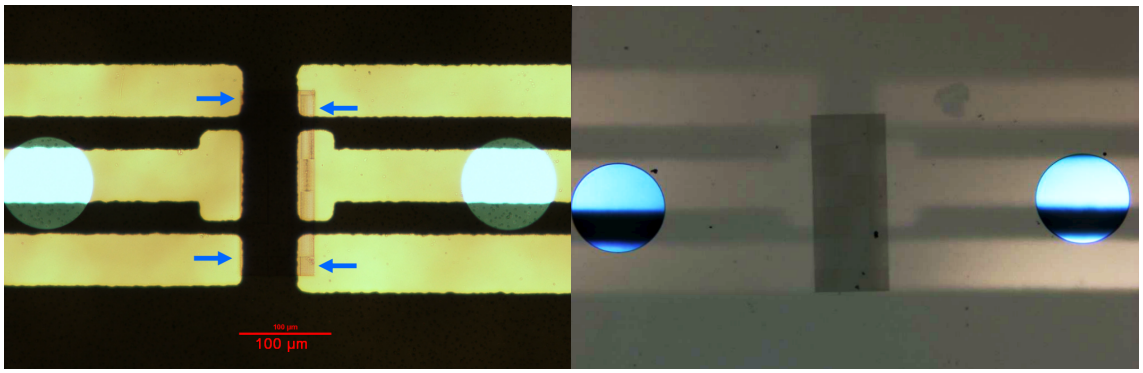

a) Mask alignment of sample A **b)** Mask alignment of sample B

Figure 6.3: Photographs of mask alignment under optical microscope: a) sample A in transmitted illumination b) sample B in incident illumination. [108]

Irradiation with 75 keV He^+ ions is performed at room temperature in a commercial ion implanter (*High Voltage Engineering Europa B. V.*) with rapid lateral beam scanning at 3 cm × 3 cm exposure field. The incident beam is set perpendicular to the film surface with beam divergence below 1 mrad [109]. Ion current density is kept below 0.2 μA cm^{-2} and monitored by Faraday cups to achieve an accumulated fluence of 3.0×10^{15} cm^{-2}. The sample stage is cooled to suppress oxygen depletion through heating.

After irradiation, the critical temperature is reduced depending on the CDA lattice spacing [81]. The critical temperature decreased to $T_c \sim 47$ K for sample A and $T_c \sim 83$ K for sample B, respectively.

7 Experimental Setup

7.1 The Closed-Cycle Cryocooler

The closed-cycle cryocooler *Leybold-Haereus RGD210* is composed of a water-cooled compressor unit, which provides compressed He gas to the refrigerator cryostat as the working fluid. The cryostat is based on a Gifford-McMahon cooling cycle, in which a regenerator is built into the cryopump head [110, p. 80]. The high pressure He gas passes the regenerator on its way into the expansion space and exchanges its excess heat. The coldhead stage is cooled through He gas expansion. A rotary valve switches the expansion space connection from high to low pressure, such that the low pressure gas is released, cooling the regenerator. The gas is then fed back to the compressor unit in a closed cycle. The separation of compressor unit and cryostat suppresses vibrations of the cooling stage.

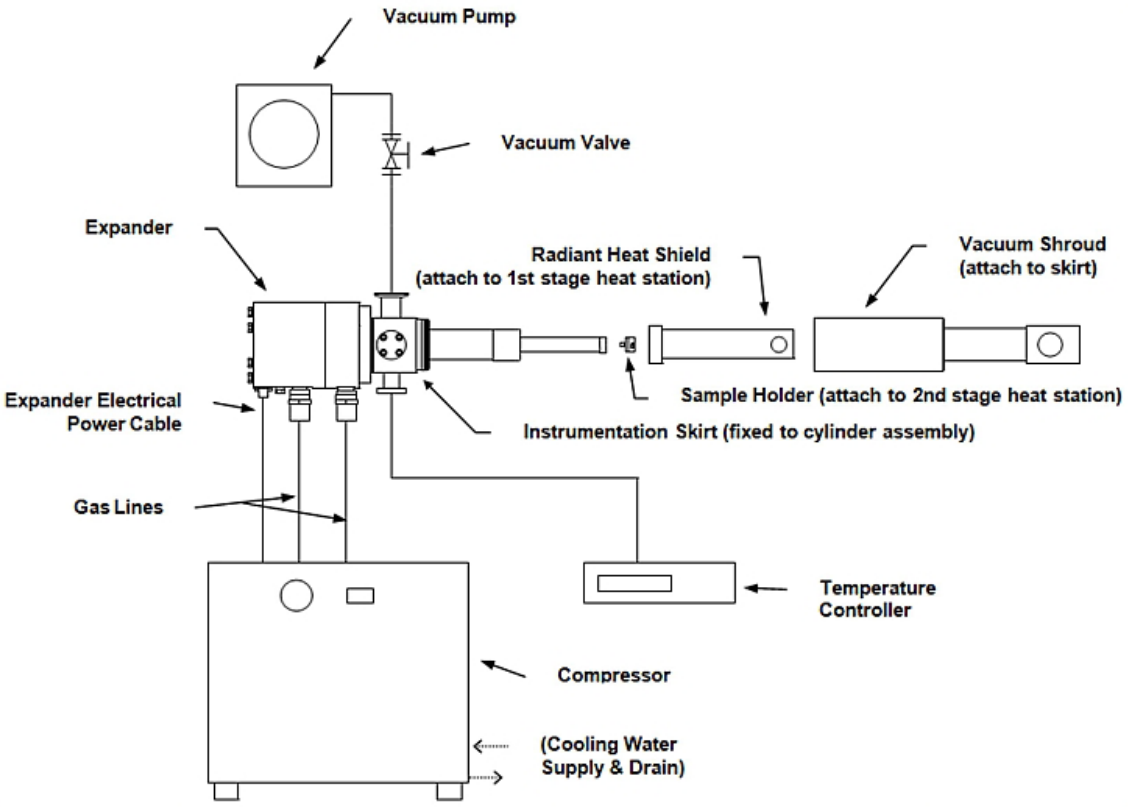

Figure 7.1: Schematic representation of the experimental setup. Reprinted figure with permission from *Advanced Research Systems* [111].

The cryocooler is subdivided into two cooling stages with separate temperature levels, as shown in figure 7.1. Thereby, the first cooling stage provides the operating temperature for the second cooling stage, which cools a copper rod with the sample attached from room temperature down to about 10 K.

An aluminum thermal radiation shield is connected to the first cooling stage. It absorbs the thermal radiation emitted by the surrounding vacuum shroud, which is mounted to the cryostat with vacuum grease and thread screws to ensure alignment and tightness. The vacuum chamber is connected to a *Pfeiffer HiCube* turbo pump, which provides a pressure of about 10^{-4} mbar at room temperature and reaches pressures below 10^{-6} mbar at low temperatures. The vacuum protects the coldhead from heat conduction and enables low operating temperatures. Furthermore, the vacuum prevents condensation of water vapor on the sample, which could mechanically damage the sample upon desublimation.

7.2 The Sample Stage and its Connection

The copper rod is screwed to the second cooling stage, where an additional layer of cryogenic high-vacuum *Apiezon-N* grease provides thermal conduction. The sample is mounted on a copper cylinder at the end of the copper rod and contacted to six pins on the sample stage. Holes are drilled through the copper block to connect incoming wires to the pins. The wires are wrapped to the copper rod with Teflon tape to avoid contact with the thermal radiation shield and keep them at low temperature, preventing heating of the sample. The wires of the copper rod are soldered to a D-SUB DE-9 jack, which is connected to an electrical feedthrough, leading to an external distribution box. A detailed documentation of the copper rod construction can be found in the thesis of Göb [112].

A *Cernox* temperature sensor [113] is placed inside a drilled hole below the sample and connected to a *LakeShore 336* temperature controller. Moreover, the temperature controller powers a heating coil, which is placed at the front end of the sample stage. Since the cooling stage constantly operates at full cooling power, the copper cylinder is heated to a given temperature value in a feedback loop of temperature and heating power. The temperature stability depends on the temperature level considered. However, for measurements below 40 K, the heating element operates at low range, thus the stability is about ± 1 mK. The sample stage is covered by a copper cap, which is screwed on the rear end of the copper rod to ensure homogeneous temperature distribution and suppress direct incidence of thermal radiation onto the sample.

The contact pads of the samples are connected to the sample stage pins using 50 μm thick gold wires. The wires are carefully placed on top of the contact pads under an optical microscope using a tweezer and fixed by manually dripping off a drop of silver paste (*ÖGUSSA Leitsilber 200*) on top of the wire. Sample A was mounted to the sample stage using cryogenic high-vacuum *Apiezon-N* grease, whereas silver paste was used for sample B to provide better thermal conductance.

Figure 7.2 presents a picture of sample A through the optical microscope. The outermost pins (1 and 6) provide the source current, whereas the pins 2, 5 and 3, 4 are voltage contacts. Typically, the sample is contacted such that the longitudinal voltage is measured on the pins 2 and 5. Contacts 3 and 4 could either be used as a backup for longitudinal voltage measurements, or for transverse Hall voltage measurements with respect to pins 2 or 5, which are not considered here.

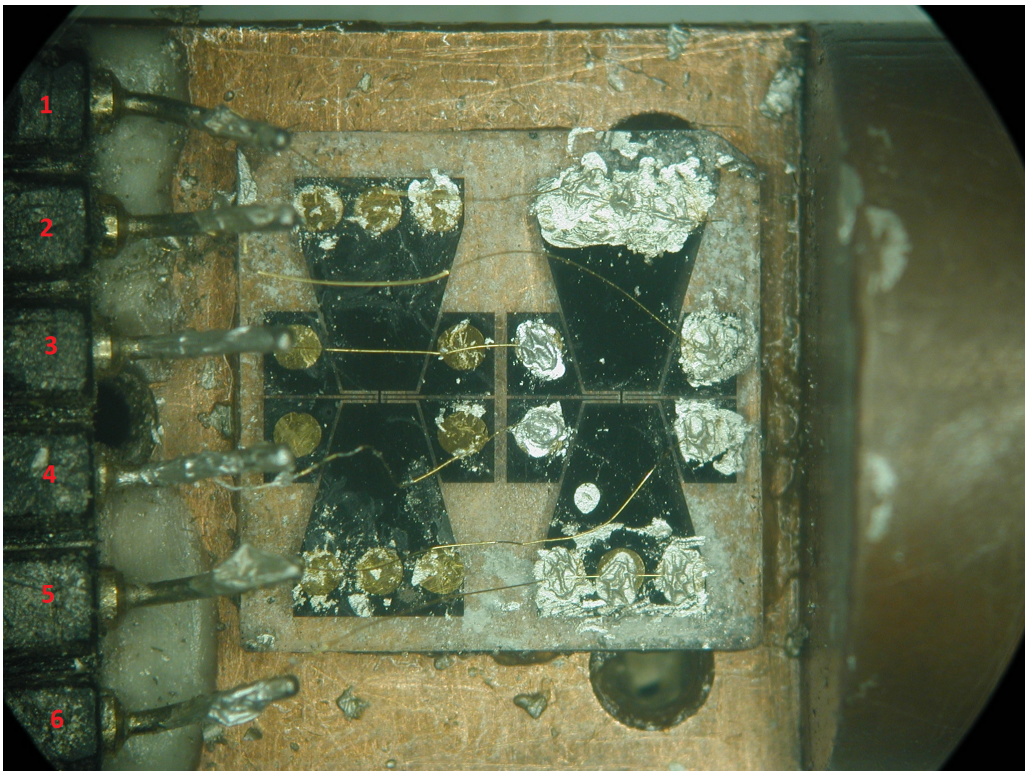

Figure 7.2: Mounting of sample A (right) to the sample stage with cryogenic high-vacuum *Apiezon-N* grease. Pins 1 and 6 lead the source current. Pins 2 and 5 are connected to the rightmost contact pads to measure the longitudinal voltage drop. Pins 3 and 4 are connected to the inner contact pads, which are not used in this measurement. The unirradiated reference sample on the left is not contacted. Pin numbers are indicated in red.

7.3 The Electromagnet

The cryostat is mounted on a scaffold, such that a magnetic field can be applied to the sample. The *Bruker B-E 15 C8* electromagnet is water cooled and powered by a *FUG NTN 4200M-125* power supply with an operating current up to 30 A. The distance of the magnet poles to the sample can be set independently. For short pole distances the magnetic field exceeds 1 T at both polarities. In the experiments conducted, the gap size was about 15 cm and the maximum magnetic field used was about 100 mT. In this setup, an increment of 5 mA of the supply current corresponds to an increment in magnetic field of about 0.16 mT.

A *LakeShore HSE* high-sensitivity transverse Hall probe is controlled by a digital *LakeShore 475 DSP Gaussmeter* to measure the magnetic field. It is mounted on the left magnetic pole, with its plastic cover being tightly taped to the magnet and its active area of 1 mm in diameter centered at sample height. It is thus turned with the magnet rotation. The Hall probe is aligned parallel to the magnetic field by determining the maximum signal of the probe at constant magnetic field of about 90 mT and fixed inside its cover. The minimum sensitivity of the HSE probe is stated as 0.5 μT in the magnetic field range considered. This value is accurate to 0.4% at a variance of 5° tilt angle in any axis. For slight variations in probe positioning, a

maximum variation of 0.2% was found, which corresponds to a maximum uncertainty of $\Delta B = 0.2$ mT at full range considered in this experiment.

7.4 Sample Orientation

The critical current of sample A was measured with the applied magnetic field being parallel to its c axis and mounted as shown in figure 7.2. In contrast, the angle dependence of the magnetoresistance of sample B is measured in constant Lorentz force geometry of the magnetic component.

$$\vec{F} = q(\vec{v} \times \vec{B}(\alpha)) \rightarrow |\vec{F}| = q(|\vec{v}| \cdot |\vec{B}|) \tag{7.1}$$

Thus, the current through the sample needs to flow parallel to the rotation axis of the magnet. In other words, the magnetic field must be perpendicular to the current density upon rotation: $\vec{B}(\alpha) \perp \vec{j} \quad \forall\alpha$. This geometry is realized by rotating the sample as depicted in figure 7.3, such that an angle of $\alpha = 90°$ corresponds to the magnetic field being perpendicular to the irradiated columnar defects.

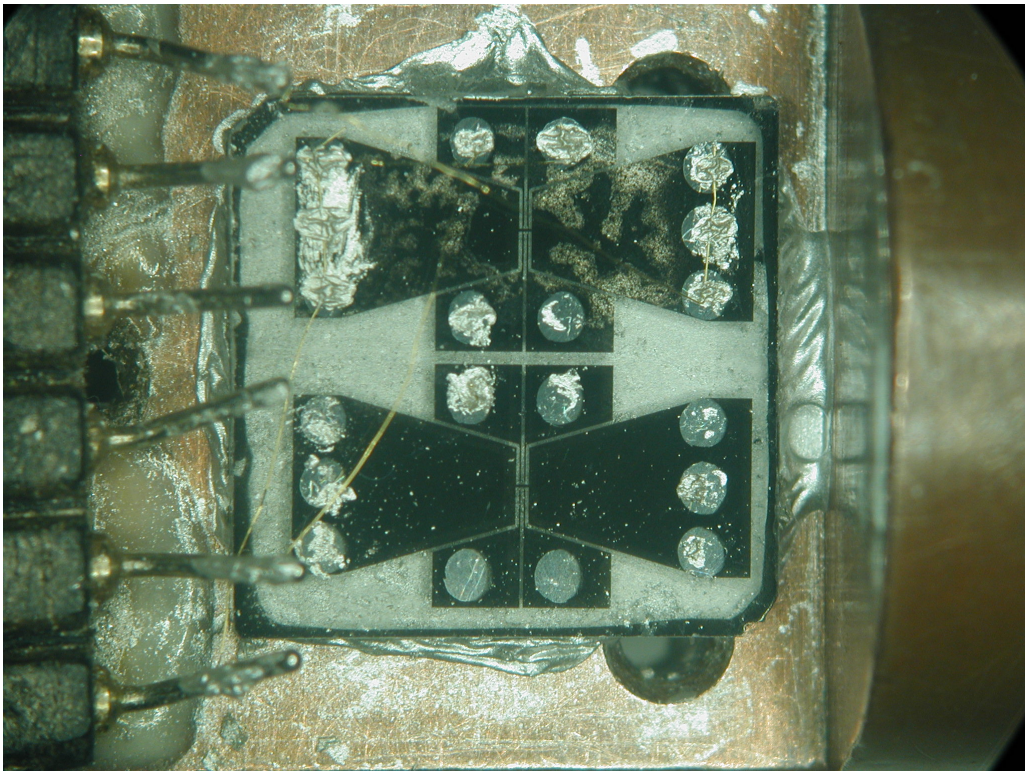

Figure 7.3: Contacting of the $d = 500$ nm sample to the sample stage with silver paste in constant Lorentz force geometry. Pins 1 and 6 are connected to the current source. Pins 2 and 5 are connected to the upper gold pads to measure the longitudinal voltage drop. The unirradiated reference sample on the bottom is not contacted.

7.5 Angle Dependence

The magnet is mounted on a revolvable base. The angle $\alpha = 0°$ corresponds to the magnetic field being applied parallel to the sample's c axis and thus parallel to the CDs. The angle was calibrated by setting the magnetic field to 227 mT and searching for the minimum in the magnetoresistance of sample A at 44 K. The maximum magnetoresistance is found at $\alpha = 90°$. The circumference of the revolvable base is 138.7 cm. The arc length between these two position is 35.0 cm. Thus, the mean value of 0.3865 cm/1° is used to determine the other angle positions. This scale is only valid for a given position of the cryostat. The maximum uncertainty of calibration, scale and magnet alignment to scale is $\Delta\alpha = 0.5°$.

However, the cryostat had to be slightly shifted at 75°, such that the gaussmeter passed the vacuum shroud. The scale was not recalibrated, such that for angles 75° and 80° a maximum uncertainty of $\Delta\alpha = 1°$ is assumed. The cryostat needed to be shifted again at 85° of original scale, such that at 90° of original scale the magnetoresistance still showed matching peaks. Thus, evidently the scale needed to be recalibrated by determining the maximum magnetoresistance of sample B at 81.7 K and 32 mT. The alleged angles 85° and 90° of original scale could be recalculated to 86.4° and 91.7°, respectively. The latter measurement is projected to 88.3°, since the situation is symmetric.

7.6 Measurement Devices and Routines

The measurements are conducted in standard four-probe geometry, where the longitudinal DC voltage drop on the superconducting bridge is measured in a parallel circuit with high resistance in the voltmeter. The current supplied to the sample is generated by a *Keithley 2400* source-meter. The longitudinal voltage drop is measured by a *Keithley 2181A* nanovoltmeter. The latter provides two measurement channels, whereby the first channel is used due to its higher resolution throughout the experiment. The measurement device uncertainty is orders below systematic uncertainties from thermal fluctuations or electronic noise. Thus, uncertainties are not considered in current-voltage characteristics.

The source-meter, nanovoltmeter, magnet power supply, temperature controller (sensor and heating) and gaussmeter are connected to a measurement computer via GPIB and controlled by measurement routines written in *TestPoint*. Detailed documentation of the program routines can be found in the thesis of Zechner [63].

7.6.1 Critical Current

In this measurement routine the critical current is determined by a voltage criterion of 100 nV, corresponding to 10 μV cm^{-1} at given temperature and applied magnetic field.

The measurement is started with an applied current of 1 μA. The longitudinal voltage V_p is measured after 0.2 s of current settling time. Next, the current polarity is changed and the longitudinal voltage V_n of opposite sign is measured. Thermal

voltage signal is eliminated by determining the difference of both voltages, since it always is of same sign, such that the mean sample voltage is given by $V_{\text{sample}} = \frac{1}{2}(V_p - V_n)$. This sample voltage will be simply termed voltage hereafter.

If the previously measured voltage was below 88 nV, an average of two voltage measurements (*coarse reading*) is taken at the momentarily applied current. If the previously measured voltage was above 88 nV, an average of 10 voltage measurements is taken (*fine reading*), to allow for better resolution (fig. 1.8). The measured voltage is then checked for the voltage criterion. If the criterion is not met, the current is increased by 1% in *coarse* or 0.1% in *fine reading*, respectively.

This procedure is applied until the voltage criterion is met. Once the voltage criterion is met, the measured set of current-voltage data at the given applied magnetic field is saved. The obtained critical current and its corresponding magnetic field and temperature are stored separately.

Next, the current supplied to the magnet is altered by 5 mA in a given direction, corresponding to a change in magnetic field of about 0.16 mT. After a settling time of 5 s, the starting current of the successive run is set to 80% of the previously determined critical current. It is lowered by the same amount, if the voltage criterion is met immediately. The procedure of determining the critical current at an applied magnetic field is repeated until the measurement is terminated manually. An example of the routine interface is given in figure 7.4.

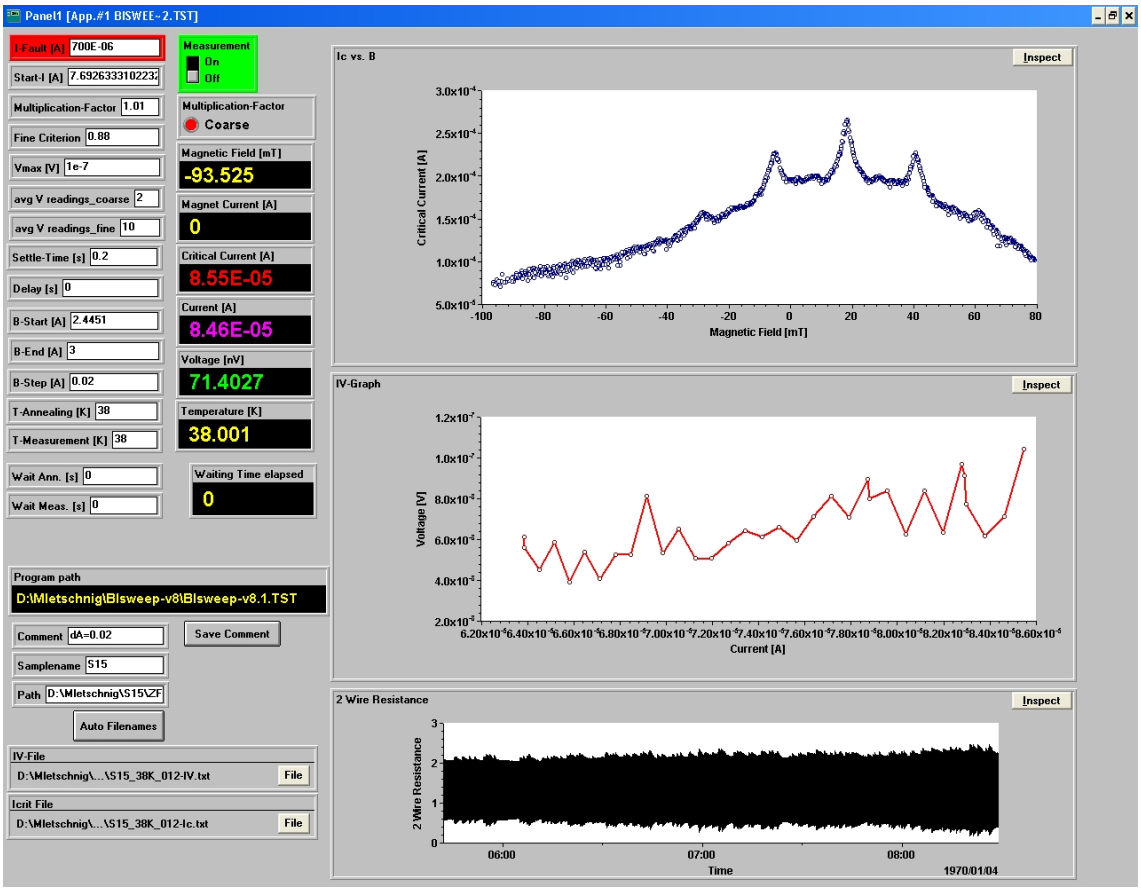

Figure 7.4: TestPoint routine user interface to determine the critical current.

7.6.2 Magnetoresistance

In this measurement procedure, the longitudinal voltage drop is measured at a constant bias current of 200 μA at given temperature and applied magnetic field. The voltage is measured after 0.2 s of current settling time. The longitudinal voltage drop is determined by calculating the average of 10 voltage measurements. Again the sample voltage is determined as the difference in voltage of periodical reversal of polarity, as described in section 7.6.1.

If the longitudinal voltage is obtained, the current supplied to the magnet is altered by 5 mA in a given direction. The procedure of determining the longitudinal voltage at applied magnetic field is continued after 5 s of settling time and repeated until the measurement is terminated manually. The magnetoresistance can be calculated by dividing the longitudinal voltage by the applied current of 200 μA. An example of the routine interface is given in figure 7.5.

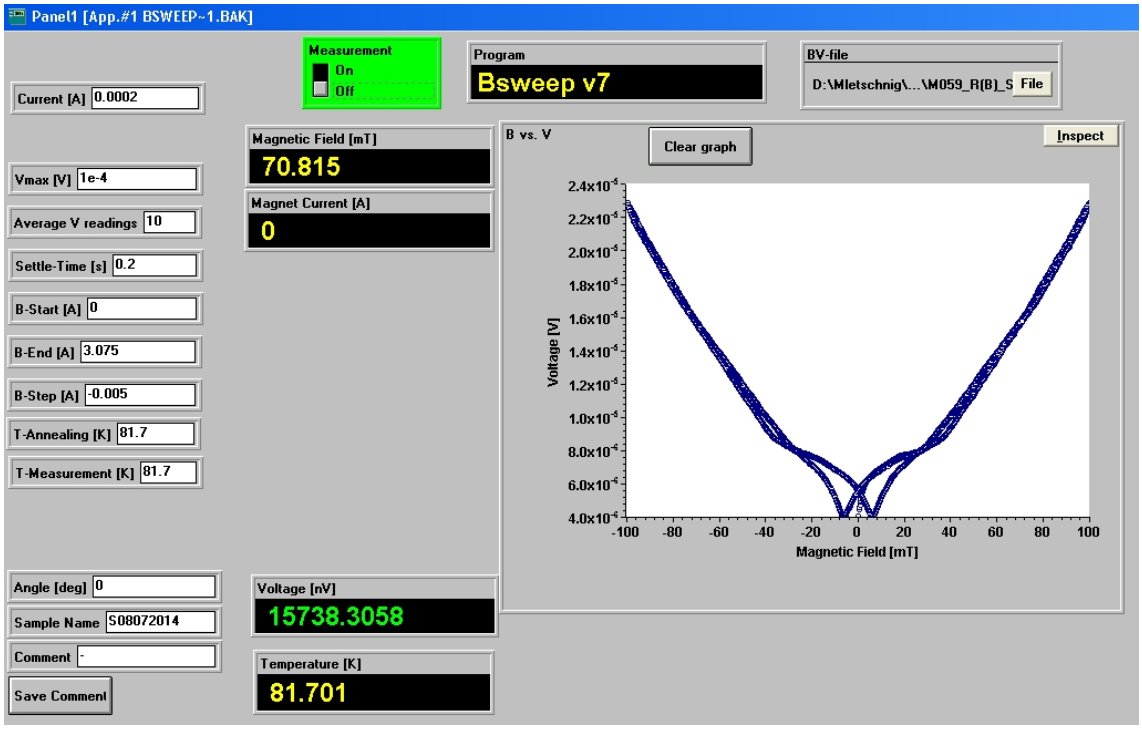

Figure 7.5: TestPoint routine user interface to determine the magnetoresistance.

8 Unconventional Critical State[1]

8.1 Field-Cooled Down-Ramped Measurement

Zero field-cooled measurements provide the virgin curve of critical current hysteresis. However, only one initial state is probed, where vortices enter a field free sample upon ramping up the magnetic field. A possibility of investigating alternating non-equilibrium vortex arrangements with well defined initial magnetization conditions is obtained by applying different field-cooled magnetic fields B_{FC}, which are down-ramped while the sample remains in the superconducting state.

Field-Cooled Down-Ramped Procedure

Field-cooled down-ramped data is acquired by applying a magnetic field B_{FC} to the sample in its normal state. Initially, an equilibrium vortex arrangement is established upon cooling the sample in-field below the superconducting transition temperature T_c. The critical current $I_c(B_a)$ is measured for decreasing applied magnetic field B_a while keeping the sample in the superconducting state.

The peaks of I_c can be understood as a consequence of two different vortex pinning mechanisms. On one hand, n fluxons can be trapped in the normal-conducting core of a CD. These pinned fluxons are not moved by the transport current applied to the sample. Only by changing the applied magnetic field, the Lorentz force due to shielding currents exceeds the pinning potential and the fluxons can hop between neighboring CDs due to mutual repulsive forces and repulsion from the sample's boundaries [114].

On the other hand, vortices at interstitial positions between the CDs are weaker pinned. The critical current shows a peak when most available fluxons are trapped in the CDs due to commensurability effects. At the same time, the number of weaker pinned interstitial vortices that can give rise to dissipation is smallest.

The critical current of the sample is determined by the motion of interstitial vortices in a small region near the edge of the sample [115] and does not lead to a redistribution of the strongly pinned fluxons in the CDs.

[1] Most of this section is reproduced from [59].

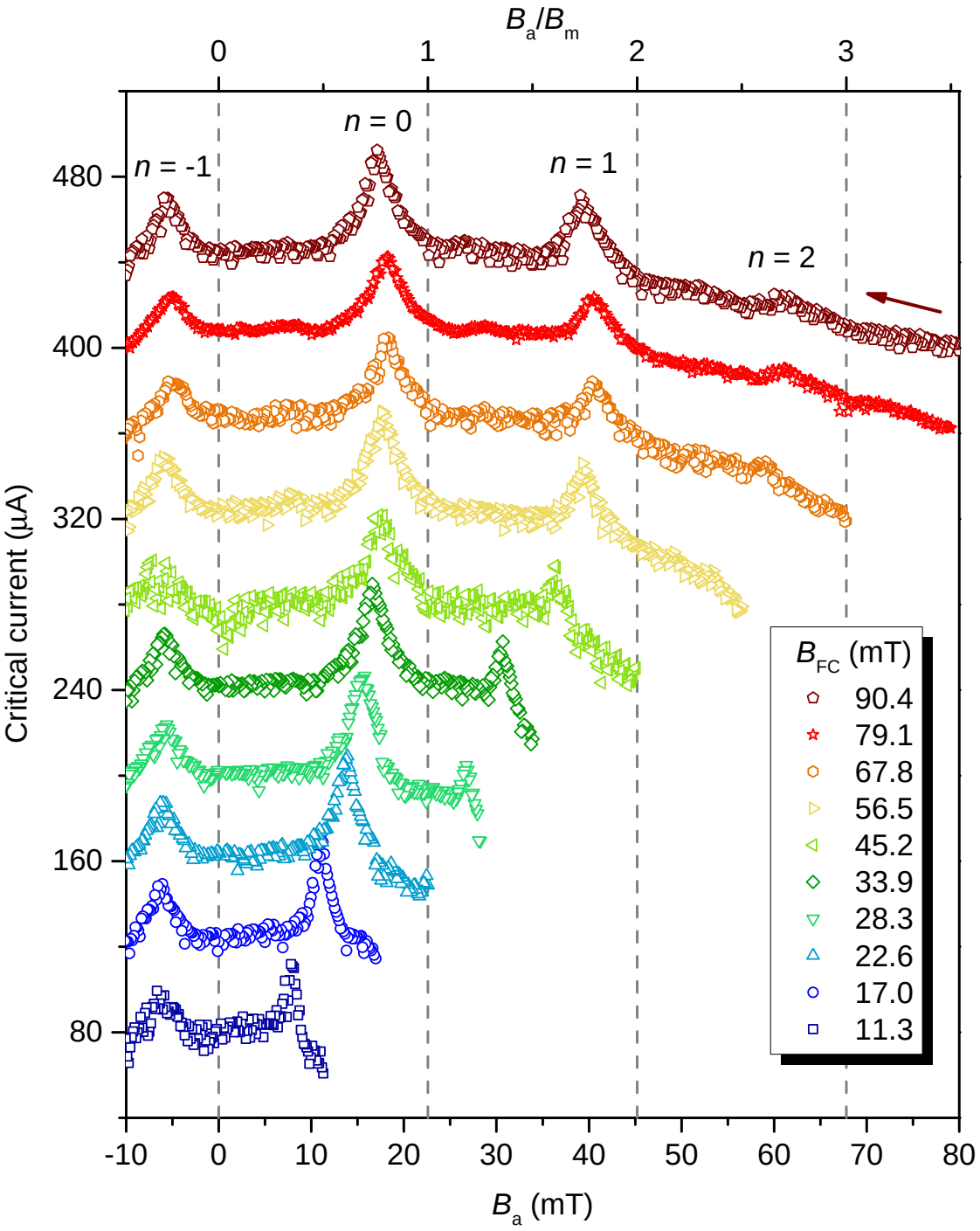

Figure 8.1: Critical current I_c measured during down-ramps of the applied magnetic field B_a after establishing an equilibrium vortex arrangement by in-field cooling from 100 to 38 K ($T/T_c = 0.78$) for several initial magnetic fields B_{FC}. The curve at $B_{FC} = 11.3$ mT is to original scale. Data for higher B_{FC} fields are displaced by +30 μA for better visibility.

Adaption of the Generalized Critical State Model

The generalized critical state model presented in equation 1.15 is adapted to account for the matching conditions of higher order by introducing a superposition of individual critical current peaks at a given temperature $I_{c,n}$ [116], with each contribution shifted to the position of its matching field B_n. The position of the measured matching field B_n of n^{th} order is assumed to be a fitting parameter, to allow for shifts due to the hysteretic behavior.

$$I_c(B) = \sum_{n=0}^{n_{\max}} \frac{I_{c,n}}{\left(1 + \frac{||B|-B_n|}{B_0}\right)^{\beta}} \tag{8.1}$$

In this case, the current is considered instead of the current density, since the applied current is known, but the actual cross-section can not be easily determined.

Critical current data for each initially field-cooled magnetic field B_{FC} presented in figure 8.1 are fitted by a multi-peak fit using equation 8.1. The resulting multi-peak fits are presented in figures D.1 and D.2 in the appendix. The determined matching fields for $n = 0$, $n = 1$ and $n = -1$ of the peaks as well as the distances between peaks $n = 1$ to $n = 0$ are displayed in figure 8.2.

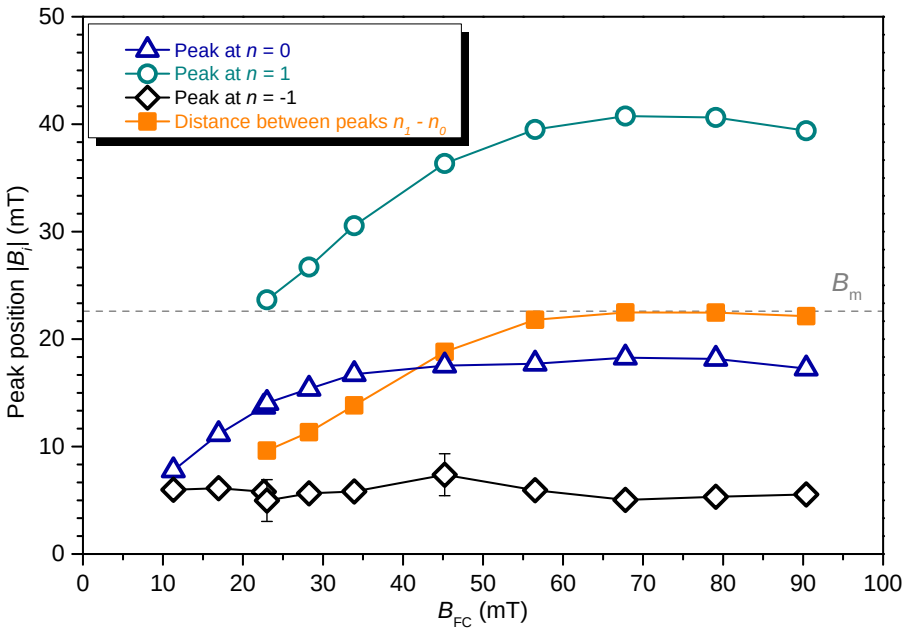

Figure 8.2: Positions of the critical current peaks from figure 8.1 and the distance for peaks $n = 1$ to $n = 0$ as a function of initially in-field cooled B_{FC} and down-ramped B_a. Error bars for $n = -1$ at 23 and 45 mT are determined as 3σ of the standard deviation of the mean for peak positions at $n = -1$ to account for obvious errors in the acquired data shown in figures D.1 and D.2. Otherwise, uncertainties are accounted for by symbol width. Lines are guides to the eye.

8.2 Discussion on Unconventional Critical State

Terraced Critical State

Actually, for vortex-pin lattices, a terraced critical state has been theoretically predicted by Cooley and Grishin [117]. It is characterized by circumferential domains in the sample, inside which the pinning centers are occupied by the same number n of fluxons and neighboring domains by $n \pm 1$. A similar domain structure has been revealed by a two-dimensional dynamic simulation of vortex arrangements in the critical state of superconductors with periodic pinning sites by Reichardt et al. [118] and inferred from scanning Hall probe measurements in a perforated Pb thin film by Silhanek et al. [119]. Another important consequence of such state is that the shielding currents are stratified into streamlines between the terraces and vanish inside, as indicated by gray areas in figure 8.3. Hence, the local current density in the streamlines is higher than its average over the sample's width.

ZFC Virgin Curve

The fact that the $n = 1$ matching peak is observed already at $B_1 \sim 10$ mT $< B_m$ indicates a pronounced critical state with a domain of commensurable vortex pattern near the sample's edge [58] as it is outlined in figure 8.3(a). Upon further rising B_a, vortices propagate towards the interior of the sample and another domain at the edges forms, filled with two fluxons per CD resulting in $B_2 \sim 30$ mT $< 2B_m$ establishing a terrace-like profile of the critical state, see figure 8.3(b).

Down-ramp

It is instructive to investigate the reverse situation, where a finite B_{FC} is applied during cooling below T_c, thus allowing initially for an equilibrium arrangement of vortices and a field-saturated state within the sample. Field-cooling the sample with $B_{\mathrm{FC}} > 80$ mT before B_a is ramped down leads to an identical behavior as the one shown as the topmost curve in figure 8.1, which, thus, can be seen as representative for higher B_{FC}. In all curves, the critical current peaks appear already at higher fields than predicted by equation 1.13. When B_{FC} is reduced, the peaks are gradually shifted to lower B_a values, except for the $n = -1$ peak. The peak positions are summarized in figure 8.2, where it can be noticed that they remain stable for freezing fields $B_{\mathrm{FC}} > 70$ mT $\sim 3B_m$. Remarkably, the distance between all neighboring peaks at high enough B_{FC} corresponds exactly to the matching field B_m.

Since the critical current is determined by vortex motion near the edge of the sample it probes the features of the outermost domain. Upon lowering B_a the equilibrium state again transforms into a terraced critical state, where the terrace situated near the sample' edge has a local $B_T < B_a$ as depicted in figure 8.3c. When it is populated by exactly one fluxon per CD, i.e., $B_T = B_m$, a peak in I_c appears. Due to the fact that the local field B_T in the outer terrace is lower than B_a, the peak is up-shifted from its equilibrium value of equation 1.13.

Strikingly, the distance between the peaks (orange squares in figure 8.2) equals the matching field B_m for high B_{FC}. According to equation 1.13, this indicates that

exactly one flux quantum per CD is removed over the entire sample area, in line with the prediction of the model of a terraced critical state [117] and discussed in more detail in a report of Zechner et al. [58].

However, in two situations this condition is not met: the virgin curve in figure 1.6 demonstrates that initially the inner parts of the sample are not yet populated by fluxons, as sketched in figures 8.3(a) and (b). Thus, by increasing B_a from B_n to B_{n+1}, one additional fluxon is trapped only in CDs near the sample's edges and the increase in average number of fluxons per CD over the entire sample is smaller than one, resulting in a compressed distance between peaks.

Conversely, by comparing figures 8.3(c) and (d) it is obvious that in the latter case the critical state profile near the samples's center is too flat to allow for extraction of appropriate number of fluxons. In this case, the peaks and their distance are both shifted to lower magnetic fields. A special situation happens at the $n = -1$ peak (after reversal of B_a). It corresponds to a virgin curve, displaced by a small field of opposite polarity still trapped in the center of the sample, since $|B_{-1}| < |B_1|$ of the virgin curve. However, the trapped field is similar whether it was established by ramping B_a down from a high B_{FC} or cooling the sample in an already low B_{FC}.

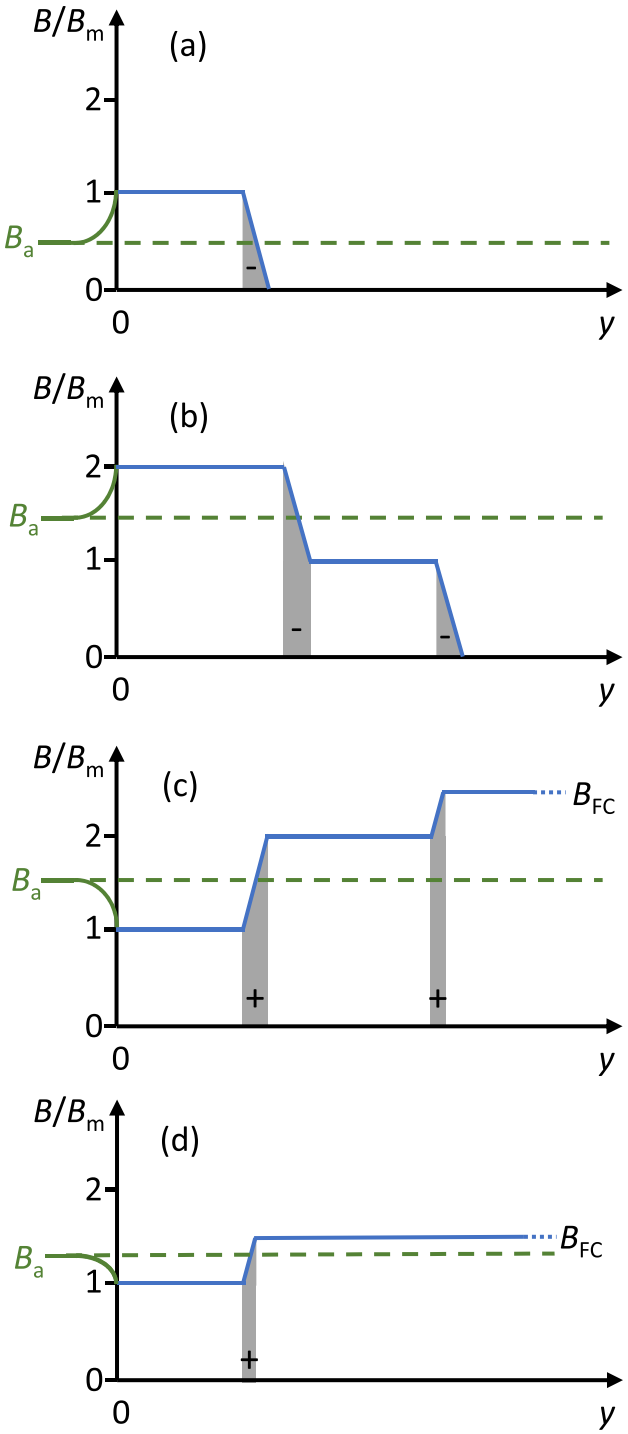

Figure 8.3: Sketch of the proposed terrace-like critical state (not to scale), plotted from the edge of the sample along the width towards its center ($0 \leq y \leq w/2$). The local modulation of B due to vortex cores is ignored. The gray areas show the zones of the stratified shielding currents between the terraces and the sign marks their direction. The applied magnetic field B_a is distorted due to demagnetization effects near the sample's edge. (a) Virgin curve at $n = 1$ matching ($B_a = B_1$). (b) Virgin curve at $n = 2$ matching ($B_a = B_2$). (c) $n = 1$ matching during down-ramping B_a and starting from $B_{\mathrm{FC}} = 2.5B_m$. (d) $n = 1$ matching during down-ramping B_a and nd starting from $B_{\mathrm{FC}} = 1.5B_m$. Reproduced from Superconductor Science and Technology [59] with permission ©IOP Publishing.

9 Angle Dependence of Magnetoresistance[1]

9.1 Measurements on Angle Dependence of Magnetoresistance

To determine whether the pinning of vortices occurs by pinning in CDs or within twin planes and dislocations of same orientation, the magnetoresistance is measured for several tilt angles α of the applied magnetic field B_a with respect to the sample's c axis. Since the applied magnetic field B_a is measured directly at the magnet pole, the incident magnetic field parallel to the defect columns decreases for a tilt angle α according to equation 9.1.

$$B_{\parallel} = B_a \cos \alpha \tag{9.1}$$

In other words, the applied magnetic field needs to be increased by $\cos^{-1} \alpha$ to get the same parallel component of the flux as for untilted magnetic field. The applied magnetic field B_a in the matching condition given by equation 1.13 needs to be replaced with the parallel component given in equation 9.1. Hence, if vortices are pinned by CDs independent by the tilt angle α, the matching peaks shift according to $B_n \cos^{-1} \alpha$ upon tilting the magnetic field. This situation is marked by carets in figure 9.1.

The magnetoresistance data for sample B with a lattice spacing of about 500 nm was acquired by first rotating the magnet to a given tilt angle α and setting the magnetic field to zero with partially compensating the earth's magnetic field. The sample was zero field-cooled from 100 K to 81.7 K for each tilt angle and the magnetic field was ramped up to 100 mT, where direction was changed to measure the down-sweep from 100 to -100 mT. Successively, the up-sweep was measured from -100 to 100 mT, as shown in figure 9.1. The virgin curves are excluded for simplicity.

The magnetoresistance data in figure 9.1 shows minima of the resistance, which for $\alpha = 0°$ coincide with the matching field given by equation 1.13. The low bias current of 200 μA is slightly above the critical current, hence the emergence of matching minima and hysteresis can be explained by the mechanism of reduced vortex mobility by pinning of defects at commensurate vortex arrangements as discussed for critical current data in sections 1.4.2 and 8.2.

The peak positions of the matching fields presented in figures 9.2 and 9.3 are determined by first fitting a parabolic baseline to the magnetoresistance data with emphasis on smooth conformity of the fit to the data for higher magnetic fields. The data is inverted by a sign change after the baseline is subtracted. Next, the obtained peaks are fitted using the adapted generalized critical state model (eq. 8.1) with fixed parameters β and B_0 within each sweep. The data showing multi-peak fits for down- and up-sweep are presented in figures E.1 and E.2 in the appendix.

[1] This section is adapted from [59].

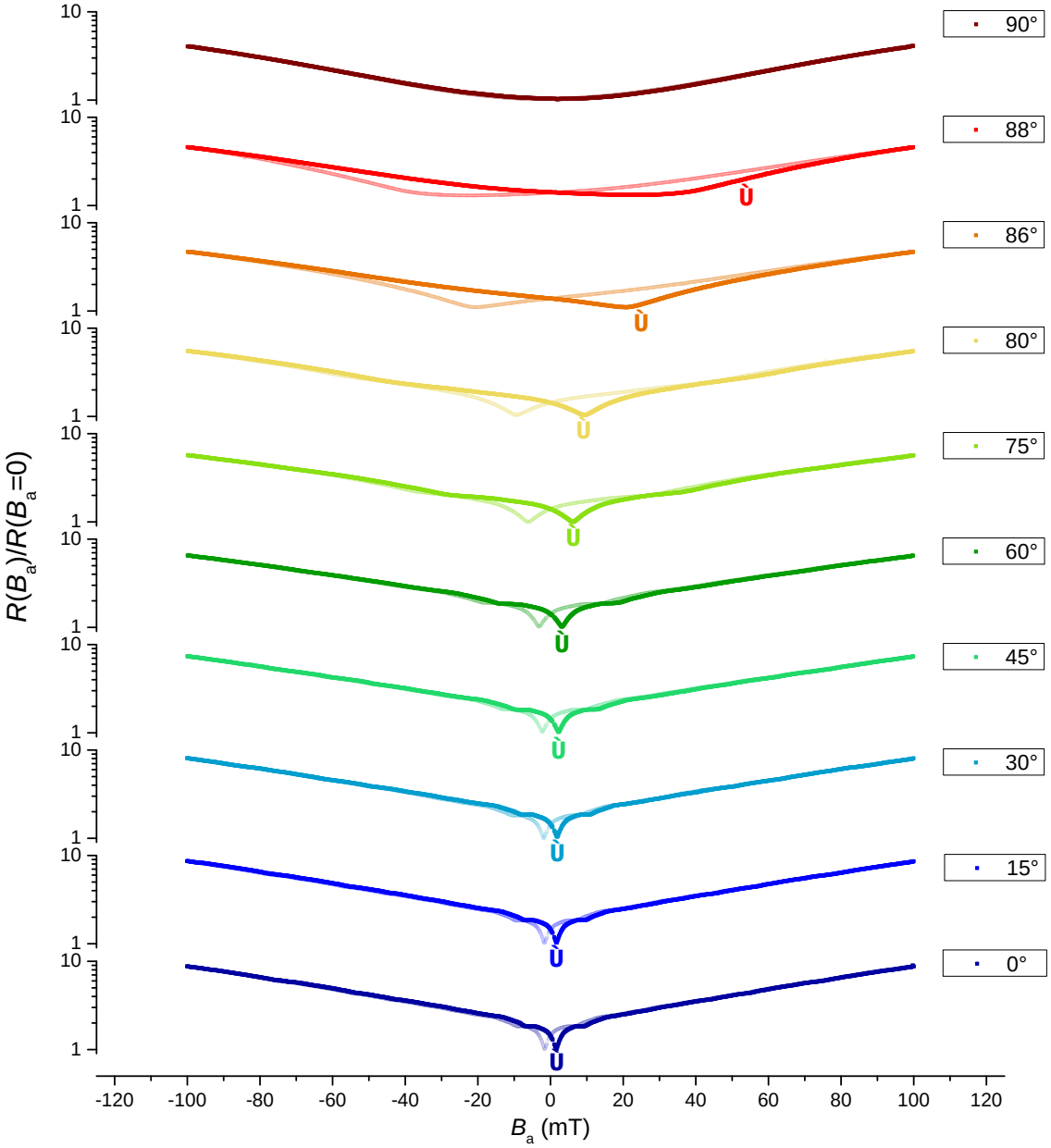

Figure 9.1: Hysteretic behavior of the normalized resistance after zero-field-cooling at several angles between the applied magnetic field and the crystallographic c axis of YBCO at 81.7 K ($T/T_c = 0.98$). Data is recorded with a bias current of 200 μA, which is only about twice the typical critical current at the given temperature. Full symbols denote the down-sweep data, whereas hollow symbols denote the up-sweep data. Virgin curves are excluded for simplicity and successive sweeps produce identical traces. Carets mark equal values of the component of B_a that is parallel to the c axis. Note the semilogarithmic scale. [59][2]

[2]This caption is reproduced with adaptions from [59].

9.2 Discussion on Angle Dependence of Magnetoresistance

The positions of the minima B_n for down- and up-sweep presented in figures 9.2 and 9.3 are scaled to its parallel component by $B_n \cos^{-1}\alpha$. The aspect ratio of the irradiated CDs of diameter $D = 180$ nm at film thickness $t_z = 210$ nm is AR $= D/t_z = 0.82$. The maximum tilt angle above which stiff vortices would exceed the pinning volume of CDs and would need to penetrate into unirradiated areas thus corresponds to $\alpha_{\max} = \tan^{-1}(0.82) \sim 40°$. Hence, a strong shift to lower matching fields might be expected for tilt angles $\alpha \sim 40°$.

However, in figures 9.2 and 9.3 a constant parallel component up to an angle of $\alpha \sim 80°$ can be observed. Furthermore, the difference between the positions of minima corresponds to the matching field $B_m = 8.2$ mT. According to equation 9.1 this corresponds to the situation that positions of minima are shifted precisely according to their altered matching condition without the expected breakdown at $\alpha \sim 40°$. This indicates that vortices are pinned farther than the suggested maximum tilt angle for stiff vortices.

The matching minima of higher order are not visible in the data for tilt angles $\alpha > 80°$. However, the parallel component of the minimum for $n = 0$ shows a drop for tilt angles exceeding $\alpha > 80°$. Hence, the matching peaks occur prior to the modified matching condition. This indicates that the pinning mechanism changes and most probably arises due to intrinsic in-plane pinning, which is expected for tilt angles $\alpha \sim 90°$ [28, 120]. A further indication for pinning due to CDs is the pronounced hysteresis in magnetoresistance as a consequence of a critical state, which breaks down for $\alpha \sim 90°$.

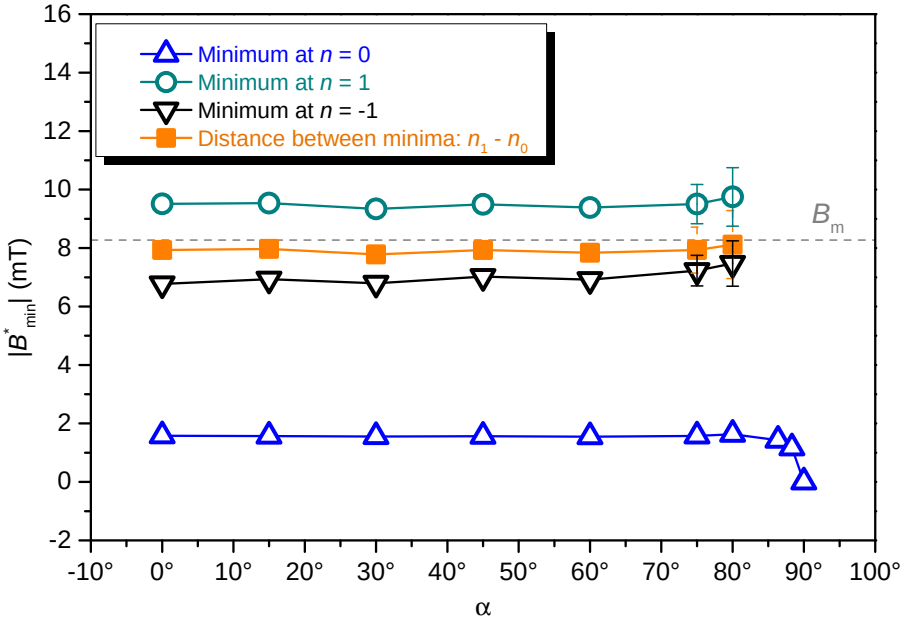

Figure 9.2: Position of the minima for down-sweep data presented in figure 9.1 as a function of the magnetic field's tilt angle α with respect to the c axis of YBCO. Data are scaled to the magnetic field component parallel to the c axis. Uncertainties are accounted for by error bars or symbol width. Lines are guides to the eye.

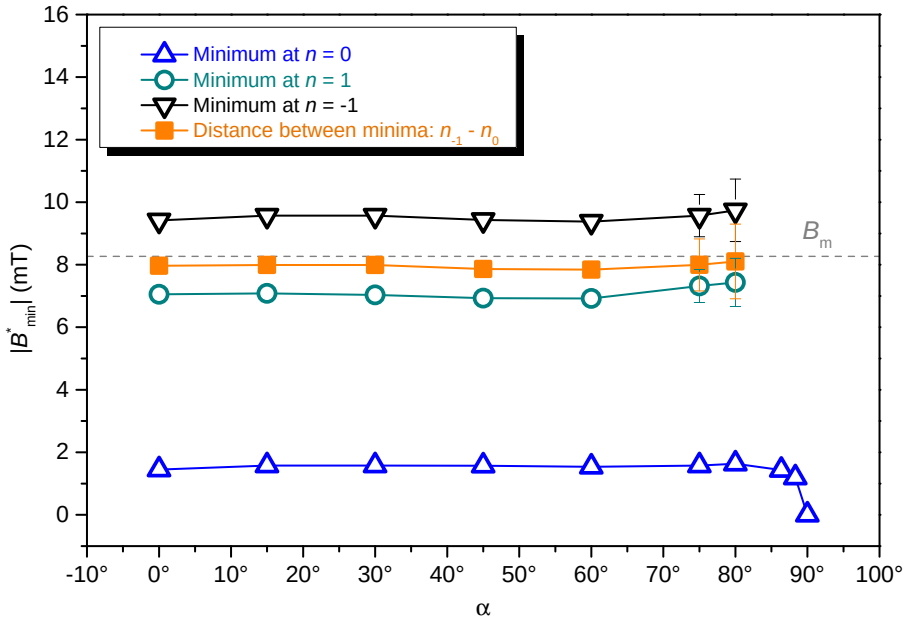

Figure 9.3: Position of the minima for up-sweep data presented in figure 9.1 as a function of the magnetic field's tilt angle α with respect to the c axis of YBCO. Data are scaled to the magnetic field component parallel to the c axis.

Figure 9.4 presents data on angle dependence of the magnetoresistance for sample A with a lattice spacing of $d = 300$ nm irradiated under same conditions. The peak positions at $\alpha = 0°$ and distances between two adjacent minima $\Delta B = B_1 - B_0 \sim B_m = 22.6$ mT are consistent with the topmost curve in figure 8.1.

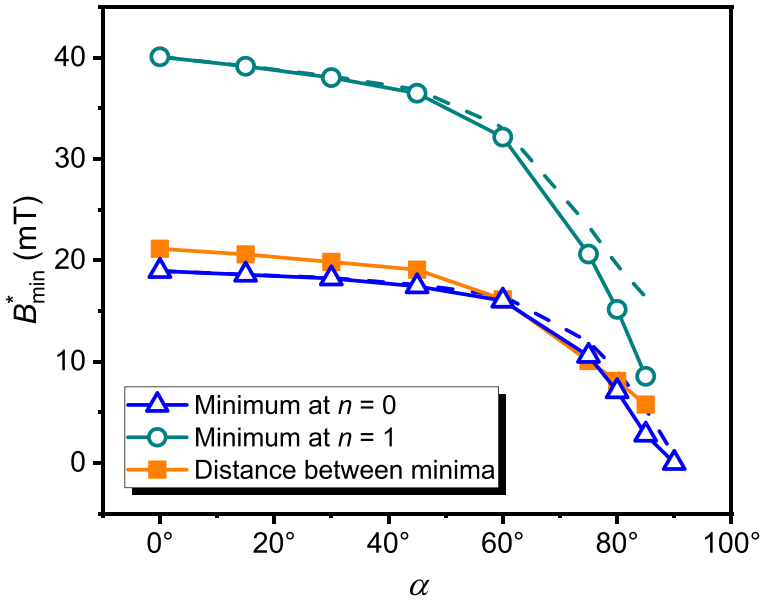

Figure 9.4: Position of the minima observed for sample A as a function of the magnetic field's tilt angle α with respect to the c axis of YBCO. Data are scaled to the magnetic field component parallel to the c axis according to equation 9.1 (symbols). The dashed curve is a different scaling accounting for anisotropy and is not discussed here. Reproduced from Superconductor Science and Technology [59] with permission ©IOP Publishing.

In contrast to measurements on sample B with a lattice constant of $d = 500$ nm the positions of minima are consistent with the modified matching condition for $\alpha \sim 45°$. This value is in agreement with the maximum tilt angle corresponding to the aspect ration of the CDs. At higher tilt angles $\alpha > \alpha_{\max}$, the unconventional critical state gradually breaks down and B_0, B_1, and ΔB decrease below the respective values of $B_\parallel$.

In unirradiated YBCO films, pinning of vortices is mainly caused by twinning and growth defects oriented parallel to the c axis [29]. Angle-dependent measurements show a minimum in magnetoresistance for twin boundaries in a parallel field, extending to about $\alpha \sim 10°$ at half maximum [121]. The measurements on angle dependence of the applied magnetic field don't show any structure in this range of angles neither for sample A nor sample B. We conclude [59] that in our samples additional point defects introduced by stray irradiation into the interstitial regions are present that favor elastic deformation of vortices [21]. Thus, the pinning potential of twin boundaries around $\alpha = 0°$ is reduced, otherwise the additional pinning of twin boundaries would shift the matching peak to higher values at constant bias current.

In conclusion, these measurements confirm the pinning of vortices in ion-irradiated CDs and are consistent with the hysteretic effects of a terrace-like critical state discussed in section 8.2. However, the deviations of angle dependence for samples A and B indicate that vortices are more strongly pinned within the CDs for sample B with 500 nm spacing and form an elastic vortex structure within a single columnar defect, whereas the vortices in sample A with 300 nm spacing might form a kinked vortex structure with neighboring CDs. This would indicate that the irradiation profiles presented in section 5.4 actually are idealized visualizations, since they don't account for a distribution of incident angles due to scattering of ions at the lateral surface of the stencil mask perforations. This scattering might be responsible for a blurring in irradiation of the columnar defect, such that superconductivity is gradually suppressed at a diameter between the idealized 180 nm and below 300 nm. This would account for a stronger suppression of unirradiated superconducting channels between the irradiated CDs for smaller spacing.

This could be further investigated by determining the amount of hysteresis depending on lattice spacing. Furthermore, the angle dependency might be temperature dependent in the sense that sample A might also be consistent with the matching condition above the locking angle of $\alpha \sim 45°$ at lower temperatures, when the difference in spatial modulation of T_c suppression is increased.

10 Conclusion and Outlook

In this thesis, stable non-equilibrium critical states in nanostructured $YBa_2Cu_3O_{7-\delta}$ thin films were investigated by measuring the critical current dependency on applied magnetic fields in field-cooled down-ramped experiments for several initial equilibrium vortex arrangements. An adapted generalized critical state model was used to determine peak positions in critical current data [62, 116]. Peaks of critical current due to matching of commensurate vortex arrangement within an irradiated CDA appear prior to their corresponding matching condition for field-cooled equilibrium vortex distribution, both for ZFC up-ramped and FC down-ramped measurements. This is due to the local magnetic field strongly exceeding the mean magnetic field inside the superconductor due to demagnetization effects in the outermost domain [115].

However, the difference in position of shifted peaks in critical current corresponds to the matching condition. This is shown to be consistent with predictions of a terraced critical state model [117], implying domains of constant occupation number of vortices in CDs. The critical current is determined in the outermost domain on the edge of the superconductor by mobile interstitial vortices, which are strongly pinned within the CDs for commensurate arrangement.

Hysteresis in critical current and magnetoresistance measurements upon ramping the magnetic field can be interpreted by contributions of strongly pinned vortices by CDs and weakly bound interstitial vortices [58]. The angle dependence of minima in magnetoresistance was investigated to determine whether indeed irradiated CDs are responsible for the strong pinning of vortices. The matching condition upon tilting the magnetic field is modified, such that the parallel component of the applied magnetic field with respect to the sample's c axis must reach the matching field of the unmodified condition. For intrinsic twin boundary pinning, deviations from the matching condition are known to occur below 10 to 30° [26, 30, 31, 121]. Investigations on a CDA of 180 nm diameter and 300 nm lattice spacing show that the matching condition is fulfilled up to a locking angle of about 45°, which is consistent with the aspect ratio of the CDs [59]. In this thesis, a CDA of 500 nm lattice spacing was investigated, which shows consistent matching up to a locking angle of 80°, thus, strongly exceeding the locking angle suggested by the aspect ratio. The difference in locking angles upon tilted magnetic field suggest that CDs are surrounded by continuous unsuppressed high T_c channels in the sample with 500 nm lattice spacing, whereas there might be overlapping areas of broadened T_c suppression - caused by stray irradiation of scattered ions within the stencil mask - for the 300 nm lattice spacing, allowing for the occurrence of kinked vortex structures between CDs.

From the observation that angle-dependent pinning at the CDA follows the expected scaling according to equation 9.1 as long as $\alpha < \alpha_{\max}$, the absence of a narrow pinning peak around $\alpha = 0°$ due to pinning at twin boundaries, and the fact that the hysteresis is almost vanishing in the strong intrinsic pinning situation at $\alpha = 90°$ in YBCO we conclude that the pronounced hysteresis of $R(B_a)$ is caused

by pinning of vortices by the CDA and not by a pinning mechanism specific to the unirradiated parts of the sample.[1]

The position of minima in magnetoresistance measurements was determined by fitting a parabolic baseline and inverting the sign of the residual data, such that the adapted generalized critical state model could be also applied to determine the inverted minima. However, future experiments should investigate the angle dependence of applied magnetic field on magnetoresistance at a temperature yielding the same resistance at higher magnetic fields, to serve as actual baseline to the magnetoresistance data of the irradiated sample.

Furthermore, a fundamental question on the interpretation of fit parameters is still open to discussion. Assuming β is associated to the pinning strength of the nanostructured sample, its value might increase - the corresponding pinning strength thus decreases - for matching peaks of higher order, due to lower pinning potential of CDs with higher occupation number. This investigation could reveal information on the influence on occupation number of CDs.

Numerical simulations on irradiation of a $YBa_2Cu_3O_{7-\delta}$ thin film of 210 nm thickness with 75 keV and 30 keV He^+ ions were performed. Single ion trajectories and their respective collision cascades were distributed, first, uniformly across an area corresponding to holes in the Si stencil mask of 180 nm diameter and, second, according to a lateral Gaussian beam distribution of 27 nm FWHM - both corresponding to a fluence of 3×10^{15} cm^{-2}. 3D profiles of T_c suppression were obtained by applying an experimentally calibrated pair-breaking fitting function for the reduction of the critical temperature on simulated defect density data.

75 keV He^+ ion irradiation creates continuous CDs of consistent T_c suppression with insignificant implantation of He atoms at a thickness of 210 nm. He^+ ion irradiation with kinetic energy of 30 keV and lateral Gaussian beam distribution creates CDs up to a thickness of 80 nm, whereas superconductivity is only slightly suppressed below.

The parameters used for the simulation show a relative increase in displacements of oxygen atoms with respect to their abundance. Further investigations might focus on the energy distribution of primary knock-on atoms, to find out whether this relative increase of oxygen displacements mostly occurs in primary ion collisions, or towards the end of defect cascades - as a result of their low displacement energy - where the kinetic energy might not be sufficient anymore to displace tighter bound atoms. Furthermore, a way to distinguish between displacements of chain and plane oxygen atoms should tried to be found.

In conclusion, this thesis provides new insights on stable non-equilibrium vortex arrangements, which represent stored information in its defined vortex states. Vortex motion and, thus, its states can be manipulated using anisotropic shapes of columnar defects upon electronic excitation, such as guides, ratchets or valves [122–126]. The transition between stable states resembles a computation, which is a crucial prerequisite for technological applications of fluxon-bit computing in superconducting electronics [127], enabling high clock speeds at low dissipation [128].

[1] This paragraph is reproduced from [59].

Appendix

A Sample Pictures

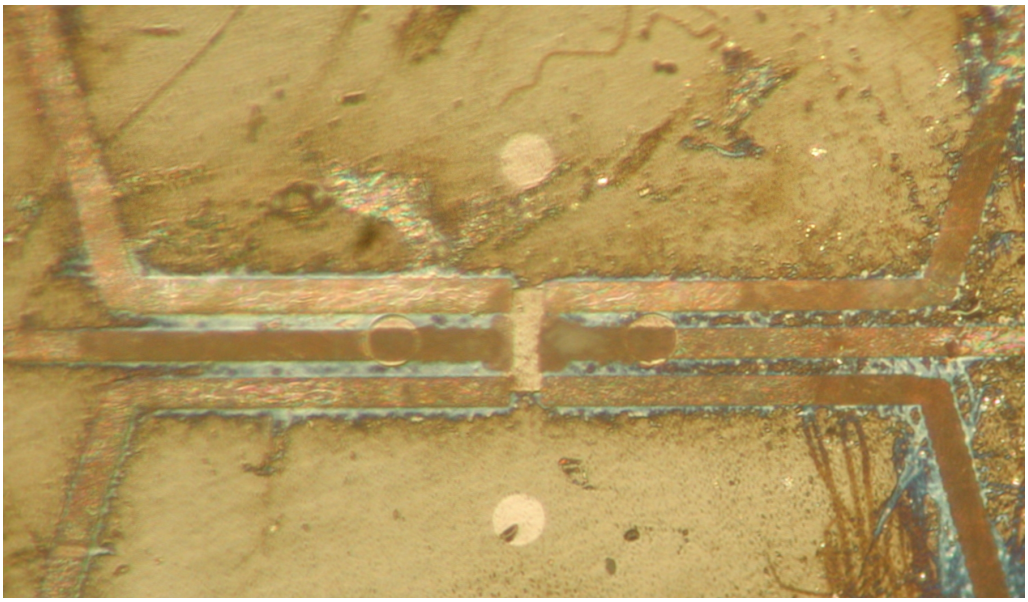

Figure A.1: Sample A under opticle microscope under a specific reflecting angle.

B $T_{c\text{-onset}}$ for 3×10^{15} cm^{-2}

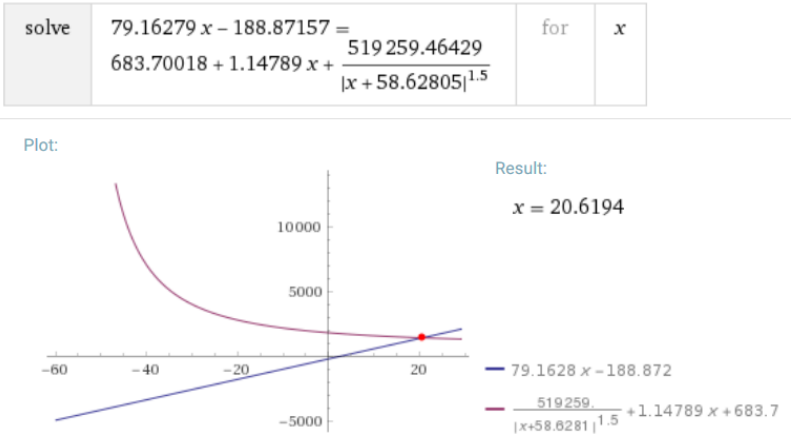

Figure B.1: T_c for 3×10^{15} cm^{-2} was calculated using *WolframAlpha*[100].

C Programs for Data Processing

```c
#include <stdio.h>
#include <string.h>
#include <math.h>
#include <stdlib.h.>
/** fluence.c **/
/*Before starting the program make sure, that the TRANSMIT.txt file has an End Of File (EOF). SRIM tends to
cut of last row! The program substitute all commas with points of the TRANSMIT.txt files computed by SRIM
for several depths [and "³" with spaces - this may be different for the font Newline favored by SRIM]. Then
the replaced file is searched for the string "(Z)", which is the last line before the actual data. Next
each line is read in and stored in the input[] array. The y, z, positions are randomly displaced indepen-
dently inside the given mask-opening of 180nm diameter. The random seed is set to the same value after each
file - since also the ions in TRANSMIT.txt file are computed with same seed for each depth - they are
correlated! Ions, which end up outside the cell, are folded inside the cell on the opposite side. The
number of ions inside a square cell of 2nm length is counted, normalized to the entity e15/cm^2 and written
into the FLUENCE.txt file with the appropriate format for gnuplot pm3d.*/
float ioncount[7][151][151]={0};
float yplus, zplus;
void filecopy(char *pdat, char *pneu);
void randnum();
float foldback(float coordinate);

int main()
{
    int i, condition, nofions;
    int o, p, q;    //indices of defectmatrix
    //depths for which the TRANSMIT.txt data was computed
    int depth[7] = {20, 200, 500, 1000, 1500, 1800, 2000};
    float input[6];
    float fluence;
    float x, y, z;  //ion position
    char filename[130], *pfilename=&filename[0];
    char modfilename[130], *pmodfilename=&modfilename[0]; //decimal commas converted to points
    char depthstring[8], find_breakcond[4];
    char textrow[130], stringcomp[130];
    char *found_it, *pstringcomp;
    FILE *fp, *modfp;

    //for each depth
    for(i=0; i<=6; i++)
    {
    //the TRANSMIT file is opened
    sprintf(depthstring, "%d", depth[i]);
    strcpy(filename, "TRANSMIT_");
    strcat(filename, depthstring);
    strcat(filename, "A.txt");
    fp=fopen(filename, "r");
    //the decimal points file is opened
    strcpy(modfilename, "TRANSMIT_decpoints_");
    strcat(modfilename, depthstring);
    strcat(modfilename, "A.txt");
    //the TRANSMIT file is replaced: commas with points, "³" with spaces.
    modfp=fopen(modfilename, "w");
    filecopy(pfilename, pmodfilename);
    fclose(modfp);
    fclose(fp);
    //the modified file is reopened for reading
    modfp=fopen(modfilename, "r");
    //initialization for each depth
    condition=1;        //checks for breaking condition
    nofions=0;  //prints the total number of ions at given depth on the shell
    srand(1);   //resets the random seed for each depth
    snprintf(find_breakcond,4, "(Z)");  //break-condition is set
    fgets(textrow, sizeof(textrow), modfp);

    while(textrow[0]!=EOF)
    {
```

```
 67          if (condition!=0)
 68          {
 69              //searches for END of header lines
 70              fgets(textrow, sizeof(textrow), modfp);
 71              pstringcomp= strstr(textrow, find_breakcond);
 72              snprintf(stringcomp, 130, "%s", pstringcomp);
 73              condition=strncmp(find_breakcond, stringcomp, 2);
 74          }
 75
 76          if (condition==0)
 77          {
 78              //reads in the ion coordinates
 79              fgets(textrow, sizeof(textrow), modfp);
 80              sscanf(textrow, "%f %f %f %f %f %f", &input[0], &input[1], &input[2], &input[3], &input[4], &
input[5]);
 81              nofions=nofions+1;
 82              y=input[4];
 83              z=input[5];
 84              //random distribution of y and z coordinates
 85              randnum();
 86              y=y+yplus;
 87              z=z+zplus;
 88              //folding back coordinates from neighboring elementary cells
 89              y=foldback(y);
 90              z=foldback(z);
 91               //calculates index corresponding to coordinate
 92              p=floor(150.*(y+1510.)/3020.);
 93              if(p>150)
 94              {
 95                  p=150;
 96              }
 97              q=floor(150.*(z+1510.)/3020.);
 98              if(q>150)
 99              {
100                  q=150;
101              }
102              //counts the number of ions inside 4nm^2 cell
103              ioncount[i][p][q]=ioncount[i][p][q]+1;
104          }
105      }
106      printf("The total number of ions in depth %s is: %d \n", depthstring, nofions);
107      fclose(modfp);
108
109      //Output the normalized fluence to FLUENCE.txt
110      sprintf(depthstring, "%d", depth[i]);
111      strcpy(filename, "FLUENCE_");
112      strcat(filename, depthstring);
113      strcat(filename, "A.txt");
114      fp=fopen(filename, "w");
115
116      for(p=0; p<=150; p++)
117      {
118          for(q=0; q<=150; q++)
119          {
120              //There are 120 ions per 4nm^2 at 3e15/cm^2 fluence.
121              //Times 3 to convert from entity 3e15/cm^2 to e15/cm^2
122              fluence=3.*ioncount[i][p][q]/120.;
123              x=depth[i]/10.;
124              fprintf(fp, "%f %f %f %e\n", x, ((p-75.)*151./75.), (q-75.)*151./75., fluence);
125          }
126              fprintf(fp, "\n"); //needed for gnuplot structure
127      }
128      fclose(fp);
129      printf("%s successfully saved. \n", filename);
130      }
131  }
```

```c
/*****************************************************
##1## Copying datafile substituting commas by points
*****************************************************/
//This function was originally written by Bernd Aichner.
void filecopy(char *pdat, char *pneu)
{
    FILE *altesfile;
    FILE *neuesfile;
    char zeichen;

    altesfile=fopen(pdat, "r");
    // ! Logical NOT. True only if the operand is 0. If c = 5 then, expression ! (c == 5) equals to 0.
    if(!altesfile)
    {
        printf("Fehler beim Öffnen der Datei %s!", *pdat);
    }
    neuesfile=fopen(pneu, "w");

    do
    {
        //The fgetc function returns the character read.
        //If an error occurs, the fgetc function will set the stream's error indicator and return EOF.
        //If the fgetc function encounters the end of stream, it will set the stream's end-of-file
        //indicator and return EOF.
        zeichen=fgetc(altesfile);
        if(zeichen==',')
        {
            zeichen='.';
        }
        if(zeichen=='³')
        {
            zeichen=' ';
        }
        if(zeichen=='T')
        {
            zeichen=' ';
        }
        fputc(zeichen, neuesfile);
    }
    while(zeichen!=EOF);
fclose(altesfile);
fclose(neuesfile);
}
```

```
/*********************************************
##2## Creating random numbers for radial offset of each ion coordinate
*********************************************/
void randnum()
{
    int accept, sign;
    float radius;

    accept=0;
    while(accept==0)
    {
        //yplus
        sign = 0+(rand() % (1000));
        yplus= 0+(rand() % (900)); //900 Angstroem is the radius of the defect channel.
        if(sign<500)
        {
            yplus=-yplus;
        }
        //zplus
        sign = 0+(rand() % (1000)); //independent sign calculation
        zplus= 0+(rand() % (900));
        if(sign<500)
        {
            zplus=-zplus;
        }
        radius=sqrt(yplus*yplus+zplus*zplus);
        if(radius<(900))
        {
        accept=1;
        }
    }
}

/*********************************************
##3## Folding back coordinates from ions in neighboring elementary cells
*********************************************/
float foldback(float coordinate)
{
    while(fabs(coordinate)/1510>1)
    {
        if(coordinate>0)
        {
            coordinate=-(3020-coordinate);
        }
        else if (coordinate<0)
        {
            coordinate=3020+coordinate;
        }
    }
    return coordinate;
}
```

```c
#include <stdio.h>
#include <string.h>
#include <math.h>
#include <time.h>
#include <stdlib.h.>
/** 3D_defect_distribution.c **/
/*
This main program reads out the defect coordinates from the COLLISION.txt file, shifts them
randomly according to a uniform distribution and counts the total  number of defects per
8nm^3 as well as for each element separately. First, the COLLISION.txt file needs to be
converted from decimal comma to point style once. The defined variable LENGTH defines
the number of allocatable defects per ion. It might have to be adapted if the SRIM
simulation settings are altered. A 3D defect-matrix containing x,y,z coordinates
and the corresponding number of defects per 8nm^3 is exported.

This program is loosely based on a program by Bernd Aichner.
It has to be noted, that this program should be improved by reducing the number of global variables.
Furthermore, the reading in process should be possible without the use of the input array of
defined LENGTH, by subsequently reading in and storing data with the same random shift.*/


#define LENGTH 2200 // ->Pro Ion darf es maximal so viele Datenzeilen geben!
//global variables
    int n;
    float yplus, zplus;
    float koord[LENGTH][8];
    float defects[105][151][151][5]={0};
    char colname[150]={"COLLISON.txt"}, *pcolname=&colname[0];
    char modname[150]={"COLLISON_decimalpoint.txt"}, *pmodname=&modname[0];

//function prototypes
    void initialize(FILE *datafile);
    void search_maximum_lines_per_ion(FILE *datafile);
    void filecopy(char *pdat, char *pneu);
    void readcol(int k, FILE *datafile);
    void randnum();
    float foldback(float coordinate);
    int get_element_index(int index);
    void output_defectmatrix(float defects[105][151][151][5]);

/*****************************************************
SRIM-based Ion-distribution-calculation
##0## Main Program
*****************************************************/
int main()
{
    int k, i, j; //k...Zählindex für Ionen, i...Zählindex für die Positionen des k-ten Ions
    int ind, vacancies=0;  //Ordnungszahl des Elements
    int o,p,q; //indices of defect matrix
    float x,y,z; //coordinates
    FILE *datafile;

    n=763407;
    // Initializiation allows for change in n, calling of filecopy and an estimate for LENGTH.
    initialize(datafile);
    datafile=fopen(modname, "r");

    for(k=1; k<=n; k++)
    {
        //readcol reads in all defect coordinates of all recoil cascades for one ion
        readcol(k, datafile);
        //Draw a random radial position offset for each ion. All defect-coordinates affected.
        randnum();
        for(i=0;i<LENGTH;i++)
        {
            if(koord[i][0]!=-1)
```

```
            {
            x=koord[i][3];
            y=koord[i][4];
            z=koord[i][5];

            y=y+yplus;
            z=z+zplus;

            //folding back coordinates from neighboring elementary cells
            y=foldback(y);
            z=foldback(z);

            //mapping from unit cell to array
            o=floor(105.*x/2100.);
            if(o>104)
            {
                o=104;
            }
            p=floor(150.*(y+1510.)/3020.);
            if(p>150)
            {
                p=150;
            }
            q=floor(150.*(z+1510.)/3020.);
            if(q>150)
            {
                q=150;
            }
            ind=get_element_index(koord[i][1]);

                if(koord[i][6]==1) //is not true for replacements
                {
                    //number of defects per element defined in ind
                    defects[o][p][q][ind]=defects[o][p][q][ind]+1;
                    //total number of defects
                    defects[o][p][q][4]=defects[o][p][q][4]+1;
                    vacancies=vacancies+1;
                }
            }
        }
    }
    printf("%d vacancies. \n", vacancies);
    printf("Printing matrices...\n");
    output_defectmatrix(defects);
    fclose(modname);
}
```

```
/*********************************************
#### Reading out the collision cascades for one ion
*********************************************/
void readcol(int k, FILE *datafile)
{
    char textrow[130];
    char find_ion[8], find_cascades[8], find_breakcond[21];
    char *found_it;
    char *pstringcomp;
    char stringcomp[130];
    int i,j, l=1, v, statistics=1; //i...Zeilenindex, l...Nummerierung der Recoils

    for(i=0;i<LENGTH;i++)
    {
        koord[i][0]=-1;
    }

    i=0;
    found_it=0;
    v=1;
    snprintf(find_breakcond,21, "For All Ions to date");

    while(v!=0)
    {
        //The fgets function reads characters from the stream pointed to by stream.
        //It will stop reading when n-1 characters are read,
        //the first new-line character is encountered in s,
        //or at the end-of-file, whichever comes first.
        //Then the fgets function will append a null character to the string.
        fgets(textrow, sizeof(textrow), datafile);

        //The strstr function searches within the string pointed to by s1 for the string pointed to by s2.
        //It returns a pointer to the first occurrence in s1 of s2.
        pstringcomp= strstr(textrow, find_breakcond);
        snprintf(stringcomp, 130, "%s", pstringcomp);
        v=strncmp(find_breakcond, stringcomp, 20);

        if (v==0 && k==763406)
        {
            printf("Found statistics:\n");
            printf("%s", textrow);
            statistics=1;
            for (j=1;j<=6;j++)
            {
                fgets(textrow, sizeof(textrow), datafile);
                printf("%s", textrow);
            }
        }

        if (v==0 && fmod(k, 5000)==0)
        {
            printf("All cascades up to ion: %d \n", k);
        }

        //Integer nach Leerzeichen in 5 Zeichen langen String verwandeln,
        //der von vorn mit Nullen aufgefüllt wird.
        snprintf(find_ion,8, " %05d=", k);
        found_it=strstr(textrow,find_ion); //found_it ist jetzt: " 0000k=\n"

        if(found_it!=0)
        {
        //In this if-case we are inside a collision cascade, at the end of the last ion data line.
        //We have to search for target atoms of this collision in a loop
        //and read out the defect coordinates and the corresponding element.
        //printf("%s\n", find_ion);
            while(found_it!=0)
```

```
            {
                fgets(textrow, sizeof(textrow), datafile);
                snprintf(find_cascades,8, "Û %05d", l);
                found_it=strstr(textrow,find_cascades);
                sscanf(textrow, "Û %f %f %f %f %f %f %f %f Û", &koord[i][0], &koord[i][1], &koord[i][2], &
koord[i][3], &koord[i][4], &koord[i][5], &koord[i][6], &koord[i][7]);
                //printf("%f, %f, %f, %f, %f, %f, %f, %f \n", koord[i][0], koord[i][1], koord[i][2],
koord[i][3], koord[i][4], koord[i][5], koord[i][6], koord[i][7]);
                l++;
                i++;
            }
            l=1;
        }
    }
}


/***********************************************
##8## Convert the element's atomic number to the corresponding index
***********************************************/
int get_element_index(int index)
{
    if(index==39)
    {
        index=0;
    }
    else if(index==56)
    {
        index=1;
    }
    else if(index==29)
    {
        index=2;
    }
    else
    {
        index=3;
    }
    return index;
}
```

```
/*********************************************
##6## Creating files for defect-matrices at given depth
*********************************************/
void output_defectmatrix(float defects[105][151][151][5])
{
    char spaceholder[3];
    int i, o, p, q;
    char filename[130];
    FILE *fp;

    for(i=0; i<=3; i++)
    {
    sprintf(spaceholder, "%d", i);
    strcpy(filename, "defectmatrix_x_y_z_fxyz_");
    strcat(filename, spaceholder);
    strcat(filename, ".txt");

    fp=fopen(filename, "w");
    for(o=0; o<=104; o++)
    {
        for(p=0; p<=150; p++)
        {
            for(q=0; q<=150; q++)
            {   // x and y +. 151nm
                fprintf(fp, "%f %f %f %f\n", o*2., ((p-75.)*151./75.), (q-75.)*151./75., defects[o][p][q][i
]);

            }
        }
    }
    fclose(fp);
    printf("%s created succesfully. \n", filename);
    }

    strcpy(filename, "defectmatrix_x_y_z_fxyz_CuO.txt");
    fp=fopen(filename, "w");
    for(o=0; o<=104; o++)
    {
        for(p=0; p<=150; p++)
        {
            for(q=0; q<=150; q++)
            {   // x and y +. 151nm
                fprintf(fp, "%f %f %f %f\n", o*2., ((p-75.)*151./75.), (q-75.)*151./75., defects[o][p][q][2
]+defects[o][p][q][3]);
            }
        }
    }
    fclose(fp);
    printf("%s created succesfully. \n", filename);

    strcpy(filename, "defectmatrix_x_y_z_fxyz.txt");
    fp=fopen(filename, "w");
    for(o=0; o<=104; o++)
    {
        for(p=0; p<=150; p++)
        {
            for(q=0; q<=150; q++)
            {   // x and y +. 151nm
                fprintf(fp, "%f %f %f %f\n", o*2., ((p-75.)*151./75.), (q-75.)*151./75., defects[o][p][q][4
]);

            }
        }
    }
    fclose(fp);
    printf("%s created succesfully. \n", filename);
}
```

```c
#include <stdio.h>
#include <string.h>
#include <math.h>
#include <stdlib.h.>
/** fluence-HIM.c **/
/*For explanation look at fluence.c. Here only differences are discussed.
This probe has a lattice constant of defect channels of 200nm. Its diameter is determined by the FWHM,
of the Gaussian distribution for the ion beam, which is used in the randnum() function.
The Gaussian distribution of random numbers is obtained by the accept-reject method.
The overall number of ions is 50639, corresponding to fluence of 3e15/cm^2 if the beam diameter is
about 25nm. Experimentally, the number of ions is determined by the voltage on the HIM-tip. */

float ioncount[7][101][101]={0};
float yplus, zplus, FWHM;
float foldback(float coordinate);
void filecopy(char *pdat, char *pneu);
void randnum();

int main()
{
    int i, o, p, q, v, nofions;
    int depth[5] = {20, 500, 1000, 1500, 2000};
    float input[6];
    float x, y, z, fluence;
    char filename[130], *pfilename=&filename[0];
    char modfilename[130], *pmodfilename=&modfilename[0];
    char depthstring[8], find_breakcond[4];
    char textrow[130], stringcomp[130];
    char *found_it, *pstringcomp;
    FILE *fp, *modfp;

    FWHM=270.;

    for(i=0; i<=4; i++)
    {
    sprintf(depthstring, "%d", depth[i]);
    strcpy(filename, "TRANSMIT_HIM_");
    strcat(filename, depthstring);
    strcat(filename, "A.txt");
    fp=fopen(filename, "r");

    strcpy(modfilename, "TRANSMIT_HIM_decpoints_");
    strcat(modfilename, depthstring);
    strcat(modfilename, "A.txt");

    modfp=fopen(modfilename, "w");
    filecopy(pfilename, pmodfilename);
    fclose(modfp);
    fclose(fp);

    modfp=fopen(modfilename, "r");
    v=1;
    nofions=0;
    srand(1);

    snprintf(find_breakcond,4, "(Z)");
    fgets(textrow, sizeof(textrow), modfp);

    while(textrow[0]!=EOF)
    {
        if (v!=0)
        {
            fgets(textrow, sizeof(textrow), modfp);
            pstringcomp= strstr(textrow, find_breakcond);
            snprintf(stringcomp, 130, "%s", pstringcomp);
            v=strncmp(find_breakcond, stringcomp, 2);
```

```
 67          }
 68
 69          if (v==0)
 70          {
 71              fgets(textrow, sizeof(textrow), modfp);
 72              sscanf(textrow, "%f %f %f %f %f %f", &input[0], &input[1], &input[2], &input[3], &input[4], &
input[5]);
 73              y=input[4];
 74              z=input[5];
 75              randnum();
 76              y=y+yplus;
 77              z=z+zplus;
 78              y=foldback(y);
 79              z=foldback(z);
 80              p=floor(100.*(y+1000.)/2000.);
 81              if(p>100)
 82              {
 83                  p=100;
 84              }
 85              q=floor(100.*(z+1000.)/2000.);
 86              if(q>100)
 87              {
 88                  q=100;
 89              }
 90              ioncount[i][p][q]=ioncount[i][p][q]+1;
 91              nofions=nofions+1;
 92          }
 93      }
 94      printf("The total number of ions in depth %s is: %d \n", depthstring, nofions);
 95      fclose(modfp);
 96
 97      //Output
 98      sprintf(depthstring, "%d", depth[i]);
 99      strcpy(filename, "FLUENCE_HIM_");
100      strcat(filename, depthstring);
101      strcat(filename, "A.txt");
102      fp=fopen(filename, "w");
103
104       for(p=0; p<=100; p++)
105       {
106          for(q=0; q<=100; q++)
107          {
108              fluence=3*ioncount[i][p][q]/120.;
109              x=depth[i]/10.;
110              fprintf(fp, "%f %f %f %e\n", x, ((p-50.)*100./50.), (q-50.)*100./50., fluence);
111          }
112              fprintf(fp, "\n"); //needed for gnuplot structure
113      }
114      fclose(fp);
115      printf("%s opened succesfully. \n", filename);
116      }
117   }
118
119
120
121
122
123
124
125
126
127
128
129
130
131
```

```
/*********************************************
##2## Creating random numbers for Gaussian distribution of the ion beam
*********************************************/
void randnum()
{
    int accept, sign;
    float gauss, sigma, random_z;

    accept=0;
    sigma=FWHM/2.4;
    while(accept==0)
    {
        sign = 0+(rand() % (1000));
        yplus= (0+(rand() % (10000)))/10.;
        if(sign<500)
        {
            yplus=-yplus;
        }
        sign = 0+(rand() % (1000));
        zplus= (0+(rand() % (10000)))/10.;
        if(sign<500)
        {
            zplus=-zplus;
        }
        //accept/reject
        gauss=exp(-(yplus*yplus+zplus*zplus)/(2*sigma*sigma));
        random_z=(0+(rand() % (100000)))/100000.;
        if(random_z<gauss)
        {
        accept=1;
        }
    }
}

/*********************************************
##3## Folding back coordinates from ions in neighboring elementary cells
*********************************************/
float foldback(float coordinate)
{
    while(fabs(coordinate)/1000>1)
    {
        if(coordinate>0)
        {
            coordinate=-(2000-coordinate);
        }
        else if (coordinate<0)
        {
            coordinate=2000+coordinate;
        }
    }
    return coordinate;
}
```

D Field-Cooled Ramped I_c Multi-Peak Fits

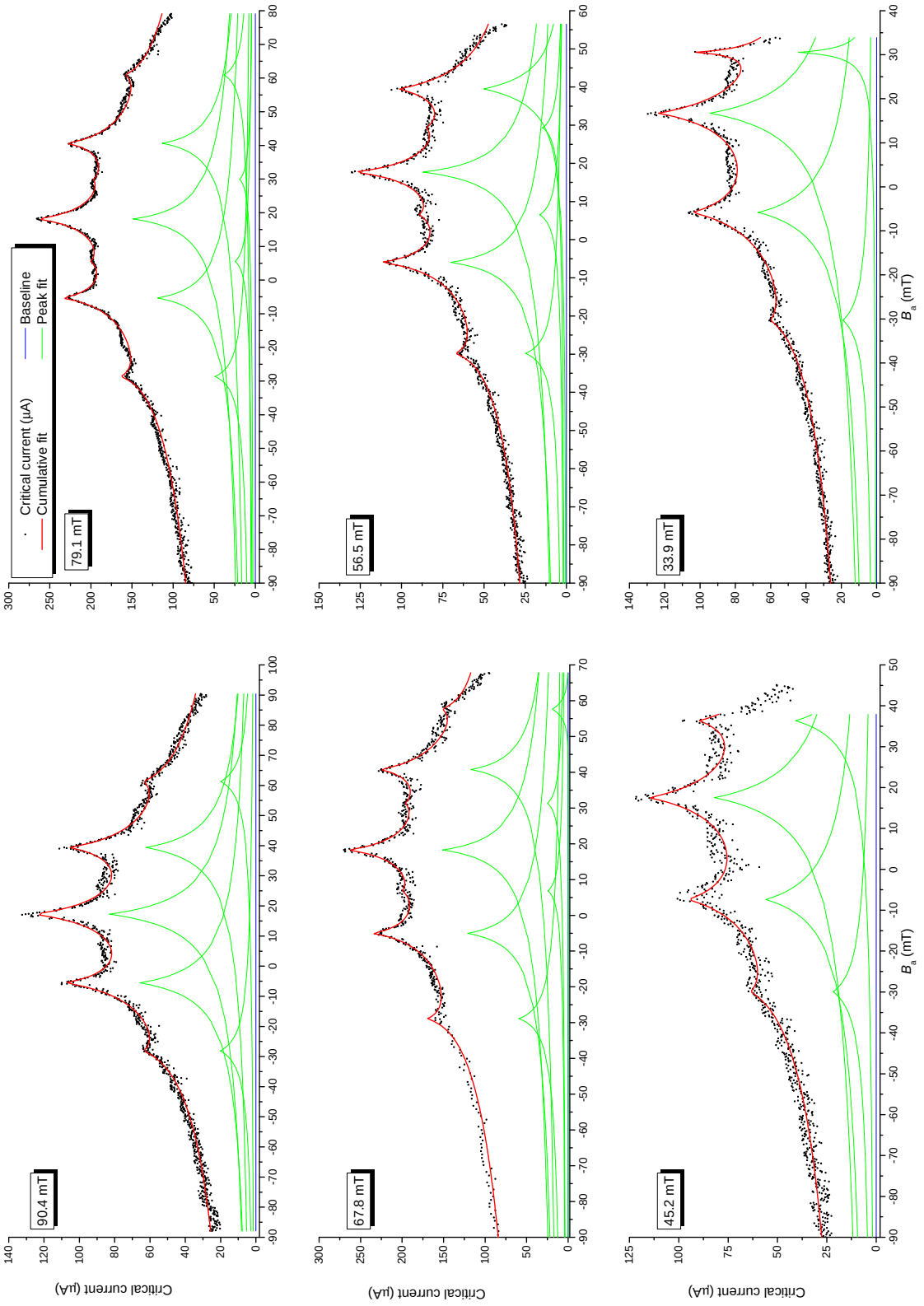

Figure D.1: Field-cooled ramped I_c multi-peak fits

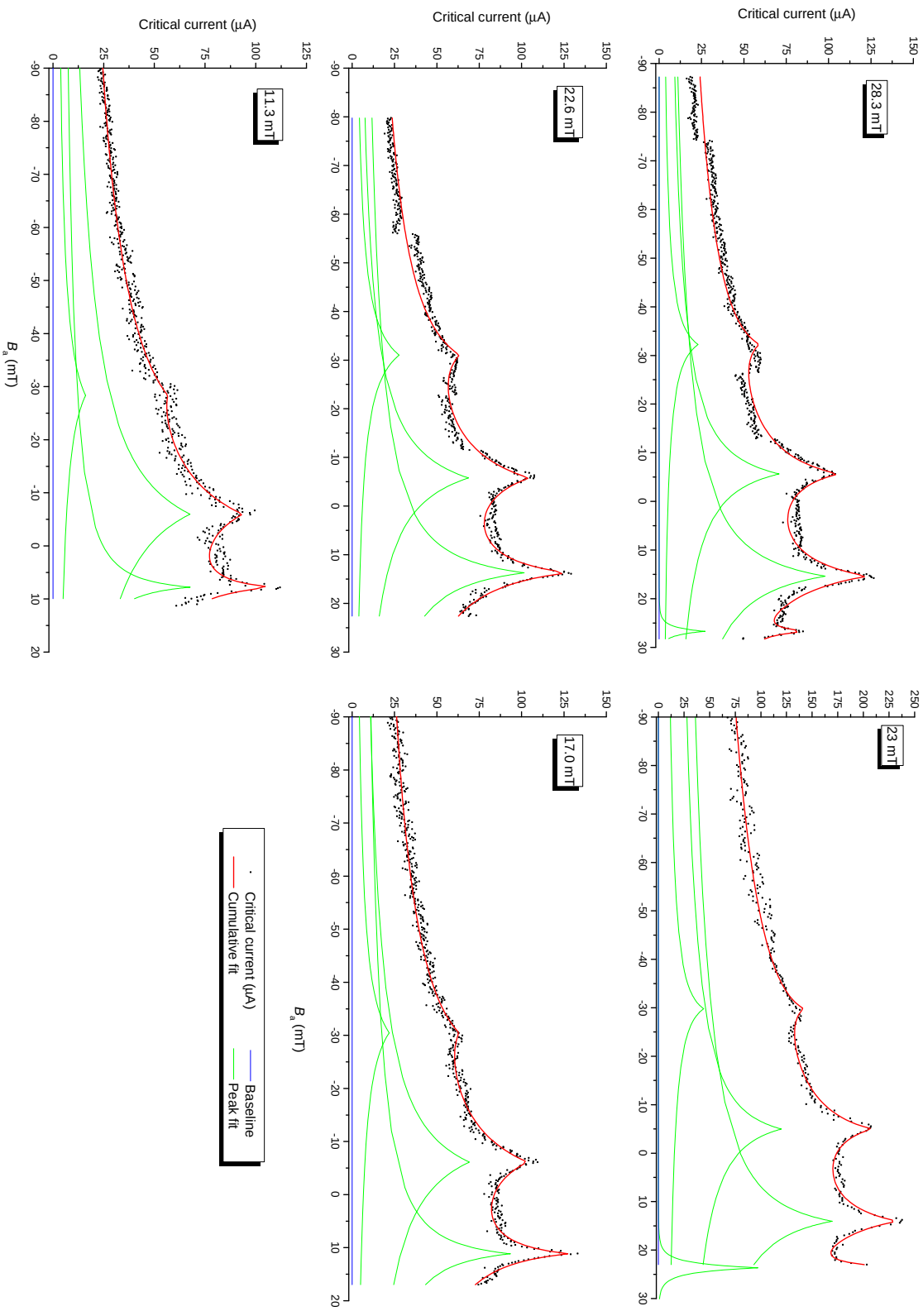

Figure D.2: Field-cooled ramped I_c multi-peak fits

E Angle Dependence of Magnetoresistance Multi-Peak Fits

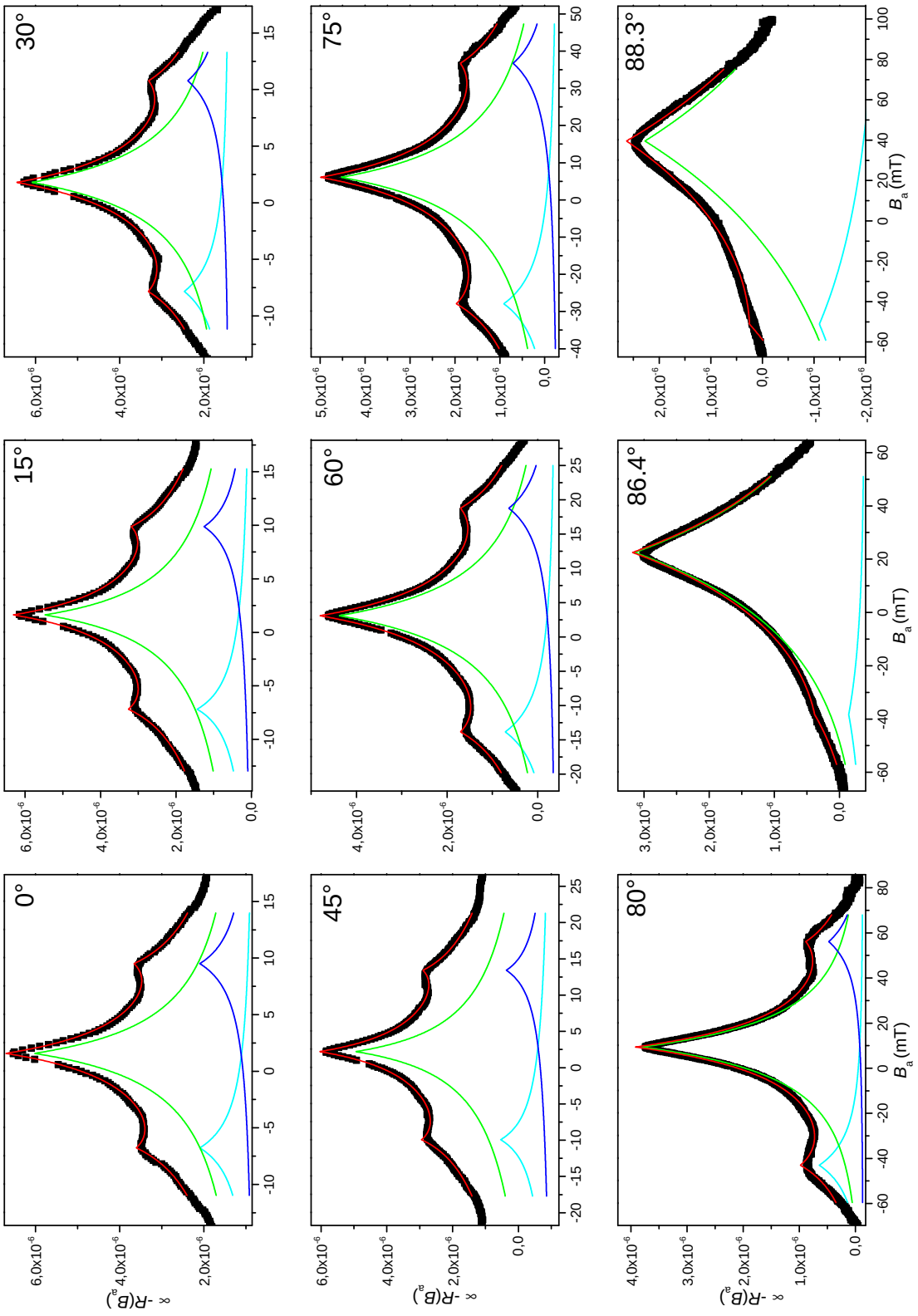

Figure E.1: $R(B, \alpha)$ down-sweep multi-peak fits

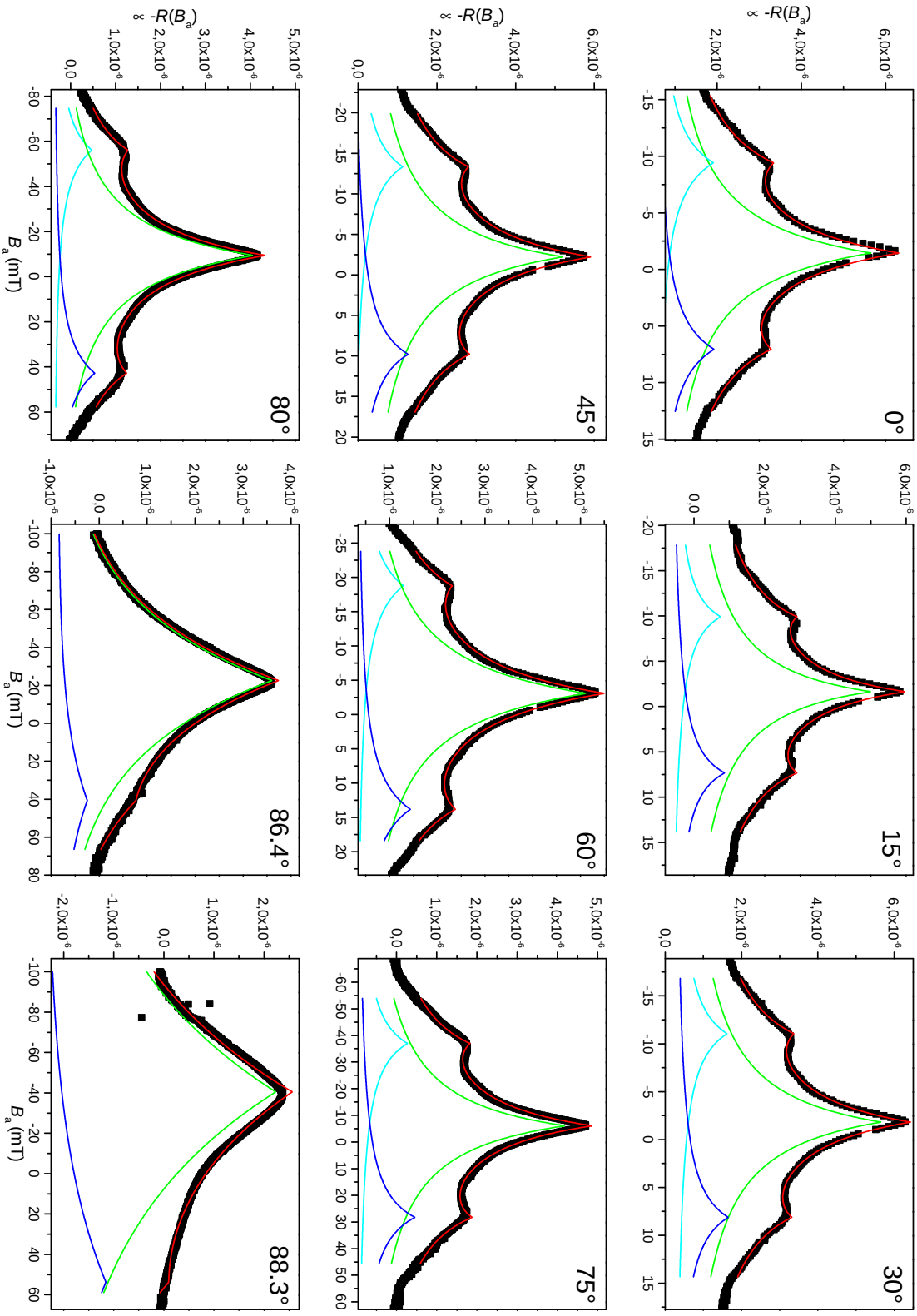

Figure E.2: $R(B, \alpha)$ up-sweep multi-peak fits

List of Figures

List of Tables

Bibliography

[1] Kamerlingh Onnes, H. "The resistance of pure mercury at helium temperatures". In: *Commun. Phys. Lab. Univ. Leiden, b* 120 (1911).

[2] Bloch, F. "Über die Quantenmechanik der Elektronen in Kristallgittern". In: *Zeitschrift für Physik* 52.7-8 (1929), pp. 555–600. DOI: 10.1007/bf01339455.

[3] Meissner, W. and Ochsenfeld, R. "Ein neuer Effekt bei Eintritt der Supraleitfähigkeit". In: *Die Naturwissenschaften* 21.44 (1933), pp. 787–788. DOI: 10.1007/bf01504252.

[4] Quinn, D. J. and Ittner, W. B. "Resistance in a Superconductor". In: *Journal of Applied Physics* 33.2 (1962), pp. 748–749. DOI: 10.1063/1.1702504.

[5] Bednorz, J. G. and Müller, K. A. "Possible high T_c superconductivity in the Ba-La-Cu-O system". In: *Zeitschrift für Physik B Condensed Matter* 64.2 (1986), pp. 189–193. DOI: 10.1007/bf01303701.

[6] Wu, M. K., Ashburn, J. R., Torng, C. J., Hor, P. H., Meng, R. L., Gao, L., Huang, Z. J., Wang, Y. Q., and Chu, C. W. "Superconductivity at 93 K in a new mixed-phase Y-Ba-Cu-O compound system at ambient pressure". In: *Physical Review Letters* 58.9 (1987), pp. 908–910. DOI: 10.1103/physrevlett.58.908.

[7] London, F. and London, H. "The Electromagnetic Equations of the Supraconductor". In: *Proceedings of the Royal Society A: Mathematical, Physical and Engineering Sciences* 149.866 (1935), pp. 71–88. DOI: 10.1098/rspa.1935.0048.

[8] Ginzburg, V. L. and Landau, L. D. "On the Theory of superconductivity". In: *Zh. Eksp. Teor. Fiz.* 20 (1950), pp. 1064–1082.

[9] Bardeen, J., Cooper, L. N., and Schrieffer, J. R. "Theory of Superconductivity". In: *Physical Review* 108.5 (1957), pp. 1175–1204. DOI: 10.1103/physrev.108.1175.

[10] Buckel, W. and Kleiner, R. *Supraleitung*. Wiley-VCH Verlag GmbH & Co. KGaA, 2012. DOI: 10.1002/9783527668670.

[11] Gor'kov, L. P. "Microscopic derivation of the Ginzburg-Landau equations in the theory of superconductivity". In: *Sov. Phys. JETP* 9.6 (1959), pp. 1364–1367.

[12] Bulut, N. and Scalapino, D. J. "Weak-coupling model of spin fluctuations in the superconducting state of the layered cuprates". In: *Physical Review B* 45.5 (1992), pp. 2371–2384. DOI: 10.1103/physrevb.45.2371.

[13] Tsuei, C. C., Kirtley, J. R., Chi, C. C., Yu-Jahnes, L. S., Gupta, A., Shaw, T., Sun, J. Z., and Ketchen, M. B. "Pairing Symmetry and Flux Quantization in a Tricrystal Superconducting Ring of $YBa_2Cu_3O_{7-\delta}$". In: *Physical Review Letters* 73.4 (1994), pp. 593–596. DOI: 10.1103/physrevlett.73.593.

[14] Harlingen, D. J. V. "Phase-sensitive tests of the symmetry of the pairing state in the high-temperature superconductors - Evidence for $d_{x^2-y^2}$ symmetry". In: *Reviews of Modern Physics* 67.2 (1995), pp. 515–535. DOI: 10.1103/revmodphys.67.515.

[15] Wesche, R. *Physical Properties of High-Temperature Superconductors*. John Wiley & Sons, Ltd, 2015. DOI: 10.1002/9781118696644.

[16] Abrikosov, A. A. "On the Magnetic Properties of Superconductors of the Second Group". In: *Sov. Phys. JETP* 5.6 (1957), pp. 1174–1182.

[17] Kleiner, R. and Buckel, W. *Superconductivity: Fundamentals and Applications*. Wiley-VCH, 2015. ISBN: 978-3-527-40349-3.

[18] Silsbee, F. B. "A note on electrical conduction in metals at low temperatures". In: *Journal of the Washington Academy of Sciences* 6.17 (1916), pp. 597–602. ISSN: 00430439.

[19] Kwok, W.-K., Welp, U., Glatz, A., Koshelev, A. E., Kihlstrom, K. J., and Crabtree, G. W. "Vortices in high-performance high-temperature superconductors". In: *Reports on Progress in Physics* 79.11 (2016), p. 116501. DOI: 10.1088/0034-4885/79/11/116501.

[20] Fisher, M. P. A. "Vortex-glass superconductivity: A possible new phase in bulk high-T_c oxides". In: *Physical Review Letters* 62.12 (1989), pp. 1415–1418. DOI: 10.1103/physrevlett.62.1415.

[21] Sefrioui, Z., Arias, D., González, E. M., León, C., Santamaria, J., and Vicent, J. L. "Vortex liquid entanglement in irradiated $YBa_2Cu_3O_7$ thin films". In: *Physical Review B* 63.6 (2001). DOI: 10.1103/physrevb.63.064503.

[22] Bardeen, J. and Stephen, M. J. "Theory of the Motion of Vortices in Superconductors". In: *Physical Review* 140.4A (1965), A1197–A1207. DOI: 10.1103/physrev.140.a1197.

[23] Campbell, A. M. and Evetts, J. E. "Flux vortices and transport currents in type II superconductors". In: *Advances in Physics* 21.90 (1972), pp. 199–428. DOI: 10.1080/00018737200101288.

[24] Bean, C. P. and Livingston, J. D. "Surface Barrier in Type-II Superconductors". In: *Physical Review Letters* 12.1 (1964), pp. 14–16. DOI: 10.1103/physrevlett.12.14.

[25] McHenry, M. E. and Sutton, R. A. "Flux pinning and dissipation in high temperature oxide superconductors". In: *Progress in Materials Science* 38 (1994), pp. 159–310. DOI: 10.1016/0079-6425(94)90003-5.

[26] Roas, B., Schultz, L., and Saemann-Ischenko, G. "Anisotropy of the critical current density in epitaxial $YBa_2Cu_3O_x$ films". In: *Physical Review Letters* 64.4 (1990), pp. 479–482. DOI: 10.1103/physrevlett.64.479.

[27] Blatter, G., Feigelman, M. V., Geshkenbein, V. B., Larkin, A. I., and Vinokur, V. M. "Vortices in high-temperature superconductors". In: *Reviews of Modern Physics* 66.4 (1994), pp. 1125–1388. DOI: 10.1103/revmodphys.66.1125.

[28] Tachiki, M. and Takahashi, S. "Strong vortex pinning intrinsic in high-T_c oxide superconductors". In: *Solid State Communications* 70.3 (1989), pp. 291–295. DOI: 10.1016/0038-1098(89)90330-x.

[29] Dam, B., Huijbregtse, J. M., Klaassen, F. C., Geest, R. C. F. van der, Doornbos, G., Rector, J. H., Testa, A. M., Freisem, S., Martinez, J. C., Stäuble-Pümpin, B., and Griessen, R. "Origin of high critical currents in $YBa_2Cu_3O_{7-\delta}$ superconducting thin films". In: *Nature* 399.6735 (1999), pp. 439–442. DOI: 10.1038/20880.

[30] Civale, L., Maiorov, B., Serquis, A., Willis, J. O., Coulter, J. Y., Wang, H., Jia, Q. X., Arendt, P. N., MacManus-Driscoll, J. L., Maley, M. P., and Foltyn, S. R. "Angular-dependent vortex pinning mechanisms in $YBa_2Cu_3O_7$ coated conductors and thin films". In: *Applied Physics Letters* 84.12 (2004), pp. 2121–2123. DOI: 10.1063/1.1655707.

[31] Zhukov, A. A., Perkins, G. K., Thomas, J. V., Caplin, A. D., Küpfer, H., and Wolf, T. "Direct observation of tilted vortex structures induced by twin boundaries in $YBa_2Cu_3O_y$ single crystals". In: *Physical Review B* 56.6 (1997), pp. 3481–3487. DOI: 10.1103/physrevb.56.3481.

[32] Tachiki, M. and Takahashi, S. "Anisotropy of critical current in layered oxide superconductors". In: *Solid State Communications* 72.11 (1989), pp. 1083–1086. DOI: 10.1016/0038-1098(89)90251-2.

[33] Díaz, A., Mechin, L., Berghuis, P., and Evetts, J. E. "Evidence for Vortex Pinning by Dislocations $YBa_2Cu_3O_{7-\delta}$ Low-Angle Grain Boundaries". In: *Physical Review Letters* 80.17 (1998), pp. 3855–3858. DOI: 10.1103/physrevlett.80.3855.

[34] Welp, U., Xiao, Z. L., Jiang, J. S., Vlasko-Vlasov, V. K., Bader, S. D., Crabtree, G. W., Liang, J., Chik, H., and Xu, J. M. "Superconducting transition and vortex pinning in Nb films patterned with nanoscale hole arrays". In: *Physical Review B* 66.21 (2002). DOI: 10.1103/physrevb.66.212507.

[35] Raedts, S., Silhanek, A. V., Bael, M. J. V., and Moshchalkov, V. V. "Flux-pinning properties of superconducting films with arrays of blind holes". In: *Physical Review B* 70.2 (2004). DOI: 10.1103/physrevb.70.024509.

[36] Stoll, O. M., Montero, M. I., Guimpel, J., Åkerman, J. J., and Schuller, I. K. "Hysteresis and fractional matching in thin Nb films with rectangular arrays of nanoscaled magnetic dots". In: *Physical Review B* 65.10 (2002). DOI: 10.1103/physrevb.65.104518.

[37] Ionescu, M., Li, A. H., Zhao, Y., Liu, H. K., and Crisan, A. "Enhancement of critical current density in $YBa_2Cu_3O_7$ thin films grown using PLD on YSZ (001) surface modified with Ag nano-dots". In: *Journal of Physics D: Applied Physics* 37.13 (2004), pp. 1824–1828. DOI: 10.1088/0022-3727/37/13/014.

[38] Civale, L., Marwick, A. D., Worthington, T. K., Kirk, M. A., Thompson, J. R., Krusin-Elbaum, L., Sun, Y., Clem, J. R., and Holtzberg, F. "Vortex confinement by columnar defects in $YBa_2Cu_3O_7$ crystals: Enhanced pinning at high fields and temperatures". In: *Physical Review Letters* 67.5 (1991), pp. 648–651. DOI: 10.1103/physrevlett.67.648.

[39] Holzapfel, B., Kreiselmeyer, G., Kraus, M., Bouffard, S., Klaumünzer, S., Schultz, L., and Saemann-Ischenko, G. "Angle-resolved critical transport-current density of $YBa_2Cu_3O_{7-\delta}$ thin films and $YBa_2Cu_3O_{7-\delta}/PrBa_2Cu_3O_{7-\delta}$ superlattices containing columnar defects of various orientations". In: *Physical Review B* 48.1 (1993), pp. 600–603. DOI: 10.1103/physrevb.48.600.

[40] Takezawa, N. and Fukushima, K. "Optimal size of a cylindrical insulating inclusion acting as a pinning center for magnetic flux in superconductors". In: *Physica C: Superconductivity* 228.1-2 (1994), pp. 149–159. DOI: 10.1016/0921-4534(94)90186-4.

[41] Nordborg, H. and Vinokur, V. M. "Interaction between a vortex and a columnar defect in the London approximation". In: *Physical Review B* 62.18 (2000), pp. 12408–12412. DOI: 10.1103/physrevb.62.12408.

[42] Mkrtchyan, G. S. and Shmidt, V. V. "Interaction Between a Cavity and a Vortex in a Superconductor of the Second Kind". In: *Sov. Phys. JETP* 34 (1972), p. 195.

[43] Doria, M., Andrade, S. de, and Sardella, E. "Maximum number of flux lines inside columnar defects". In: *Physica C: Superconductivity* 341-348 (2000), pp. 1199–1200. DOI: 10.1016/s0921-4534(00)00858-3.

[44] Blamire, M. G. "Flux vortex dynamics and electric fields in matched pinning systems". In: *Journal of Low Temperature Physics* 68.5-6 (1987), pp. 335–352. DOI: 10.1007/bf00682301.

[45] Petermann, J. "Ausscheidungen und Flußverankerung in einer supraleitenden PbNa-Legierung". Georg-August-Universität Göttingen, 1970.

[46] Raffy, H., Renard, J. C., and Guyon, E. "Critical currents and pinning effect in superconducting alloy films spatially modulated in concentration". In: *Solid State Communications* 11.12 (1972), pp. 1679–1682. DOI: 10.1016/0038-1098(72)90770-3.

[47] Daldini, O., Martinoli, P., Olsen, J. L., and Berner, G. "Vortex-Line Pinning by Thickness Modulation of Superconducting Films". In: *Physical Review Letters* 32.5 (1974), pp. 218–221. DOI: 10.1103/physrevlett.32.218.

[48] Fiory, A. T., Hebard, A. F., and Somekh, S. "Critical currents associated with the interaction of commensurate flux-line sublattices in a perforated Al film". In: *Applied Physics Letters* 32.1 (1978), pp. 73–75. DOI: 10.1063/1.89845.

[49] Baert, M., Metlushko, V. V., Jonckheere, R., Moshchalkov, V. V., and Bruynseraede, Y. "Composite Flux-Line Lattices Stabilized in Superconducting Films by a Regular Array of Artificial Defects". In: *Physical Review Letters* 74.16 (1995), pp. 3269–3272. DOI: 10.1103/physrevlett.74.3269.

[50] Martín, J. I., Vélez, M., Nogués, J., and Schuller, I. K. "Flux Pinning in a Superconductor by an Array of Submicrometer Magnetic Dots". In: *Physical Review Letters* 79.10 (1997), pp. 1929–1932. DOI: 10.1103/physrevlett.79.1929.

[51] Castellanos, A., Wördenweber, R., Ockenfuss, G., Hart, A. v.d., and Keck, K. "Preparation of regular arrays of antidots in $YBa_2Cu_3O_7$ thin films and observation of vortex lattice matching effects". In: *Applied Physics Letters* 71.7 (1997), pp. 962–964. DOI: 10.1063/1.119701.

[52] Harada, K., Kamimura, O., Kasai, H., Matsuda, T., Tonomura, A., and Moshchalkov, V. V. "Direct Observation of Vortex Dynamics in Superconducting Films with Regular Arrays of Defects". In: *Science* 274.5290 (1996), pp. 1167–1170. DOI: 10.1126/science.274.5290.1167.

[53] Swiecicki, I., Ulysse, C., Wolf, T., Bernard, R., Bergeal, N., Briatico, J., Faini, G., Lesueur, J., and Villegas, J. E. "Strong field-matching effects in superconducting $YBa_2Cu_3O_{7-\delta}$ films with vortex energy landscapes engineered via masked ion irradiation". In: *Physical Review B* 85.22 (2012). DOI: 10.1103/physrevb.85.224502.

[54] Wördenweber, R., Dymashevski, P., and Misko, V. R. "Guidance of vortices and the vortex ratchet effect in high-T_c superconducting thin films obtained by arrangement of antidots". In: *Physical Review B* 69.18 (2004). DOI: 10.1103/physrevb.69.184504.

[55] Kemmler, M., Gürlich, C., Sterck, A., Pöhler, H., Neuhaus, M., Siegel, M., Kleiner, R., and Koelle, D. "Commensurability Effects in Superconducting Nb Films with Quasiperiodic Pinning Arrays". In: *Physical Review Letters* 97.14 (2006). DOI: 10.1103/physrevlett.97.147003.

[56] Bothner, D., Seidl, R., Misko, V. R., Kleiner, R., Koelle, D., and Kemmler, M. "Unusual commensurability effects in quasiperiodic pinning arrays induced by local inhomogeneities of the pinning site density". In: *Superconductor Science and Technology* 27.6 (2014), p. 065002. DOI: 10.1088/0953-2048/27/6/065002.

[57] Jausner, F. "Kritischer Strom von nanostrukturierten $YBa_2Cu_3O_{7-x}$ Schichten in Magnetfeldern bis 100 mT". BSc thesis. Universität Wien, 2012.

[58] Zechner, G., Jausner, F., Haag, L. T., Lang, W., Dosmailov, M., Bodea, M. A., and Pedarnig, J. D. "Hysteretic Vortex-Matching Effects in High-T_c Superconductors with Nanoscale Periodic Pinning Landscapes Fabricated by He Ion-Beam Projection". In: *Physical Review Applied* 8.1 (2017). DOI: 10.1103/physrevapplied.8.014021.

[59] Zechner, G., Mletschnig, K. L., Lang, W., Dosmailov, M., Bodea, M. A., and Pedarnig, J. D. "Unconventional critical state in $YBa_2Cu_3O_{7-\delta}$ thin films with a vortex-pin lattice fabricated by masked He^+ ion beam irradiation". In: *Supercond. Sci. Technol.* 31.4 (2018), p. 044002. DOI: 10.1088/1361-6668/aaacc1.

[60] Khalfin, I. B. and Shapiro, B. Y. "Relaxation of magnetic flux in a superconductor with a system of columnar defects". In: *Physica C: Superconductivity* 207.3-4 (1993), pp. 359–365. DOI: 10.1016/0921-4534(93)90318-k.

[61] Doria, M. M., Brandt, E. H., and Peeters, F. M. "Magnetization of a superconducting film in a perpendicular magnetic field". In: *Physical Review B* 78.5 (2008). DOI: 10.1103/physrevb.78.054407.

[62] Xu, M., Shi, D., and Fox, R. F. "Generalized critical-state model for hard superconductors". In: *Physical Review B* 42.16 (1990), pp. 10773–10776. DOI: 10.1103/physrevb.42.10773.

[63] Zechner, G. "Vortex commensurability effects in cuprate superconductors with nanoscale pinning lattices fabricated by masked ion beam irradiation". PhD thesis. University of Vienna, 2018.

[64] Haj33. URL: https://commons.wikimedia.org/wiki/File%3AYbco.jpg.

[65] Uimin, G. V. and Rossat-Mignod, J. "Role of Cu-O chains in the charge transfer mechanism in $YBa_2Cu_3O_{6+x}$". In: *Physica C: Superconductivity* 199.3-4 (1992), pp. 251–261. DOI: 10.1016/0921-4534(92)90408-5.

[66] Cava, R. J., Batlogg, B., Rabe, K. M., Rietman, E. A., Gallagher, P. K., and Rupp, L. W. "Structural anomalies at the disappearance of superconductivity in $Ba_2YCu_3O_{7-\delta}$: Evidence for charge transfer from chains to planes". In: *Physica C: Superconductivity* 156.4 (1988), pp. 523–527. ISSN: 0921-4534. DOI: 10.1016/0921-4534(88)90015-9.

[67] Tranquada, J. M., Moudden, A. H., Goldman, A. I., Zolliker, P., Cox, D. E., Shirane, G., Sinha, S. K., Vaknin, D., Johnston, D. C., Alvarez, M. S., Jacobson, A. J., Lewandowski, J. T., and Newsam, J. M. "Antiferromagnetism in $YBa_2Cu_3O_{6+x}$". In: *Physical Review B* 38.4 (1988), pp. 2477–2485. DOI: 10.1103/physrevb.38.2477.

[68] Tolentino, H., Baudelet, F., Fontaine, A., Gourieux, T., Krill, G., Henry, J. Y., and Rossat-Mignod, J. "Sequence and symmetry of hole injection in $YBa_2Cu_3O_{6+x}$ in situ and ex situ experiments on powders and single crystals using X-ray absorption spectroscopy". In: *Physica C: Superconductivity* 192.1-2 (1992), pp. 115–130. DOI: 10.1016/0921-4534(92)90751-w.

[69] Uimin, G. V., Gantmakher, V. F., Neminsky, A. M., Novomlinsky, L. A., Shovkun, D. V., and Brüll, P. "Dependence of T_c on the oxygen distribution in the Cu-O chains in the high temperature superconductors $YBa_2Cu_3O_{6+x}$". In: *Physica C: Superconductivity* 192.3-4 (1992), pp. 481–490. DOI: 10.1016/0921-4534(92)90857-9.

[70] Wuyts, B., Moshchalkov, V. V., and Bruynseraede, Y. "Resistivity and Hall effect of metallic oxygen-deficient $YBa_2Cu_3O_x$ films in the normal state". In: *Physical Review B* 53.14 (1996), pp. 9418–9432. DOI: 10.1103/physrevb.53.9418.

[71] Lang, W., Heine, G., Schwab, P., Wang, X. Z., and Bäuerle, D. "Paraconductivity and excess Hall effect in epitaxial $YBa_2Cu_3O_7$ films induced by superconducting fluctuations". In: *Physical Review B* 49.6 (1994), pp. 4209–4217. DOI: 10.1103/PhysRevB.49.4209.

[72] Civale, L., Marwick, A. D., McElfresh, M. W., Worthington, T. K., Malozemoff, A. P., Holtzberg, F. H., Thompson, J. R., and Kirk, M. A. "Defect independence of the irreversibility line in proton-irradiated Y-Ba-Cu-O crystals". In: *Physical Review Letters* 65.9 (1990), pp. 1164–1167. DOI: 10.1103/physrevlett.65.1164.

[73] Tolpygo, S. K., Lin, J.-Y., Gurvitch, M., Hou, S. Y., and Phillips, J. M. "Effect of oxygen defects on transport properties and T_c of $YBa_2Cu_3O_{6+x}$: Displacement energy for plane and chain oxygen and implications for irradiation-induced resistivity and T_c suppression". In: *Physical Review B* 53.18 (1996), pp. 12462–12474. DOI: 10.1103/PhysRevB.53.12462.

[74] Dineva-Stavreva, M. "Monte-Carlo Simulation der Defekterzeugung durch Ionenstrahlen in Hochtemperatursupraleitern". PhD thesis. Universität Wien, 2005.

[75] Lang, W. and Pedarnig, J. D. "Ion Irradiation of High-Temperature Superconductors and Its Application for Nanopatterning". In: *Nanoscience and Engineering in Superconductivity*. Ed. by Moshchalkov, V., Woerdenweber, R., and Lang, W. Springer Berlin Heidelberg, 2010. Chap. 3, pp. 81–104. DOI: 10.1007/978-3-642-15137-8_3.

[76] Lang, W., Dineva, M., Marksteiner, M., Enzenhofer, T., Siraj, K., Peruzzi, M., Pedarnig, J. D., Bäuerle, D., Korntner, R., Cekan, E., Platzgummer, E., and Loeschner, H. "Ion-beam direct-structuring of high-temperature superconductors". In: *Microelectronic Engineering* 83.4-9 (2006), pp. 1495–1498. DOI: 10.1016/j.mee.2006.01.091.

[77] Legoues, F. K., Ruault, M. O., Clark, G., Bernas, H., and Gasgnier, M. "In situ studies of microstructural changes in $YBa_2Cu_3O_{7-x}$ during O and He irradiation". In: *Philosophical Magazine A* 60.5 (1989), pp. 525–538. DOI: 10.1080/01418618908213876.

[78] Enzenhofer, T. "Eigenschaften von Hochtemperatur-Supraleitern nach Bestrahlung mit leichten Ionen". Diploma thesis. Universität Wien, 2003.

[79] Marwick, A. D., Clark, G. J., Yee, D. S., Laibowitz, R. B., Coleman, G., and Cuomo, J. J. "Resistivity changes and defect mobility in ion-irradiated $YBa_2Cu_3O_{7-x}$". In: *Physical Review B* 39.13 (1989), pp. 9061–9068. DOI: 10.1103/PhysRevB.39.9061.

[80] Gross, R. and Marx, A. *Festkörperphysik*. Oldenbourg Wissenschaftsverlag, 2014. DOI: 10.1524/9783110358704.

[81] Lang, W., Richter, H., Marksteiner, M., Siraj, K., Bodea, M. A., Pedarnig, J. D., Grigoropoulos, C., Bauerle, D., Hasenfuss, C., Palmetshofer, L., Kolarova, R., and Bauer, P. "Masked ion beam irradiation of high-temperature superconductors: patterning of nano-size regions with high point-defect density". In: *International Journal of Nanotechnology* 6.7/8 (2009), pp. 704–714. DOI: 10.1504/ijnt.2009.025308.

[82] Anderson, P. W. "Hall effect in the two-dimensional Luttinger liquid". In: *Physical Review Letters* 67.15 (1991), pp. 2092–2094. DOI: 10.1103/physrevlett.67.2092.

[83] Lang, W., Enzenhofer, T., Peruzzi, M., Pedarnig, J. D., Bäuerle, D., Horner, C., Cekan, E., Platzgummer, E., and Loeschner, H. "Tailoring the transport properties of $YBa_2Cu_3O_{7-\delta}$ thin films by light-ion irradiation". In: *Inst. Phys. Conf. Ser.* Vol. 181. 2004, pp. 1549–1555.

[84] Valles, J. M., White, A. E., Short, K. T., Dynes, R. C., Garno, J. P., Levi, A. F. J., Anzlowar, M., and Baldwin, K. "Ion-beam-induced metal-insulator transition in $YBa_2Cu_3O_{7-\delta}$: A mobility edge". In: *Physical Review B* 39.16 (1989), pp. 11599–11602. DOI: 10.1103/PhysRevB.39.11599.

[85] White, A. E., Short, K. T., Garno, J. P., Valles, J. M., Dynes, R. C., Schneemeyer, L. F., Waszczak, J., Levi, A. F. J., Anzlowar, M., and Baldwin, K. W. "Implantation, damage, and regrowth of high T_c superconductors". In: *Nuclear Instruments and Methods in Physics Research Section B: Beam Interactions with Materials and Atoms* 37-38 (1989), pp. 923–929. DOI: 10.1016/0168-583x(89)90328-5.

[86] Tolpygo, S. K., Lin, J.-Y., Gurvitch, M., Hou, S. Y., and Phillips, J. M. "T_c enhancement by low energy electron irradiation and the influence of chain disorder on resistivity and Hall coefficient in $YBa_2Cu_3O_7$ thin films". In: *Physica C: Superconductivity* 269.3-4 (1996), pp. 207–219. DOI: 10.1016/0921-4534(96)00450-9.

[87] Tolpygo, S. K., Lin, J.-Y., Gurvitch, M., Hou, S. Y., and Phillips, J. M. "Universal T_c suppression by in-plane defects in high-temperature superconductors: Implications for pairing symmetry". In: *Physical Review B* 53.18 (1996), pp. 12454–12461. DOI: 10.1103/physrevb.53.12454.

[88] Legris, A., Rullier-Albenque, F., Radeva, E., and Lejay, P. "Effects of electron irradiation on $YBa_2Cu_3O_{7-\delta}$ superconductor". In: *Journal de Physique I* 3.7 (1993), pp. 1605–1615. DOI: 10.1051/jp1:1993203.

[89] Wang, X. Z., Hellebrand, B., Bäuerle, D., Strecker, M., Wortmann, G., and Lang, W. "Oxygen ordering and superconductivity in $GdBaSrCu_3O_{7-x}$". In: *Physica C: Superconductivity* 242.1-2 (1995), pp. 55–62. DOI: 10.1016/0921-4534(94)02370-0.

[90] Ziegler, J. F., Biersack, J. P., and Ziegler, M. D. *SRIM: The Stopping and Range of Ions in Matter*. SRIM Company, 2008.

[91] Ziegler, J. F., Biersack, J. P., and Littmark, U. *Stopping and Range of Ions in Matter*. version 2013. 1985. URL: http://www.srim.org/.

[92] Biersack, J. P. and Haggmark, L. G. "A Monte Carlo computer program for the transport of energetic ions in amorphous targets". In: *Nuclear Instruments and Methods* 174.1-2 (1980), pp. 257–269. DOI: 10.1016/0029-554x(80)90440-1.

[93] Marwick, A. D. and Clark, G. J. "Ion implantation in high-T_c superconductors". In: *Nuclear Instruments and Methods in Physics Research Section B: Beam Interactions with Materials and Atoms* 37-38 (1989), pp. 910–916. DOI: 10.1016/0168-583x(89)90326-1.

[94] Cui, F. Z., Xie, J., and Li, H. D. "Preferential radiation damage of the oxygen sublattice in $YBa_2Cu_3O_7$: A molecular-dynamics simulation". In: *Physical Review B* 46.17 (1992), pp. 11182–11185. DOI: 10.1103/PhysRevB.46.11182.

[95] Emmrich, D., Beyer, A., Nadzeyka, A., Bauerdick, S., Meyer, J. C., Kotakoski, J., and Gölzhäuser, A. "Nanopore fabrication and characterization by helium ion microscopy". In: *Applied Physics Letters* 108.16 (2016), p. 163103. DOI: 10.1063/1.4947277.

[96] Lesueur, J., Nedellec, P., Bernas, H., Burger, J. P., and Dumoulin, L. "Depairing-like variation of T_c in $YBa_2Cu_3O_{7-\delta}$". In: *Physica C: Superconductivity* 167.1-2 (1990), pp. 1–5. DOI: 10.1016/0921-4534(90)90477-v.

[97] Abrikosov, A. A. and Gorkov, L. P. "Contribution to the theory of superconducting alloys with paramagnetic impurities". In: *Sov. Phys.-JETP* 12.2 (1961), pp. 337–339.

[98] Abramowitz, M. and Stegun, I. A. *Handbook of Mathematical Functions with Formulas, Graphs, and Mathematical Tables*. Vol. 20. 93. JSTOR, 1966, p. 167. DOI: 10.2307/2004284.

[99] Clark, G. J., Marwick, A. D., Koch, R. H., and Laibowitz, R. B. "Effects of radiation damage in ion-implanted thin films of metal-oxide superconductors". In: *Applied Physics Letters* 51.2 (1987), pp. 139–141. DOI: 10.1063/1.98594.

[100] URL: www.wolframalpha.com.

[101] Nédellec, P., Lesueur, J., Traverse, A., Bernas, H., Dumoulin, L., and Laibowitz, R. "Nature of the granular structure in low-temperature helium-irradiated YBaCuO thin films". In: *Journal of the Less Common Metals* 151 (1989), pp. 443–449. DOI: 10.1016/0022-5088(89)90351-2.

[102] Edwards, H. L., Markert, J. T., and Lozanne, A. L. de. "Energy gap and surface structure of $YBa_2Cu_3O_{7-x}$ probed by scanning tunneling microscopy". In: *Physical Review Letters* 69.20 (1992), pp. 2967–2970. DOI: 10.1103/PhysRevLett.69.2967.

[103] Dosmailov, M. "Functional oxide thin films by pulsed-laser deposition: ion beam nanostructuring of epitaxial $YBa_2Cu_3O_{7-\delta}$ and growth of conductive transparent $Zn_{1-x}Al_xO$ on compliant substrates". PhD thesis. Johannes Kepler University, 2015.

[104] Bodea, M.-A. "Deposition and characterization of nano-composite M-2411/YBCO thin films and ion beam modification of YBCO thin films". Dissertation. Johannes Kepler University Linz, 2010.

[105] Holzapfel, B. and Wiesmann, J. "Substrates and functional buffer layers". In: *Handbook of superconducting materials*. Ed. by Cardwell, D. A. and Ginley, D. S. Vol. 1. IoP Institute of Physics Publishing, 2002. Chap. B4.1, pp. 723–740.

[106] Bäuerle, D. *Laser Processing and Chemistry*. Springer Berlin Heidelberg, 2011. DOI: 10.1007/978-3-642-17613-5.

[107] Pedarnig, J. D., Siraj, K., Bodea, M. A., Puica, I., Lang, W., Kolarova, R., Bauer, P., Haselgrübler, K., Hasenfuss, C., Beinik, I., and Teichert, C. "Surface planarization and masked ion-beam structuring of $YBa_2Cu_3O_7$ thin films". In: *Thin Solid Films* 518.23 (2010), pp. 7075–7080. DOI: 10.1016/j.tsf.2010.07.021.

[108] Pedarnig, J. D. private communication.

[109] Pedarnig, J. D., Bodea, M. A., Steiger, B., Markowitsch, W., and Lang, W. "Systematic Modification of Electrical and Superconducting Properties of YBCO and Nano-Patterning of High-T_c Superconducting Thin Films by Light-Ion Irradiation". In: *Physics Procedia* 36 (2012), pp. 508–513. DOI: 10.1016/j.phpro.2012.06.075.

[110] Umrath, W. *Grundlagen der Vakuumtechnik*. Leybold Vakuum, 1997.

[111] URL: https://www.arscryo.com/cryocooler-principles-of-operation/.

[112] Göb, W. "Magnetotransport Effekte und Fluktuationen im sauerstoffreduzierten Hochtemperatur Supraleiter $YBa_2Cu_3O_{7-\delta}$". Diplomarbeit. Universität Wien, 1997.

[113] Heine, G. and Lang, W. "Magnetoresistance of the new ceramic "Cernox" thermometer from 4.2 K to 300 K in magnetic fields up to 13 T". In: *Cryogenics* 38.4 (1998), pp. 377–379. DOI: 10.1016/s0011-2275(97)00130-6.

[114] Sørensen, M. P., Pedersen, N. F., and Ögren, M. "The dynamics of magnetic vortices in type II superconductors with pinning sites studied by the time dependent Ginzburg–Landau model". In: *Physica C: Superconductivity and its Applications* 533 (2017), pp. 40–43. DOI: 10.1016/j.physc.2016.08.001.

[115] Brandt, E. H., Indenbom, M. V., and Forkl, A. "Type-II Superconducting Strip in Perpendicular Magnetic Field". In: *Europhysics Letters (EPL)* 22.9 (1993), pp. 735–740. DOI: 10.1209/0295-5075/22/9/017.

[116] Haag, L. T., Zechner, G., Lang, W., Dosmailov, M., Bodea, M. A., and Pedarnig, J. D. "Strong vortex matching effects in YBCO films with periodic modulations of the superconducting order parameter fabricated by masked ion irradiation". In: *Physica C: Superconductivity and its Applications* 503 (2014), pp. 75–81. DOI: 10.1016/j.physc.2014.03.032.

[117] Cooley, L. D. and Grishin, A. M. "Pinch Effect in Commensurate Vortex-Pin Lattices". In: *Physical Review Letters* 74.14 (1995), pp. 2788–2791. DOI: 10.1103/physrevlett.74.2788.

[118] Reichhardt, C., Groth, J., Olson, C. J., Field, S. B., and Nori, F. "Spatiotemporal dynamics and plastic flow of vortices in superconductors with periodic arrays of pinning sites". In: *Physical Review B* 54.22 (1996), pp. 16108–16115. DOI: 10.1103/physrevb.54.16108.

[119] Silhanek, A. V., Gutierrez, J., Kramer, R. B. G., Ataklti, G. W., Vondel, J. van de, Moshchalkov, V. V., and Sanchez, A. "Microscopic picture of the critical state in a superconductor with a periodic array of antidots". In: *Physical Review B* 83.2 (2011). DOI: 10.1103/physrevb.83.024509.

[120] Feinberg, D. and Villard, C. "Intrinsic pinning and lock-in transition of flux lines in layered type-II superconductors". In: *Physical Review Letters* 65.7 (1990), pp. 919–922. DOI: 10.1103/physrevlett.65.919.

[121] Figueras, J., Puig, T., Obradors, X., Kwok, W. K., Paulius, L., Crabtree, G. W., and Deutscher, G. "The loss of vortex line tension sets an upper limit to the irreversibility line in $YBa_2Cu_3O_7$". In: *Nature Physics* 2.6 (2006), pp. 402–407. DOI: 10.1038/nphys311.

[122] Villegas, J. E., Savel'ev, S., Nori, F., Gonzalez, E. M., Anguita, J. V., Garcia, R., and Vicent, J. L. "A superconducting reversible rectifier that controls the motion of magnetic flux quanta". In: *Science* 302.5648 (2003). 742XW Times Cited:222 Cited References Count:31, pp. 1188–1191. ISSN: 0036-8075. URL: <GotoISI>://000186544300047.

[123] Vondel, J. van de, Souza Silva, C. C. de, Zhu, B. Y., Morelle, M., and Moshchalkov, V. V. "Vortex-rectification effects in films with periodic asymmetric pinning". In: *Physical Review Letters* 94.5 (2005). DOI: 10.1103/physrevlett.94.057003.

[124] Savel'ev, S., Misko, V., Marchesoni, F., and Nori, F. "Separating particles according to their physical properties: Transverse drift of underdamped and overdamped interacting particles diffusing through two-dimensional ratchets". In: *Physical Review B* 71.21 (2005). DOI: 10.1103/physrevb.71.214303.

[125] Olson Reichhardt, C. J. and Reichhardt, C. "Rectification and flux reversals for vortices interacting with triangular traps". In: *Physica C: Superconductivity* 432.3-4 (2005), pp. 125–132. DOI: 10.1016/j.physc.2005.07.017.

[126] Gonzalez, E. M., Nunez, N. O., Anguita, J. V., and Vicent, J. L. "Transverse rectification in superconducting thin films with arrays of asymmetric defects". In: *Applied Physics Letters* 91.6 (2007), p. 062505. DOI: 10.1063/1.2767199.

[127] Hastings, M. B., Olson Reichhardt, C. J., and Reichhardt, C. "Ratchet Cellular Automata". In: *Physical Review Letters* 90.24 (2003). DOI: 10.1103/physrevlett.90.247004.

[128] Seidel, P., ed. *Applied Superconductivity*. Wiley-VCH Verlag GmbH & Co. KGaA, 2015. DOI: 10.1002/9783527670635.